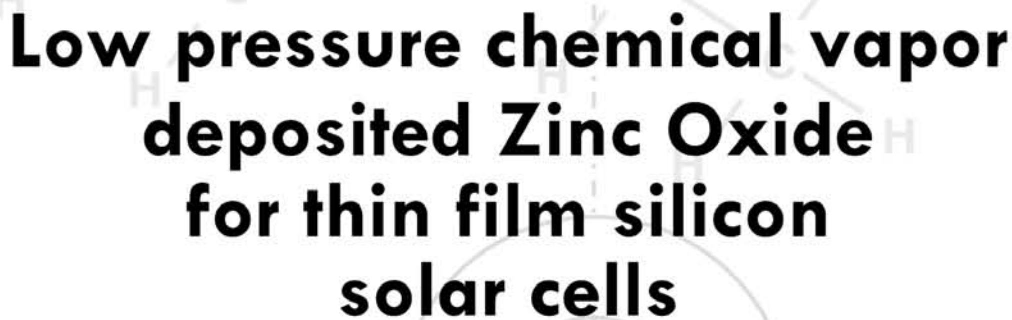

Low pressure chemical vapor deposited Zinc Oxide for thin film silicon solar cells

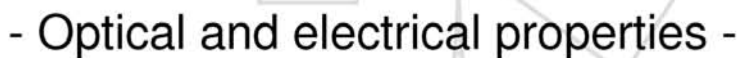

- Optical and electrical properties -

Jérôme
STEINHAUSER

imt
institute of microtechnology
university of neuchâtel

UNIVERSITY OF NEUCHÂTEL

INSTITUTE OF MICROTECHNOLOGY

LOW PRESSURE CHEMICAL VAPOR DEPOSITED ZINC OXIDE FOR SILICON THIN FILM SOLAR CELLS

OPTICAL AND ELECTRICAL PROPERTIES

JÉRÔME STEINHAUSER

Thèse présentée à la faculté des sciences, Institut de Microtechnique, Université de Neuchâtel, pour l'obtention du grade de docteur ès sciences. Acceptée sur proposition du jury : Prof. C Ballif, directeur de thèse, Dr S Faÿ, rapporteur, Prof. P Aebi, rapporteur, Dr. O. Kluth, rapporteur, Prof. R.E.I. Schropp, rapporteur. Soutenue le 29 octobre 2008.

Neuchâtel, October 2008

Université de Neuchâtel unine

FACULTE DES SCIENCES
Secrétariat-Décanat de la faculté
- Rue Emile-Argand 11
- CP 158
- CH-2009 Neuchâtel

IMPRIMATUR POUR LA THESE

Low Pressure Chemical Vapor Deposited Zinc Oxide for Silicon Thin Film Solar Cells: Optical and Electrical Properties

Jérôme STEINHAUSER

UNIVERSITE DE NEUCHATEL

FACULTE DES SCIENCES

La Faculté des sciences de l'Université de Neuchâtel,
sur le rapport des membres du jury

Mme S. Fay, MM. C. Ballif (directeur de thèse),
P. Aebi, O. Kluth (Oerlikon Solar AG, Trübbach)
et R.E.I. Schropp (Utrecht NL)

autorise l'impression de la présente thèse.

Neuchâtel, le 7 novembre 2008

Le doyen :
F. Kessler

UNIVERSITE DE NEUCHATEL
FACULTE DES SCIENCES
Secrétariat - décanat de la faculté
Rue Emile-Argand 11 - CP 158
CH-2009 Neuchâtel

Felix Kessler

■ Téléphone : +41 32 718 21 00 ■ E-mail : secretariat.sciences@unine.ch ■ www.unine.ch/sciences

// Keywords :

Zinc oxide, low pressure chemical vapor deposition, transparent conductive oxide, thin film silicon solar cells.

Summary :

Transparent conductive oxides (TCO), such as LPCVD ZnO:B (low pressure chemical vapor deposited zinc oxide doped with boron), play a major role as contacts in thin film silicon photovoltaic solar cells. This document study the "LPCVD ZnO:B layers, from the deposition process to the final application" and focus especially on their electrical and optical properties. This work intended on understanding the physics of the LPCVD ZnO:B film properties in order to efficiently optimize its characteristics to obtain TCO films well suited for thin film solar cell applications. In particular, theoretical models that describe the optical and electrical properties of LPCVD ZnO:B films are determined and verified experimentally.

Contents

Keywords / Summary **5**
Contents **7**

1 INTRODUCTION **11**

1.1 Solar energy 11
1.2 Photovoltaic solar cells 15
1.3 Transparent contacts 19
1.4 Aim and outline of this thesis 20
1.5 Contribution of this work to the research field 22

2 BASICS ON TRANSPARENT CONDUCTIVE OXIDES : FABRICATION, APPLICATIONS AND THEORY **25**

2.1 TCO fabrication, materials and applications 25
2.1.1 Deposition processes *25*
2.1.2 Materials *27*
2.1.3 Applications *29*

2.2 Thin film TCO physics 31
2.2.1 Band structure *31*
2.2.2 Optical properties *32*
2.2.3 Electrical properties *37*
2.2.4 Conclusions *45*

3 CHARACTERIZATION TECHNIQUES **47**

3.1 Structural characterizations 47
3.1.1 Thickness *47*
3.1.2 Electron microscopy (SEM, EDX, TEM, FIB) *47*
3.1.3 Atomic force microscopy (AFM) *48*
3.1.4 X-ray diffraction (XRD) *48*
3.1.5 Rutherford backscattering spectroscopy (RBS) *49*
3.1.6 Secondary ion mass spectroscopy (SIMS) *50*

3.2 Optical characterizations 50
3.2.1 Ultra-Violet / Visible / Near InfraRed spectroscopy *50*
3.2.2 Fourier Transform InfraRed spectroscopy (FTIR) *52*
3.2.3 Angular distribution function (ADF) *52*
3.2.4 Ellipsometry spectroscopy *52*

3.2.5 Raman spectroscopy *53*

3.3 Electrical characterizations 53

3.3.1 Four probe square resistance *53*
3.3.2 Hall effect *54*
3.3.3 Temperature dependence of the conductivity *56*

3.4 Solar cell characterizations 56

3.4.1 Solar cell deposition *56*
3.4.2 Illuminated current-voltage measurement *56*
3.4.3 External quantum efficiency *56*
3.4.4 Lockin thermography *57*

4 FABRICATION AND GROWTH OF LPCVD ZNO:B FILMS 59

4.1 Fabrication of LPCVD ZnO:B 59

4.1.1 Low pressure chemical vapor deposition system *59*
4.1.2 Chemical reactions *61*
4.1.3 Review of the main deposition parameter effect *63*
4.1.4 Standard LPCVD ZnO:B layers deposition parameters and characteristics *65*

4.2 Structural and chemical properties of LPCVD ZnO:B films 67

4.2.1 Crystallographic orientation *67*
4.2.2 Electron microscopy investigations *67*
4.2.3 Chemical properties *69*

4.3 Conclusions 72

5 OPTICAL PROPERTIES OF LPCVD ZNO:B FILMS 73

5.1 Transmission and reflection studies 73

5.1.1 Overview *73*
5.1.2 Band gap absorption *78*
5.1.3 Infrared response *83*

5.2 Light scattering capabilities 86

5.3 Raman analysis 93

5.4 Conclusions 94

6 ELECTRICAL PROPERTIES OF LPCVD ZNO:B FILMS 97

6.1 Overview of the electrical properties of LPCVD ZnO:B films.... 97

6.2 Advanced electrical characterizations 101

6.2.1 Optical measurements of electrical parameters *.......................... 102*
6.2.2 Temperature dependence of the conductivity *............................ 107*
6.2.3 Water vapour exposure *.. 112*

6.3 Conclusions 117

7 INTEGRATION OF LPCVD ZNO:B FILMS
IN THIN FILM SILICON SOLAR CELLS 119

7.1 Light trapping in μcSi:H solar cells... 119

7.2 Front contact induced shunt issues 126

7.2.1 Particles and its influences on shunting behaviors *.................... 126*
7.2.2 Morphology and its influence on shunting behavior *................ 131*
7.2.3 Plasma surface treatments *.. 134*

7.3 High current and best solar cell results...................................... 136

7.4 Conclusions 137

8 FINAL CONCLUSIONS...139

8.1 Conclusions 139

8.2 Perspectives.. 142

Appendix : shunt analysis 145

Acknowledgments 149

References 151

CHAPTER 1 *Introduction*

This chapter describes the general scientific context and the research field in which this thesis is included. First, the motivations for the use of photovoltaic (PV) power regarding the global energy issues are given. The second paragraph gives a brief overview of the diverse photovoltaic technologies and discusses the advantages of thin film silicon solar cells. In section 1.3, transparent conductive oxide (TCO) materials are presented and their use as an electrical contact in solar cells is explained. Finally, the aim of this work is summarized and the structure and the outline of this thesis is presented.

1.1 Solar energy

In 2005 no less than 87% of the world's total primary energy production was coming from non renewable sources : oil (35%), coal (25.3%), natural gas (20.7%), and nuclear (6.3%) [IEA 2007]. These non-renewable energies will soon be facing outstanding problems. Firstly, the decrease of the fossil fuels and uranium stocks make their capacity to supply the long-term energy demand with reasonable price uncertain [Laherrere 2005]. Secondly, burning fossil fuel releases large amounts of CO_2 into the atmosphere inducing the global warming of the Earth [IPCC 2007]. Besides these issues, the International Energy Agency expects an increase in the energy consumption of less developed countries, due to their rising industrialization [IEA 2007]. Therefore, in order to support the world energy consumption, we need to develop energy generation techniques that support the requirements of sustainability and renewability.

Resources for renewable energy production are various : solar energy, wind energy, geothermal energy, hydropower, biomass energy, wave power, and ocean thermal energy. Table 1.1 shows technical and theoretical potentials of renewable energy resources expressed in exajoules per year (1 EJ = 10^{18} J = 278 10^{9} kWh) [UNDP 2000]. The technical potential of these

Table 1.1 *The renewable energy resource potential in exajoules (EJ) per year. Numbers from reference [UNDP 2000].1EJ=10^{18}J=278 10^{9}kWh.*

Resource	Current use (EJ)	Technical potential (EJ)	Theoretical potential (EJ)
Hydropower	9	50	147
Biomass energy	50	>276	2'900
Solar energy	0.1	>1'575	3'900'000
Wind energy	0.12	640	6'000
Geothermal energy	0.6	5'000	140'000'000
Ocean energy	Not estimated	Not estimated	7'400
Total	56	>7'600	>144'000'000

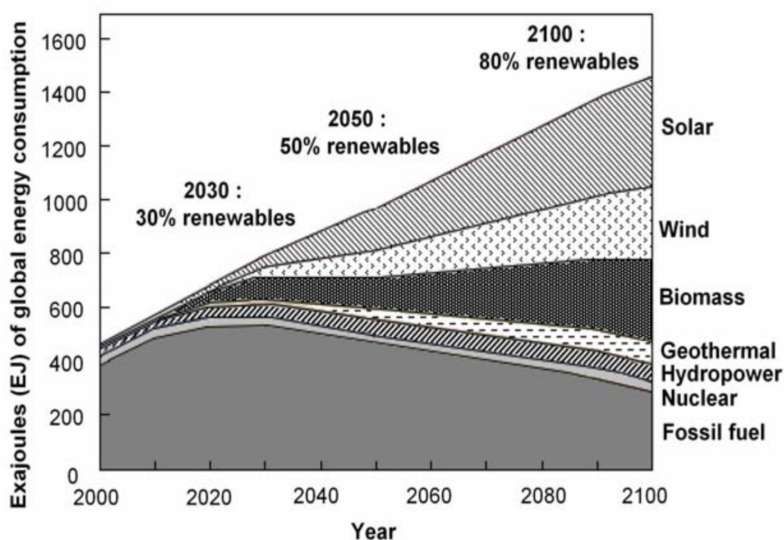

Figure 1.1 *Contributions of the different energy sources to primary energy consumption described by Aitken [Aitken 2004] in his "scenario" to support a stabilization at a CO_2 concentration in the atmosphere of 550 ppm. The points labeled indicate what percentage the renewable energies would provide to the total expected energy consumption. Numbers from reference [Aitken 2004]. 1EJ=10^{18}J=278 10^{9}kWh.*

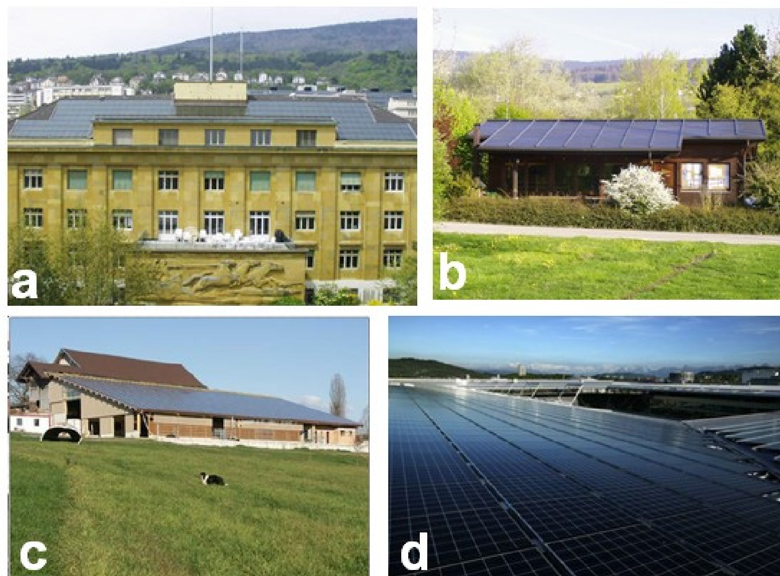

Figure 1.2 *Four examples of Swiss photovoltaic installations :* a *: Institute of Microtechnology, Neuchâtel (NE), b : Nautical Club, Auvernier (NE), c : Barberèche farm (FR), d : Swiss stadium (BE).*

energy sources is superior to 7600 exajoules per year, which is 15 times higher than the world total energy consumption (478.8 exajoules/year in 2005 [IEA 2007]). Solar energy has a particularly high technical potential, more than 1575 exajoules per year, which exceed the potential of hydropower, biomass energy and wind energies.

Figure 1.1 shows the expected energy consumption from now until 2100 and the amounts of fossil fuel and renewable energy needed for a stabilization of the CO_2 concentration in the atmosphere at 550 ppm [Aitken 2004]. It can be noticed that, according to Aitken, solar energy will play a major role in the next century. This tendency is also predicted by the International Energy Agency which publishes a "scenario" of the evolution of renewable energy. It expects a 60-fold increase of solar energy production from now until 2030 [IEA 2007b].

Energy suppliers convert the solar energy to functional energy using two techniques : heat generation from thermal collectors and electrical production from photovoltaic modules. As the application field of this research is the photovoltaic technique, we do not present the heat generation technique here.

The photovoltaic electricity production has numerous advantages : 1) it has no moving part or mass flow, 2) it has no maintenance, 3) It is highly reliable, 4) it integrates well into an urban environment, 5) and it has the possibility to produce electricity locally.

Figure 1.2 shows some examples of photovoltaic installations in Switzerland. Large realizations such as the Swiss stadium solar generator or small ones such as the solar rooftop of the Nautical Club of Auvernier demonstrate that photovoltaic installations are appropriate for any type of location.

In Bern, Switzerland, the global annual solar irradiation of about ~1100 $kWhm^{-2}$ would provide a typical annual output of 900~1000 kWh/kWp for a rooftop photovoltaic generator and of 600~700 kWh/kWp for a façade installation [IEA PVPS 2006]. A solar installation of 3.5 kWp, which corresponds to a surface of 6×6 m^2 of 10 % efficient PV modules, covers the average consumption of a Swiss household (3000 kWh/year). In this case, the energy needed to produce the modules (energy payback time) is produced in about 3 years with crystalline modules or even 1.5 years with thin film modules [Fthenakis 2007, Aselma 2006, Wild-Scholten 2005].

One issue is that solar electricity faces is its non-continuous production along the time due to the daily and seasonal variations of the sun irradiance. However, several facts attenuate this drawback. Firstly, electricity consumption occurs mainly during the day when PV modules also produce electricity. Secondly, peak production is regulated via "balancing power" techniques (e.g. switching electricity production of fuel plants on or off [Sinn 2006]). Third, in countries equipped with dams, the electricity produced by PV installations can be stored using hydroelectrical resources. Finally, the electricity can be distributed on the worldwide grid.

Another currently negative aspect is the relatively high cost of photovoltaic systems. At the beginning of 2008 the retail module price in Europe was about 3~4 Euros per watt peak [Solarbuzz].

Indeed, best fabrication costs (not prices) are reported to be in the range of 1 Euro per watt peak for thin film and 1.5 Euros per watt peak for crystalline modules. Furthermore, PV module manufacturers predict important cost reductions in the PV module price, linked with the development of thin film PV modules manufacture [Photon].

Figure 1.3 shows the annual PV production capacity from 1995 to 2006. The exponential growth is due to large industrial investment and political support for the development of solar electricity. No less than 9 billion dollars are now invested annually in new PV production facilities, leading to numerous job creations [EPIA 2007].

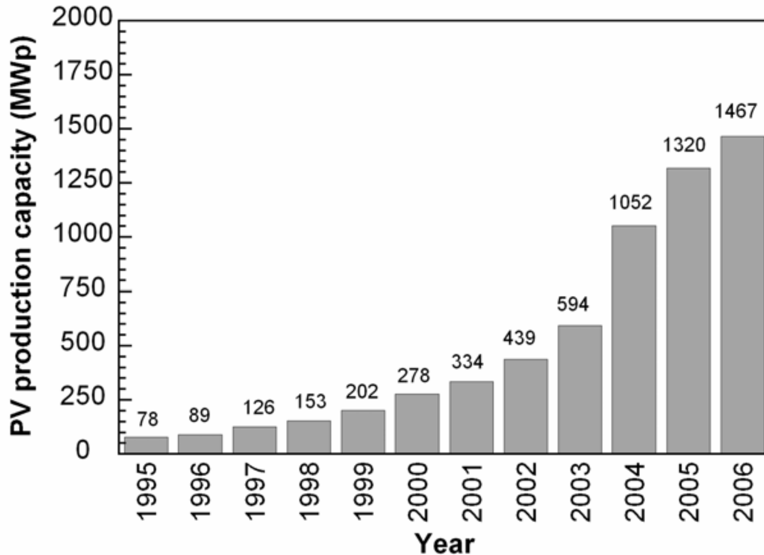

Figure 1.3 *The global annual PV market. Numbers from reference [EPIA 2007].*

1.2 Photovoltaic solar cells

Figure 1.4 shows the spectral distribution of the AM1.5G solar spectrum. It corresponds to the sun energy incident normalized at 1000 W.m^{-2}, at each wavelength, on a 37° sun-facing tilted surface relative to the horizontal under standard atmospheric conditions (see [IEC 2005] for a complete description of these standards conditions). A photovoltaic cell is made of a material that absorbs a part of this solar spectrum. This absorption generates electrical charge carriers. These charge carriers produce an electrical current when extracted from the material [Goetzberger 2005, Green 1987, Green 1982].

Several different materials are used as absorber in solar cells : crystalline silicon, gallium arsenide, cadmium telluride, copper indium selenide, organic dyes etc… For reviews concerning photovoltaic technologies, see for instance [Sun 2005, Martí 2004, Green 2003, Bubenzer 2003, Fonash 1981].

To be absorbed, in semiconductor materials such as silicon, photons must have energy to excite an electron from the valence band to the conduction band. This minimum energy named "energy gap" or "band gap" (E_g) depends on the type of semiconductor [Sze 1981].

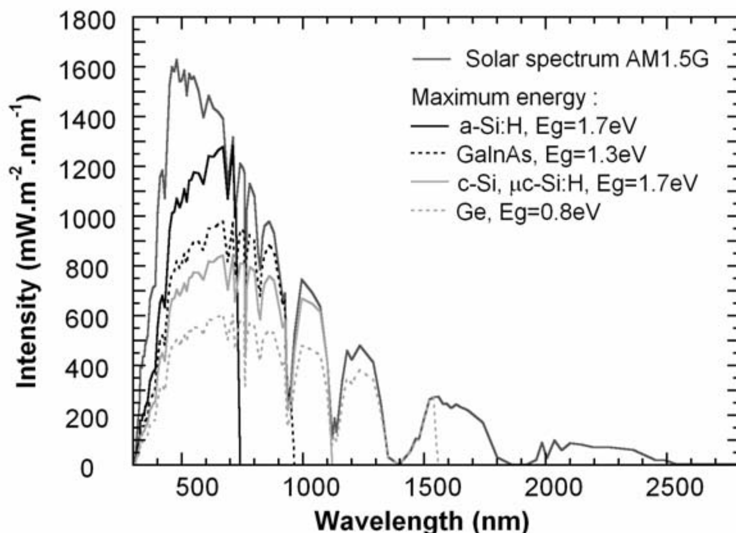

Figure 1.4 *The solar spectrum under standard atmospheric conditions AM1.5G [IEC 2005], and the maximum energy that commonly-used photovoltaic material can extract from it.*

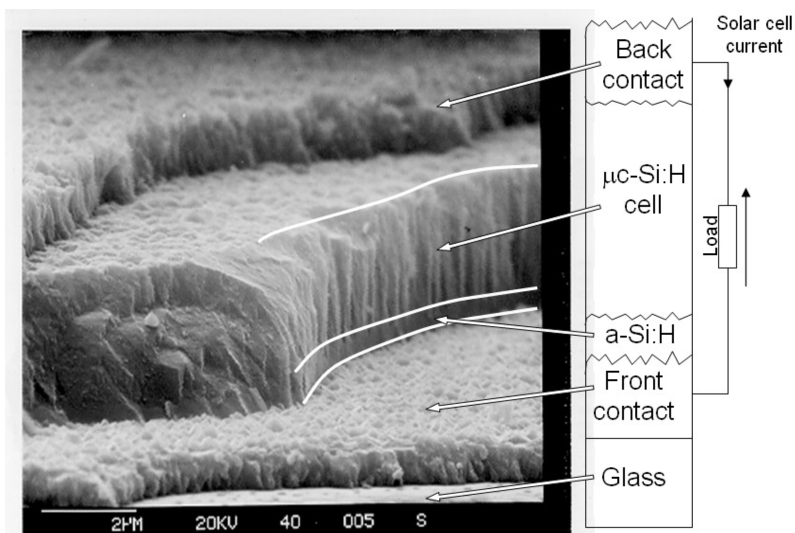

Figure 1.5 *Scanning electron micrograph of a micromorph tandem solar cell composed of an a-Si:H cell /μc-Si:H cell layer stack.*

In semiconductors with small E_g, photons of low energy are absorbed and a large quantity of electron-hole pairs are generated, leading to a high photogenerated current. However, in this case, electrons in the conduction band have low energy levels compared to holes in the valence band leading to photodiodes with low voltage. In contrast, in case of a semiconductor with a large E_g, only photons with high energy are absorbed. This results in a lower generation of electron-hole pairs but with higher energy difference, leading to low current and high voltage photodiodes [Sze 1981].

Superposed on the solar spectrum in figure 1.4, is the maximum energy that semiconductors with different band gaps can extract from the sun energy, plotted as a function of the wavelength. This illustrates the compromise existing between current and voltage, leading to an efficiency limit for semiconductor single junction solar cells of 33% [Green 2002].

In this study, we focus on thin film silicon solar cells. The first amorphous thin film silicon solar cells was fabricated in 1977 by Carlson [Carlson 1977]. Since then, several international research groups have been studying thin film silicon solar cells and regularly publishing reviews about their latest developments [Shah 2006, Rech 2003, Brendel 2003, Shah 1999, Schropp 1998, Catalano 1982].

Advantages of thin film silicon solar cells are multiple. The raw material is non-toxic and wide available, contrary to indium (In) and telluride (Te) for which feedstock become problematic at a few GigaWatts of annual production [Behrendt 2008]. Furthermore, in thin film silicon solar cell technology, the raw material usage is reduced by a factor 100 in comparison to the silicon wafer based technology for which 200 µm-thick wafers are typically used [Goetzberger 1998]. The relative low process temperature, about 200°C, allows deposition of solar cells on a large variety of substrates. In particular, thin film silicon solar cells can be deposited on flexible plastic foils [Rath, 2007, Liu 2007, Katsum 2007, Haug 2006, Yan 2006, Saito 1998, Ichikawa 1993]. The building integration of such cells is thus facilitated. In addition to this, the thin film silicon deposition process shows synergy with other industrial sectors like flat panel display or the packaging industry, which favors the fabrication of large area modules [Meier 2008, Lechner 2008, Chae 2007] and their continuous fabrication capability [Bailat 2005].

The relatively low efficiency of amorphous thin film silicon modules (about 6~8 %) is counterbalanced by lower production costs [Zweibel 2004, Green 2003b, Woodcock 1997] and a better temperature coefficient of the efficiency [Carlson 2000]. This improved temperature coefficient of the efficiency combine with a self annealing effect leads to an annual power generation per watt peak (W_p : the maximum rated output of a photovoltaic

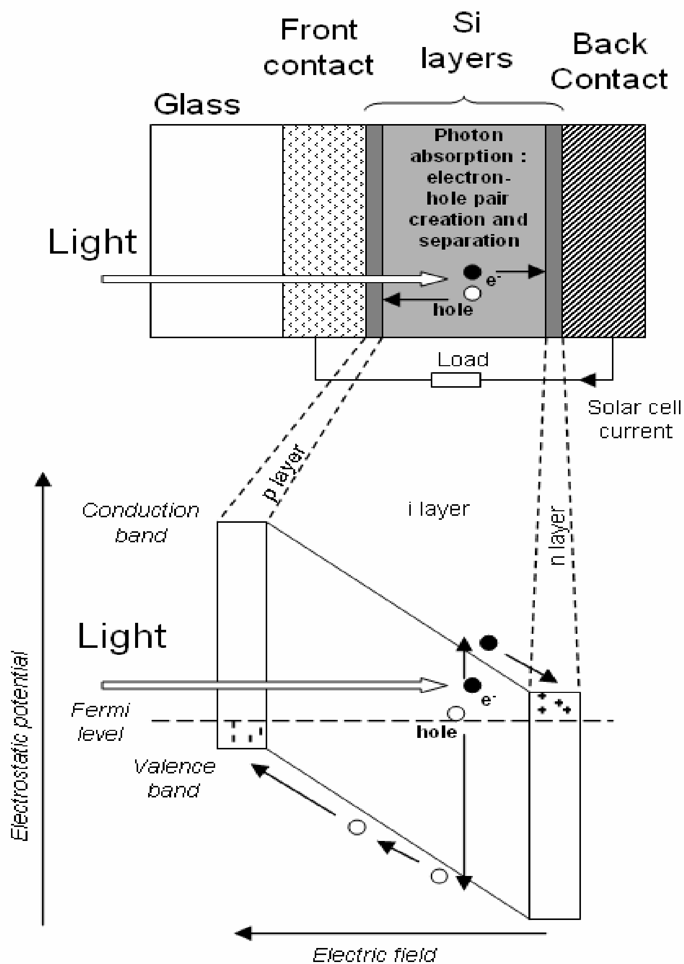

Figure 1.6 *The schematic structure and the band diagram of a pin solar cell. The photocarrier collection is illustrated here.*

device, under standardized test conditions [IEC 2005]) installed superior to the one achieved with crystalline silicon modules [Adhikari 2004].

To achieve higher efficiency cells, the Institute of Microtechnology of Neuchâtel (IMT) introduced the micromorph tandem cell concept [Meier 1994]. As illustrated by figure 1.5, a high gap material (hydrogenated amorphous silicon aSi:H) is combined with a low gap material (hydrogenated microcrystalline silicon μcSi:H). Such a combination is particularly efficient as it takes advantage of a large part of the solar spectrum without sacrificing the voltage of the solar cells [Meillaud 2006]. This type of solar cells is now developed on a world-wide scale for large PV modules [Meier 2008, Chae 2007, Noda 2003, Repmann 2003, Yamamoto 2002].

Figure 1.6 illustrates the photocarrier collection in a typical thin film silicon solar cell (pin substrate configuration). The light is absorbed essentially in the intrinsic layer (i layer). This absorption generates free electron-hole pairs. An electrostatic field separates the electron-hole pairs in order to produce available electrical current on the external electrical contacts. Using substitutional doping with boron and phosphorus, we obtain a negatively charge n layer and a positively charge p layer. The electrostatic field is produced in the i layer by the pin structure of the layers stack (for a detailed explanations, see for instance [Shah 2004]).

1.3 Transparent contacts

The electrical current produced by the solar cells is extracted through electrical contact layers deposited on each side of the pin structure. The contact layer deposited on the face of the cell that is exposed to the sun, i.e. the front contact, needs to be transparent in order to let the light enter into the solar cell.

To achieve this, we use materials with the remarkable combination of high electrical conductivity and high optical transparency : the Transparent Conductive Oxides (TCO). The most commonly used TCO are tin oxide (SnO_2), indium tin oxide (ITO) and zinc oxide (ZnO). Chapter 2 presents a complete review about TCO materials.

Due to particularly thin absorber layer (typically 300 nm for aSi:H cells and 2 μm for μcSi:H cells [Shah 2004, Schropp 1998]) of thin film silicon solar cells, a front contact possesing a surface morphology that scatters the light is necessary to achieve a high current. As shown in figure 1.7, rough diffusing layers considerably increase the light path through the absorber and thus the amount of absorbed photons.

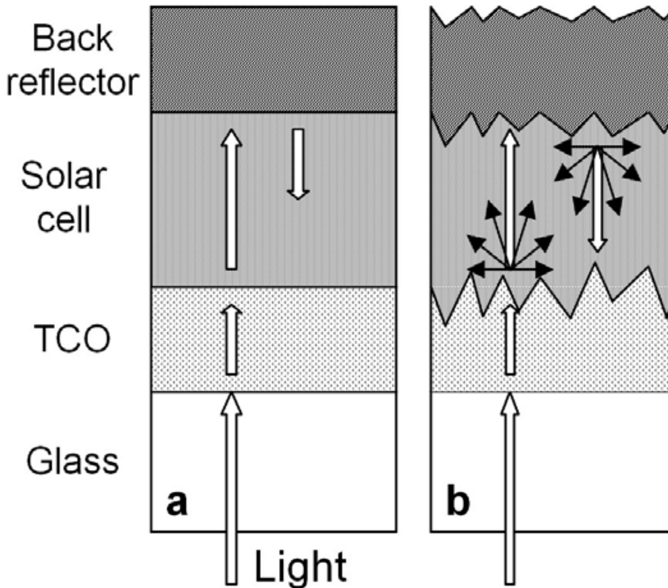

Figure 1.7 *A schematic comparison of the optical path through a flat interface solar cell (a) and through a rough interface solar cell (b). In case b, the rough interface scattered the incoming light leading to a longer optical path through the solar cell.*

This light scattering phenomenon can increase the solar cell current by 20~40 % (see 7.1) [Taneda 2007, Hüpkes 2006, Löffler 2005, Groenen 2005, Kluth 2004, Springer 2004, Müller 2004, Steinhauser 2005, Krc 2003, Faÿ 2003, Kluth 2001].

1.4 Aim and outline of this thesis

In this thesis, we investigate low pressure chemical vapor deposited zinc oxide layers doped with boron (LPCVD ZnO:B) for their used as transparent conductive contacts in thin film silicon solar cells.

The aim of this study is to improve and better understand the properties of LPCVD ZnO:B layers, especially on the optical and electrical properties of these films.

This work is organized in 3 parts : a presentation of the fabrication of LPCVD ZnO:B layers, a study of the layers properties and finally a discussion of their integration into the solar cells. We can express the

"guiding line" of this thesis as : "LPCVD ZnO, from the deposition process to final applications".

Chapter 2 "Basics on transparent conducting oxides" gives an overview of the literature relating to TCO. We summarize the physical laws that apply to TCO. We describe the most commonly used materials and deposition processes. We give a summary of TCO's applications as well as a recapitulative table of the typical TCO used in thin film silicon solar cells.

Chapter 3 "Characterization techniques" describes the experimental techniques used for this work.

Chapter 4 "Fabrication and growth of LPCVD ZnO:B films" summarizes previous results concerning LPCVD ZnO:B layers. We describe the deposition process and give a literature summary of the chemical reactions that occur during deposition. We summarize the influences of the deposition parameters on the layer properties. We describe the structural properties and present original results on elemental characterization of LPCVD ZnO:B films.

The chapter 5 "Optical properties of LPCVD ZnO:B films" focuses on experimental results and discussions about the optical properties of LPCVD ZnO:B layers grown with various parameters. We study their transmittance, reflectance and absorptance properties. We analyze their light scattering capability. Moreover, we discuss a theoretical model that explains the optical behavior of the films.

In chapter 6 "Electrical properties of LPCVD ZnO:B films" we analyze the electrical transport mechanisms of LPCVD ZnO:B layers deposited with various parameters. We establish which dominant electrical scattering factor occurs as a function of the film properties.

Chapter 7 "Integration of LPCVD ZnO:B films in silicon solar cells" relates the integration of LPCVD ZnO:B layers as a front contact in thin film silicon solar cells. We analyze the consequences of the changes of the ZnO film properties on the solar cell behavior. We study the light scattering role of various LPCVD ZnO:B layers in microcrystalline cells. We discuss the responsibility of the front TCO morphology in case of electrically-shunted solar cells.

Finally, chapter 8 "conclusion and perspectives" summarizes this work and proposes further perspectives for the improvement and better comprehension of LPCVD ZnO:B layers.

1.5 Contribution of this work to the research field

In the last years, the research on transparent contact for thin film solar cells has gained importance. This PhD thesis has contributed to the research field with the following elements :

♦ We prove that changing carrier density shifts the value of the band gap energy according to Burstein-Moss and band gap narrowing effects. In contrast to the Burnstein-Moss effect, the band gap narrowing reduces the gap and is only a factor 2 smaller than the BM shift. At energies slightly lower than Eg, we observe exponential band tails absorption due to states in the band gap [Steinhauser 2006].

♦ We show that the Drude model is sufficient to describe the NIR optical behavior of LPCVD ZnO:B films. We can attribute the small absorption of LPCVD ZnO:B films that remains in the visible range to residual free carrier absorption, also described by the Drude model [Steinhauser 2007].

♦ We establish an electrical model describing the conduction mechanisms in polycrystalline LPCVD ZnO:B layers (see 2.2.3) and verify it experimentally (see chapter 6). We find that the electron mobility is limited by grain boundary scattering at low carrier densities and by bulk scattering at high carrier densities. The transition between these regime is continuous in the range of doping level achievable in LPCVD ZnO:B films [Steinhauser 2007, Steinhauser 2007b].

♦ We explain the degradation of the electrical properties of LPCVD ZnO:B films during damp heat exposure using the electrical model establish previously (chapter 2). We link this degradation to an increase of trap states localized in grain boundaries. We also show and explain that films with a higher doping level are more stable during damp heat exposure [Steinhauser 2008].

♦ We use characterization techniques for the first time on LPCVD ZnO:B layers : First, we show that Raman analysis could provide information on the doping level of LPCVD ZnO:B (see 5.3). Then, we measure LPCVD ZnO:B layers with secondary ion mass spectroscopy and Rutherford back scattering spectroscopy techniques. The obtained results gives evidence of the non stoechiometry of LPCVD ZnO:B films and the presence of hydrogen and carbon in the layers (see 4.2.3). Finally, we establish a procedure using IR-lockin thermography, optical and electronic microscopy, and focus ion beam techniques to characterize and localize shunts due to particles in the solar cells (see 7.2.1).

♦ We observe different light scattering behaviors depending on the surface morphology of the LPCVD ZnO:B films. For samples with a small feature size, the haze factor is low, and light scattering occurs at large angles. For samples with large surface features, the haze factor is high, and light is scattered more close to the specular direction [Steinhauser 2005].

♦ We develop a LPCVD ZnO:B layer especially design for high efficiency µcSi:H and aSI:H/µcSi:H cells. This film has a high haze factor, a high mobility, and low absorptance and allows the fabrication of state of the art devices (see 7.3 and [Steinhauser 2005]).

To summarize, this study provides a more in-depth understanding of the electro-optical properties of the LPCVD ZnO:B film. This is of importance at a time where mass production equipment for such layers are being delivered worldwide to several modules manufacturers [Meier 2008].

CHAPTER 2 *Basics on transparent conductive oxides: fabrication, applications and theory*

This chapter presents an overview of the literature on Transparent Conducting Oxide (TCO). First, we describe the most commonly used TCO materials and their most common deposition processes. Then, we summarize the main applications of TCO. This section also focuses on TCO suitable for silicon thin film solar cell applications and gives a comparative description of the various TCO most commonly used for this application. Finally, we summarize the fundamental physical properties of TCO materials. We present the theoretical models that we established and applied to LPCVD ZnO:B layers in the frame of this study.

2.1 TCO fabrication, materials and applications

The materials named "Transparent Conducting Oxide" (TCO) are oxides that combine transparency in the visible spectral range with low electrical resistivity. TCO have been known for more than 50 years, and many reviews explain in detail their physical properties and fabrications [Exarhos 2007, Edwards 2004, Minami 2000, Freeman 2000, Gordon 1996, Hartnagel 1995, Chopra 1983]. This section presents the different TCO materials, their fabrication processes and their applications.

2.1.1 Deposition processes

Thin film TCO are obtained by various fabrication processes. The most commonly used techniques are the following :

- ***Sputtering***

Due to it simplicity and it large area capability, sputtering constitutes the most extensively used technique for the growth of TCO [Yim 2006, Dehuff 2005, Carcia 2003, Kluth 2001, Sundaram 1997]. A flat polycrystalline or amorphous film is obtained by deposition of sputtered species from plasma bombardment of a ceramic target or a metallic target in an oxidizing

atmosphere. A large choice of materials is grown by sputtering : ITO, ZnO, CdO, SnO_2, etc…. DC, RF magnetron or reactive sputtering are commonly applied. For instance, high quality TCO with a resistivity down to ~10^{-4} Ωcm and a visible transmittance *TT* > 80 % are obtained by sputtering. Sputtered TCO have been studied for several years (see for instance a detailed review by Ellmer [Ellmer 2000], describing the possibilities and issues of this technique).

- ***Chemical vapor deposition (CVD)***

Chemical vapor deposition is commonly used to deposit TCO. This technique consists of thermal decomposion of gases or vapors precursors in a vacuum reactor. The dissociated molecules interact with a hot substrate and form a thin film. Atmospheric pressure (APCVD), low pressure (LPCVD) or plasma enhanced (PECVD) chemical vapor depositions are all derivative techniques that can achieve very high quality TCO films. ZnO, SnO_2, ZnMgO, CdO are TCO that are easily grown by CVD. CVD has the advantage of being a moderate temperature process (150°C – 600°C), with large scale production capability and high growth rates [Li 2004, Kirchner 2003 Gessert 2001]. We give a detail description of the LPCVD process used in this study in chapter 4.

- ***Pulsed laser deposition (PLD)***

Pulsed laser deposition consists of focusing a train of high energy laser pulses on a target in a vaccum chamber. The molecular species, ablated from the target, reach the substrate and form a thin film. High quality films, i.e. epitaxial films, are obtained with this technique. A large variety of materials can be deposited including TCO [Christoulakis 2005, Grundmann 2005, Matsubara 2002].

- ***Spray pyrolysis***

Aerosol spray pyrolysis consists of spraying droplets of liquid precursors on a heated substrate. The solvent is then evaporated and the solutes become thermally pyrolized at the surface. ITO, SnO_2 or ZnO layers are deposited by this simple technique adapted to mass production and large area coatings [Prince 2002, Zhou 2001, Messing 1993].

- ***Wet technique (solution deposition)***

Solution deposition techniques such as the dip technique or the sol gel technique are well suited for the deposition of ITO and SnO_2 on large areas without any vacuum process. However, these methods lead to low film quality [Niessen 2002, Chatelon 1999, Exarhos 1995].

♦ ***Other methods***

Other methods are commonly employed in order to deposit TCO material. e.g. thermal evaporation, molecular beam epitaxy. See for instance [Chopra 1983] and [Exarhos 2007] for full reviews on TCO fabrication processes.

2.1.2 Materials

A lot of materials are used as transparent conductive materials. e.g. very thin films of metal and wide band gap oxides. The most popular are ITO, SnO_2, CdO and ZnO, fabricated with various processes and doping elements. The material characteristics strongly depend on the deposition process and on the process parameters. The substrate can also have a strong influence on the film's properties. Table 2.1 presents the main materials used as TCO with their possible dopant elements [Exarhos 2007, Koida 2007, Koida 2006, Minami 2005, Gordon 2000, Minami 2000, Freeman 2000, Ginley 2000, Minami 2000, Hartnagel 1995, Chopra 1983].

Gordon [Gordon 2000] tries to evaluate and classify these TCO for various applications using of a figure of merit. This figure of merit (*FM*) is the ratio of the electrical conductivity (σ) and the visible absorption coefficient (α) :

$$FM = \frac{\sigma}{\alpha} \qquad (2.1)$$

As the main characteristics of transparent conductive material are a high electrical conductivity and low absorption in the visible range, this definition of the figure of merit seems consistent. However, as discussed by Gordon himself, these two characteristics are not sufficient to evaluate TCO for the several different applications that they are planed to be use for. The question : "what is the best TCO ?" does not have an unique answer but strongly depends on the specific application envisaged.

The example of thin film solar cells is particularly demonstrative. For this application, we need high conductivity and transparency. But, another criterium is important : the capacity for the TCO to scatter the light. Faÿ [Faÿ 2006] redefines the figure of merit of Gordon in order to take into account this third parameter. However, the light trapping capability needed differs depending on the type of thin film solar cell (a-Si:H, micromorph, CIGS). In addition to this, the solar cell-TCO interface is essential. In fact, a better contact is achieved with TCO with a low workfunction at the n-Si interface and with TCO with a high workfunction at the p-Si interface. Finally, the cost and the resistance against the hydrogen plasma used

Table 2.1 *The main TCO materials with their doping elements are presented in this table with respect to their specific properties(compiled from [Exarhos 2007, Koida 2007, Koida 2006, Gordon 2000, Minami 2000]).*

Material	Dopant	Properties
Metal		
Ag		High plasma frequency, low deposition temperature
Oxide		
SnO_2	Sb, F, As, Nb, Ta	Low plasma frequency, high work function (best contact to p-Si), Thermal stability, mechanical durability, chemical durability, low toxicity, low cost
In_2O_3	Sn, Ge, Mo, F, Ti, Zr, Hf, Nb, Ta, W, Te, H	High conductivity, high plasma frequency, low deposition temperature
ZnO	Al, Ga, B, In, Y, Sc, F, V, Si, Ge, Ti, Zr, Hf	High transparency, low plasma frequency, low work function (best contact to n-Si), easy to etch, resistant to H plasma, low deposition temperature, low toxicity
CdO	In, Sn	
Nitride		
TiN		High plasma frequency, thermal stability, mechanical durability, easy to etch
Binary metal oxide compound		
Zn_2SnO_4		
$ZnSnO_3$		high work function (best contact to p-Si)
$Zn_2In_2O_5$		
Zn3In2O6		
$In_4Sn_3O_{12}$		
Cd_2SnO_4		High transparency, thermal stability
$CdSnO_3$		
$CdIn_2O_4$		
$MgIn_2O_4$		
$GaInO_3$	Sn,Ge	
$CdSb_2O_6$	Y	
Ternary metal oxide compound		
$Zn_2In_2O_5$-$In_4Sn_3O_{12}$		
$CdIn_2O_4$-Cd_2SnO_4		

during the Si cell deposition play also a crucial role for choosing a TCO for this application.

In this study, we invetigate zinc oxide. The advantage of ZnO compared to other TCO materials is a combination of low cost, large availability, non-toxicity, hydrogen plasma resistance, large area deposition and low temperature process capability [Gordon 2000, Minami 2005]. Recently, ZnO has attracted much attention within the scientific community not only as a TCO but as material suitable for optoelectronic devices i.e. UV light emitting diodes and lasers, detectors, and transparent transistors. Recent reviews and books give an extensive overview of ZnO properties and applications [Jagadish 2006, Özgür 2005, Nickel 2005]. A particular emphasis on the use of ZnO as thin film solar cell transparent contacts is given in [Ellmer 2007].

2.1.3 Applications

The following list gives an overview of the main applications of TCO. We summarize the criteria that influence the TCO choice, for each application, based on the reviews of [Exarhos 2007, Minami 2005, Gordon 2000].

- ***Low emissivity windows for building***

The high free electron reflectivity of the infrared radiation of TCO is used to improve the energy efficiency of building windows. In hot climates, TCO coated glass reflects the infrared portion of the incident sunlight off the buildings. In cold climates, infrared radiation is reflected back into the buildings. The same property is used for oven windows in order to lower the outside temperature to a safe level. For these applications, a short plasma wavelength and a high durability are needed. Tin oxide and TiN are generally well suited.

- ***Defrosting windows***

The combined resistivity and transparency of TCO material is used in defrosting windows. By applying an electrical current, the layer is heated due to Joule effects. Thus, such windows prevent moisture in the air from condensing. Low cost and high durability makes tin oxide a particular good candidate for this application.

- ***Flat panel displays***

TCO are used as front electrodes in flat panel displays to address the pixels. As good conductivity is needed, ITO is generally used. The low deposition temperature is also a factor in this application because the TCO need to be deposited on thermally sensitive devices.

Table 2.2 *TCO materials used in thin film solar cells applications. In addition to high conductivity and high transparency, light trapping capability are important criteria.*

TCO	LPCVD ZnO:B for a-Si:H cell	LPCVD ZnO:B for μc-Si:H cell	Sputtered and etched ZnO:Al	Expand thermal plasma CVD ZnO:Al	APCVD SnO_2:F Asahi U	APCVD SnO_2:F Asahi HU
Square resistance ($\Omega_\square$)	8	10	~ 5	~ 10	8	10
Thickness (μm)	2.2	5	~ 0.9	~ 1.1	0.76	-
Resistivity ($\times 10^{-3}$ Ωcm)	1.7	5.2	0.3 - 0.5	1.1	0.6	-
Hall mobility ($cm^2V^{-1}s^{-1}$)	30	40	30 - 40	38 - 44	~37	-
Hall carrier density ($\times 10^{20}$ cm^{-3})	1.2	0.3	4 - 6	0.7 - 2.5	~2.2	-
Visible range transparency (Absorptance @600nm %)	High (2)	Very High (0.7)	High (3)	High	High (3)	High (2.5)
Light scattering capability (Haze@ 600nm %)	High (38)	Very high (84)	Very high (54@700nm)	High (10-15)	High (14)	Very high (92)
Data from ref	[Faÿ 2003]	[Steinhauser 2005]	[Müller 2004, Kluth 2004]	[Löffler 2005, Groenen 2005]	[Taneda 2007]	[Taneda 2007]

- ***Transparent electronic***

The development of transparent electronics constitutes an activity in which the need for specific TCO is obvious. Touch panel controls, light emitting diodes, and thin film transistors are examples of applications. The main challenge in this domain is to fabricate p-type TCO in order to form p-n homojunctions. ITO is often use in these applications.

- ***Solar cells***

TCO are commonly used as electrodes in thin film solar cells, for instance : sputtered ITO is used on flexible silicon solar cells [Bailat 2005], sputtered ZnO:Al in copper indium gallium selenide (CIGS) cells [Campa 2007] or APCVD SnO_2 in cadmium telluride (CdTe) cells [Wu 2004].

Thin film silicon solar cells on glass substrates require the following characteristics : high conductivity, high transparency, light scattering capability, low cost, large area capability, high durability, and low deposition temperature.

Table 2.2 gives the characteristics of the principals TCO suitable for front contact in thin film silicon solar cells. As grown rough SnO_2 [Taneda 2007] or ZnO [Löffler 2005, Groenen 2005, Steinhauser 2005, Faÿ 2003] or sputtered and etched ZnO [Hüpkes 2006, Kluth 2004, Müller 2004] are common solutions to get sufficient light trapping inside the cells.

2.2 Thin film TCO physics

2.2.1 Band structure

TCO are wide band gap semiconductor oxides with an optical band gap energy E_g of typically 3.5 eV < E_g < 4.0 eV. This characteristic is necessary in order to have materials that are transparent in the visible range. Indeed, in materials with E_g > 3eV, the visible light energy $h\nu$ (1.65 eV < $h\nu$ < 3.26 eV) is insufficient to be absorbed by a band-to-band electron transition mechanism.

In order to be conductive, the presence of free electrons is necessary. This is achieved in TCO by either crystal defects or by incorporating extrinsic dopant elements in the crystalline network. The defects and the dopants act as shallow donor levels leading to such a high electron density in the conduction band that the Fermi level is positioned within the conduction band. In this case, the materials are called degenerate semiconductors, and

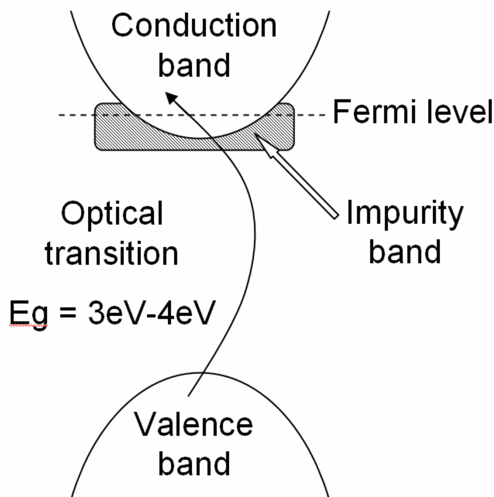

Figure 2.1 *The schematic energy band structure of a degenerate TCO.*

present a n-type conductivity. The onset of degeneracy usually takes place at a carrier concentration of around $10^{18}cm^{-3}$ [Mott 1987, Mott 1990].

The quantity of intrinsic defects in TCO materials is usually high enough to form an impurity band at the bottom of the conduction band [Edwards 2004], allowing conduction even at low temperature. TCO then behave like metals with a low density of electrons.

Figure 2.1 shows an illustration of a TCO band structure, which leads to an unusual combination of electrical conductivity and optical transparency in the visible range.

2.2.2 Optical properties

In TCO semiconductors, for photons of energy below to the band gap energy value, the band-to-band absorption takes place. As TCO are wide band gap semiconductors, this effect occurs in the UV part of the spectrum. As TCOs are usually not perfect crystals due to their fabrication process some defect states might absorb in the visible range as well. These phenomena are not explained further here, but the reader can refer to [Sze 1981, Adachi 1999, Adachi 1999b] for a comprehensive review on band gap and defects absorption.

The optical characteristics of a material can be deduced from its dielectric function. The complex frequency dependent dielectric function $\varepsilon(\omega)$ is related to the optical constants : n (refractive index) and k (extinction coefficient) through :

$$\sqrt{\varepsilon(\omega)} = n + ik \qquad (2.2)$$

For energy $h\nu << E_g$, in highly degenerate semiconductor materials such as TCO, the dielectric function can be described by the Drude model [Exarhos 2007].

In the Drude model, the local current density J of a free electron gases in a response to an electric field E oscillating at a frequency ω is given by [Drude 1900] :

$$\frac{dJ}{dt} + \frac{1}{\tau}J = \frac{N_{optic}e^2}{m}E \qquad (2.3)$$

where N_{optic} is carrier concentration, m the effective mass, e the free electron charge and τ the Drude scattering time. The dynamic conductivity $\sigma(\omega)$ is defined by :

$$J(\omega) = \sigma(\omega)E(\omega) \qquad (2.4)$$

$$\sigma(\omega) = \left(\frac{N_{optic}e^2}{m}\right)\left(\frac{1}{1+i\omega\tau}\right) \qquad (2.5)$$

Since Maxwell's corrected ampere law is :

$$\nabla \times H = J + i\omega\varepsilon_\infty\varepsilon_0 E = i\omega\varepsilon(\omega)\varepsilon_0 E \qquad (2.6)$$

the Drude form of the complex frequency dependent dielectric function $\varepsilon(\omega)=\varepsilon_1(\omega)+i\varepsilon_2(\omega)$ is expressed as :

$$\varepsilon(\omega) = \varepsilon_\infty + \frac{\sigma(\omega)}{i\omega\varepsilon_0} = \varepsilon_\infty - \frac{\omega_N^{\ 2}}{\omega^2 + i\Gamma\omega} \qquad (2.7)$$

where ε_∞ is the high frequency dielectric function, $\Gamma=1/\tau$ is the Drude damping frequency.

ω_N is the unscreened electrons plasma frequency defined by :

$$\omega_N{}^2 = \frac{N_{optic}e^2}{\varepsilon_0 m} \qquad (2.8)$$

where N_{optic} is the free electron density, e the electron charge, ε_0 the permittivity of free space and m the electron effective mass. With analogy with equation 2.14, the optical mobility μ_{optic} is given by :

$$\mu_{optic} = \frac{e}{\Gamma m} \qquad (2.9)$$

It is noticeable that electrical parameters such as the free electron density N_{optic} and the carrier mobility μ_{optic} are present in the dielectric function.

Using the Fresnel formula, the normal-incident reflectivity *TR* for a semi-infinite sample in air is expressed as [Hecht 1987] :

$$TR = \left|\frac{1-\sqrt{\varepsilon}}{1+\sqrt{\varepsilon}}\right|^2 = \frac{(1-n)^2 + n^2k^2}{(1+n)^2 + n^2k^2} \quad (2.10)$$

The normal-incident transmission *TT* of a finite sample thickness *d* considering internal reflection is given by [Hecht 1987] :

$$TT = \left|\frac{(1-\varepsilon(\omega))e^{i\frac{\omega}{c}\sqrt{\varepsilon(\omega)}d}}{1-\varepsilon(\omega)e^{i\frac{\omega}{c}\sqrt{\varepsilon(\omega)}d}}\right|^2 \qquad (2.11)$$

The absorption *A* can therefore be deduced :

$$A = 1 - TT - TR \qquad (2.12)$$

Optical properties of more complicated multilayer samples, (i.e. substrate + layer, rough interface) as well as non-normal incidence require additional computational steps. These are described in text books [Smith 1978, Tao 1994] and can be modeled with optical software such as GenPro [Zeman 2000].

In principle, we can calculate the optical spectra (i.e. the reflectance, the transmittance and the absorptance as a function of the incoming light frequency) knowing the dielectric function of a material. However, the most critical and difficult issue is to model the dielectric function itself.

The Drude dielectric function (expressed in equation 2.7) is not valid for the whole electromagnetic spectrum. Therefore, many dielectric function models can be used and even different models can be associated to fit experimental data over a broad frequency range.

In the near infrared region, the Drude model is well suited for the description of TCO optical properties. For the UV-visible region, the most commonly used optical models are Lorentz, Cauchy, Sellmeier, Tauc-Lorentz and Forouhi-Bloomer [Hong 2002, Losurdo 2002, Volintiru 2008, Logothetidis 2008].

Figure 2.2 shows the typical calculated reflectance, transmittance and absorptance curves of a TCO. These curves are simulated with in-house made software using the Drude model (for describing the infrared behavior) in addition to a Lorentz oscillator (in order to describe the band gap absorption) :

$$\varepsilon(\omega) = \varepsilon_\infty - \frac{\omega_N^{\;2}}{\omega^2 + i\Gamma\omega} + \frac{\Omega_N^{\;2}}{\Omega_0^{\;2} - \omega^2 - i\Omega_\Gamma\omega} \qquad (2.13)$$

where ε_∞ is the high frequency dielectric function, Γ and ω_N are the damping frequency and the unscreened plasma frequency of the Drude component, Ω_Γ, Ω_N, and Ω_0 are the damping frequency, the plasma frequency, and the resonant frequency of the Lorentz oscillator. The model considers a finite TCO layer deposited on a glass substrate. We adjust the model parameters in order to get typical TCO optical spectra (the parameters are listed in table 2.3).

Four separate regions come into view in these spectra, they are labeled with roman numbers on figure 2.2.

- In the UV region, i.e. region I, the band gap absorption takes place.
- In the visible and near-IR regions, i.e. region II, the TCO are transparent. Several factors limit the transmission in this region : Firstly, the reflection losses at the optical interface; secondly, the residual absorption, primarily due to free carrier but also to material defects. Finally, interference phenomena take place depending of the thickness of the layer [Hecht 1987].
- In the infrared region the Drude model explains the optical properties leading in region III mostly to free carrier absorption and in region IV mostly to free carrier reflection.

Table 2.3 *The parameters of the Drude + Lorentz oscillator model for the dielectric function (equation 2.13) used to obtain the optical spectra of figure 2.2.*

Thickness (μm)	ε_∞	ω_N (cm^{-1})	Γ (cm^{-1})	Ω_N (cm^{-1})	Ω_0 (cm^{-1})	Ω_Γ (cm^{-1})
1	3.8	7000	475	11000	32000	800

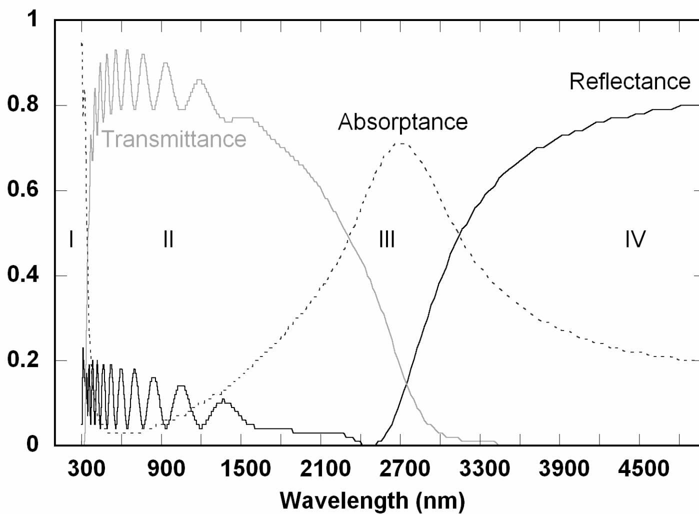

Figure 2.2 *The calculated transmittance, absorptance and reflectance for a typical TCO. The curves are obtained from a Drude + Lorentz oscillator model for the dielectric function (equation 2.11). The model considers a finite TCO layer deposited on a glass substrate. The model parameters were adjusted in order to get typical TCO's optical spetra and are listed in table 2.3.*

2.2.3 Electrical properties

TCO materials are degenerate semiconductors i.e. with the Fermi level within the conduction band. They are conductive and behave like metals. The free electron gas model of solids applies. The resistivity ρ and conductivity σ are given by [Sze 1981] :

$$\rho = \frac{1}{\sigma} = \frac{1}{eN\mu} = \frac{m}{Ne^2\tau} \quad (2.14)$$

where N is the free carrier density, $\mu = e\tau/m$ their mobility, e is the charge of the electron, m their effective mass and τ is the relaxation time between two scattering events.

Microscopically, various scattering events determine the mobility of the electrons. For bulk single crystalline TCO, the main scattering processes are the following [Ellmer 2008, Han 2008, Ellmer 2007, Özgür 2005, Look 2004] :

- ***Optical phonon scattering*** caused by the interaction of the electrons with the electric field induced by electric polarization associated with the lattice vibration at optical frequencies.
- ***Acoustic phonon scattering*** caused by the interaction of the electrons with the lattice deformations that correspond to pressure waves.
- ***Piezoelectric scattering*** caused by the interaction of electrons with the electric fields produced by the strain associated with phonons in the crystal.
- ***Neutral impurity scattering*** caused by the interaction of the electrons with uncharged defects.
- ***Ionized impurity scattering*** due to deflection of free carriers by the potential of a charge center originating from doping impurities. As TCO are usually heavily doped, this scattering mechanism is generally predominant.

Each scattering mechanism is described with its own scattering relaxation time τ_i and mobility μ_i.

The total scattering relaxation time τ_{Bulk} and the total mobility μ_{Bulk} for the material is deduced by applying Matthiessen's rule to the individual scattering relaxation times τ_i and mobility μ_i [Sze 1981] :

$$\frac{1}{\tau_{Bulk}} = \sum_i \frac{1}{\tau_i} \quad (2.15) \qquad \frac{1}{\mu_{Bulk}} = \sum_i \frac{1}{\mu_i} \quad (2.16)$$

The complete expression for each scattering process relaxation time τ_i can be found elsewhere (in reviews such as [Ellmer 2007]).

A simplified expression based on the empirical formula of Masetti [Masetti 1983] is used to describe the dependence of the bulk mobility μ_{Bulk} versus the free carrier density N:

$$\mu_{Bulk} \approx \mu_{Masseti} = \mu_{\min} + \frac{\mu_{\max} - \mu_{\min}}{1 + (N/N_{ref1})^{\alpha_1}} - \frac{\mu_1}{1 + (N_{ref2}/N)^{\alpha_2}} \quad (2.17)$$

where μ_{max} refers to the lattice mobility at low free carrier density, μ_{min} is the ionized impurity mobility at high carrier densities, μ_{min}-μ_1 represents the clustering mobility at very high carrier concentrations, N_{ref1}, N_{ref2}, α_1 and α_2 are empirical coefficients.

This model was originally developed for doped silicon. Ellmer [Ellmer 2001] used it to fit experimental data for ZnO produced using various deposition techniques. Table 2.4 summarizes the parameters found by Ellmer for ZnO regarding equation 2.17.

All the scattering phenomena described previously are related to the bulk single crystal material. However, thin film TCOs are usually polycrystalline. In this case, an additional scattering mechanism occurs due to presence of grain boundaries : the grain boundary scattering. Grain boundaries are present in thin film TCO due to polycrystalline nature of the film induced by the fabrication process.

As described by Seto in the case of polycrystalline silicon [Seto 1975], acceptor centers are localized in grain boundaries, which captures electrons from the conduction band. The grain boundaries are charged negatively and a space charge region extends into the crystallite forming a "back-to-back" schottky potential barrier [Orton 1981, Orton 1980, Seto 1975].

Considering a degenerate ZnO layer, the mean free path (l) of the electron is estimated at l~10 nm [Myong 2007, Shimakawa 2007, Mahan 1978]. Typical grain size for thin film ZnO are about 300 nm. Therefore, for the following

calculations, we assume that the electron mean free path is smaller than the grain size.

TCO are generally heavily n-type doped, therefore the trap density (N_t) at grain boundaries is lower than the carrier concentration within a grain:

$$N_t < NL \qquad (2.18)$$

where N_t is the trap density, N the carrier density inside the grain and L the grain size.

Considering a single grain of length L with a single grain boundary localized at $L/2$ and with Q_t the total traps charge and W the depletion region width, we have [Seto 1975] :

$$Q_t = -eN_t = eNW \qquad (2.19)$$

$$W = \frac{N_t}{N} \qquad (2.20)$$

The 1D Poisson's equation in the space charge region yields the spatial variation of the electric potential V [Seto 1975]:

$$\frac{d^2V(x)}{dx^2} = \frac{eN}{\varepsilon\varepsilon_0} \qquad \left(\frac{L}{2} - \frac{W}{2} < |x| < \frac{L}{2}\right) \qquad (2.21)$$

where ε is the dielectric permittivity of the material, ε_0 the dielectric permittivity of free space and x the position within the grain.

Integrating equation 2.21 twice and applying the boundary conditions : $V(x)$ is continuous and $dV/dx = 0$ at $x = L$ gives :

$$V(x) = \left(\frac{eN}{2\varepsilon\varepsilon_0}\right)\left(x - \left(\frac{L}{2} - \frac{W}{2}\right)\right)^2 + V_0 \qquad \left(\frac{L}{2} - \frac{W}{2} < |x| < \frac{L}{2}\right) \qquad (2.22)$$

where V_0 is the potential of the conduction band edge.

Table 2.4 *The fit parameters for silicon and zinc oxide according to equation 2.17, from [Ellmer 2001].*

Parameter	Si:P	Si:B	ZnO
μ_{max} ($cm^2V^{-1}s^{-1}$) lattice mobility	1414	470.5	200
μ_{min} ($cm^2V^{-1}s^{-1}$) ionized impurity mobility	68.5	44.9	50
μ_{min}-μ_1 ($cm^2V^{-1}s^{-1}$) clustering mobility	12.4	15.9	10
N_{ref1} (cm^{-3})	$9.2\ 10^{16}$	$2.23\ 10^{17}$	$1.5\ 10^{18}$
α_1	0.711	0.719	1
N_{ref2} (cm^{-3})	$3.41\ 10^{20}$	$6.1\ 10^{20}$	$6\ 10^{20}$
α_2	1.98	2	2

Table 2.5 *The depletion length and barrier height calculated from equations 2.20 and 2.23 for a back-to-back schottky barrier in case of heavily doped ZnO : $N_t < NL$. The permittivity value taken for the calculation is $\varepsilon = 8.12$.*

Trap density N_t (cm^{-2})	Carrier density N (cm^{-3})		
	$5\ 10^{19}$	$1\ 10^{20}$	$2\ 10^{20}$
$1\ 10^{12}$	W = 0.2 nm eV_b = 0.6 meV	W = 0.1 nm eV_b = 0.3 meV	W = 0.05 nm eV_b = 0.1 meV
$1\ 10^{13}$	W = 2 nm eV_b = 56 meV	W = 1 nm eV_b = 28 meV	W = 0.5 nm eV_b = 14 meV
$5\ 10^{13}$	W = 10 nm eV_b = 1393 meV	W = 5 nm eV_b = 696 meV	W = 2.5 nm eV_b = 348 meV

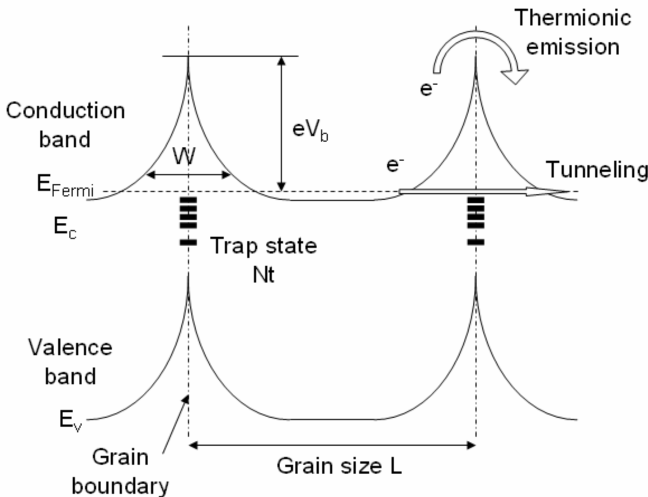

Figure 2.3 *The schematic band energy diagram of a TCO grain of length L. Potential barriers of height eV_b are formed at grain boundaries due to electronic trap states of density Nt. The thermionic emission and the tunneling current flows are illustrated.*

The maximum barrier height eV_b is given at $x = L/2$ by:

$$eV_b = \frac{e^2 N_t^{\ 2}}{8\varepsilon\varepsilon_0 N} \qquad (2.23)$$

It should be noted that the barrier width W and height eV_b are inversely proportional to the carrier density N. Table 2.5 gives calculated values for W and eV_b in ZnO for varying free carrier and trap density densities. Due to the high carrier density, the values found for the barrier height (typically a few meV) and the barrier width (typically a few nm) are very low. In these cases, the current flow occurs both by thermionic emission over the barrier and by tunneling through the barrier. Note that the very small value of W ($W < 1$ nm) has no real physical meaning and we should only interpret them qualitatively.

Figure 2.3 illustrates the band bending in such polycrystalline materials. Current flow trough the barrier could be described by various mechanisms i.e. Thermionic emission, field emission (tunneling), thermionic field emission or variable range hopping transport [Myong 2007, Sze 1981]. In our model, we choose two possible transport paths i.e. thermionic emission and tunneling. They are also illustrated in figure 2.3.

For the classical thermionic emission, based on the use of Maxwell-Boltzmann statistic, the current density is given by [Seto 1975]:

$$J_{th} = V_{gb} \frac{e^2 N}{\sqrt{2\pi mkT}} e^{\left(\frac{-eV_b}{kT}\right)} \qquad (2.24)$$

where V_{gb} is the applied voltage on the grain boundary, k the Boltzmann constant, TT the temperature and m the effective mass.

In a one dimensional grain boundary of width W we have :

$$J_{th} = \frac{V_{gb}\sigma_{th}}{W} = \frac{V_{gb} eN\mu_{th}}{W} \qquad (2.25)$$

This expression leads to a thermionic mobility equal to:

$$\mu_{th} = \frac{eW}{\sqrt{2\pi mkT}} e^{\left(\frac{-eV_b}{kT}\right)} \qquad (2.26)$$

Considering that the tunneling current through a potential barrier of height eV_b and width W is proportional to the tunneling probability (i.e. the exponential term) [Sze 1981, Simmons 1963], the expression for the tunneling current is:

$$J_{tun} = J_0 e^{\left(\frac{-4\pi W\sqrt{2meV_b}}{h}\right)} \qquad (2.27)$$

where h is the Planck's constant.

The prefactor J_0 could be expressed as [Mahan 1978]:

$$J_0 = Nev_D \qquad (2.28)$$

The drift speed v_D can be expressed in terms of the accelerating electric field $E = V_{gb}/W$, the electron mass m, and the characteristic time between collisions τ_F [Sze 1981] :

$$v_D = \frac{e}{m} E\tau_F = \frac{e}{m} E \frac{l_{tun}}{v_F} \qquad (2.29)$$

where, l_{tun} is the mean free path of the electron and v_F is the Fermi velocity given by [Sze 1981] :

$$v_F = \frac{\hbar}{m}(3\pi^2 N)^{1/3} \qquad (2.30)$$

where h is the Planck's constant. To achieve reasonable tunneling current, l_{tun} is of the order of magnitude of the nanometer [Myong 2007, Shimakawa 2007, Mahan 1978].

The complete expression for the tunneling current is then:

$$J_{tun} = \frac{V_{gb} N e^2 l_{tun}}{W\hbar(3\pi^2 N)^{1/3}} e^{\left(\frac{-4\pi W\sqrt{2meV_b}}{h}\right)} \qquad (2.31)$$

In a one-dimensional grain boundary of width W we have:

$$J_{tun} = \frac{V_{gb}\sigma_{tun}}{W} = \frac{V_{gb} eN\mu_{tun}}{W} \qquad (2.32)$$

Therefore, the tunneling mobility is given by:

$$\mu_{tun} = \frac{el_{tun}}{\hbar(3\pi^2 N)^{1/3}} e^{\left(\frac{-4\pi W\sqrt{2meV_b}}{h}\right)} \qquad (2.33)$$

Figure 2.4 is the equivalent circuit chosen to model the conductivity of a polycrystalline ZnO layer. It considers the grain resistivity and the two possible current path at the grain boundary (i.e. thermionic emission and tunneling).

In this case the current flow is:

$$J = J_B = J_{tun} + J_{th} \qquad (2.34)$$

$$J_{tun} + J_{th} = J = \frac{V_{gb}\sigma_{tun}}{W} + \frac{V_{gb}\sigma_{th}}{W} = \frac{V_{gb}eN}{W}(\mu_{th} + \mu_{tun}) \qquad (2.35)$$

$$V_{gb} = \frac{JW}{eN}\frac{1}{\mu_{th} + \mu_{tun}} \qquad (2.36)$$

$$J_B = J = \frac{V_B\sigma_B}{(L-W)/2} = \frac{V_B eN}{(L-W)/2}\mu_{Masetti} \qquad (2.37)$$

$$V_B = \frac{J(L-W)/2}{eN}\frac{1}{\mu_{Masetti}} \qquad (2.38)$$

$$J = \frac{V\sigma}{L} = \frac{VeN}{L}\mu \qquad (2.39)$$

$$V = \frac{L}{eN}\frac{1}{\mu} \qquad (2.40)$$

the total voltage is:

$$V = 2V_B + V_{gb} \qquad (2.41)$$

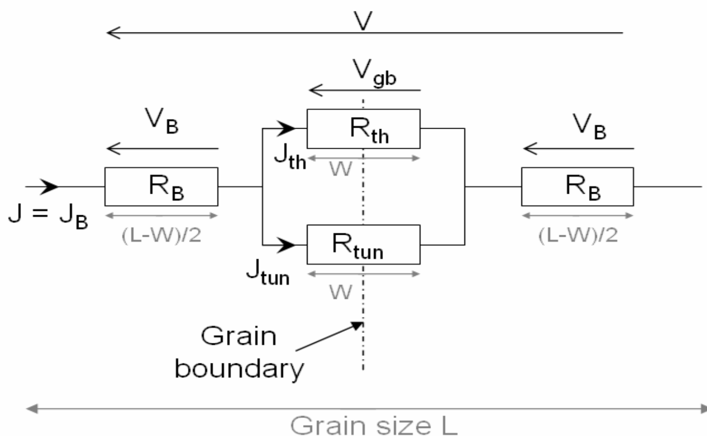

Figure 2.4 *The equivalent circuit chosen to model the resistivity of a polycrystalline ZnO layer.*

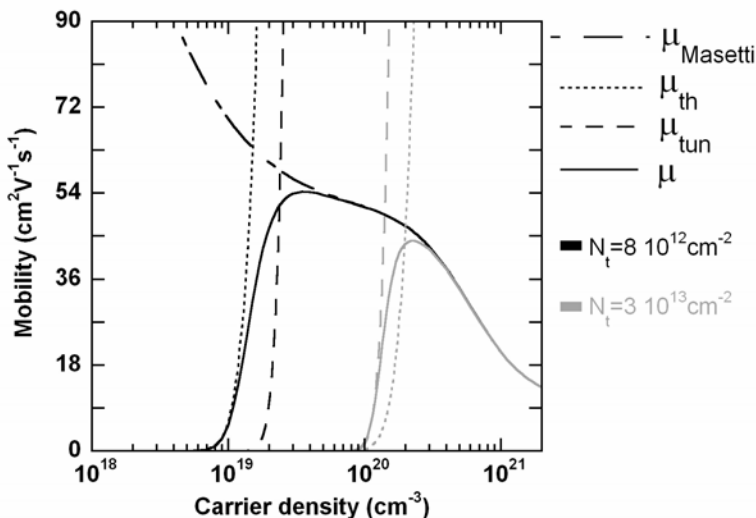

Figure 2.5 *The calculated mobility contributions for polycrystalline ZnO from equations 2.17, 2.28,and 2.35.The parameters are set to L = 300 nm, m = 0.28m_e, T = 300 K and l_{tun} = 5 nm, the Masetti parameters are taken from table 2.1. We deduce the total mobility μ from equation 2.42.The black curves are given for N_t = 8 10^{12} cm^{-2}, the gray curves for N_t = 3 $10^{13}$$cm^{-2}$.*

Therefore, the effective mobility μ is:

$$\frac{1}{\mu} = \frac{L-W}{L}\left(\frac{1}{\mu_{Masetti}}\right) + \frac{W}{L}\left(\frac{1}{\mu_{th} + \mu_{tun}}\right) \qquad (2.42)$$

Figure 2.5 shows the different calculated contributions of the mobility regarding equations 2.17, 2.28, 2.35, and the deduced total mobility from equation 2.42. For typical ZnO layer the parameters are : L = 300 nm, ε_0 = 8.12, l_{tun} = 5 nm and two values of trap density : $N_t = 8\ 10^{12}$ cm^{-2} and $N_t = 3\ 10^{13}$ cm^{-2}.

Here, it clearly appears that grain boundary scattering governs the mobility for low carrier density. In contrast, the bulk mobility described by the Masetti equation dominated the mobility behavior for high carrier density.

2.2.4 Conclusions

The basic physical properties of TCO have been presented. We established theoretical models to describe the optical and electrical properties of LPCVD ZnO:B layers.

Knowing theoretical models that applied to the properties of LPCVD ZnO:B films allow to predict their variation tendencies and their limit. These theoretical predictions give, therefore, useful rules for the optimization of LPCVD ZnO:B films as contact layers in thin film solar cells.

In the next chapters, we refer to these models in order to describe and discuss experimental results.

CHAPTER 3

Characterization techniques

In this chapter, we present the main techniques used in this thesis to characterize TCO and solar cells.

3.1 Structural characterizations

3.1.1 Thickness

LPCVD ZnO:B layers are deposited on AF45 glass. In order to measure the thickness of these films we construct a mesa or a step.

Usually, we obtain these features by wet etching of the ZnO film after masking a part of the layer with a plastic paint (plastik70). Then, we remove the remaining plastic by immersing it in acetone. A second method consists of a lift-off technique. We draw the step contour with ink directly on the glass before the ZnO deposition. After the deposition, we remove the ink and the ZnO that covers it using acetone.

We measure an average thickness d of the obtained step with a stylus Alpha-Step 200 profilometer, having a resolution of +/-5 nm. For rough samples, we evaluate the thickness by averaging the heights of a 1 mm scan length.

3.1.2 Electron microscopy (SEM, EDX, TEM, FIB)

The electron microscopy techniques consist of focusing an electron beam on the sample and forming an image from the measured scattered electron. With these methods, we can obtain surface micrographs, chemical information, and diffraction patterns. In this study, we use scanning electron microscopy (SEM), energy-dispersive X-ray spectroscopy (EDX), and transmission electron microscopy (TEM).

An ESEM-FEG Philips XL300 microscope is used to visualize the surface of the ZnO layers. We use the same equipment in EDX mode in order to perform chemical analysis.

A TEM Philips CM200 is used to obtain precise micrographs of the cross-sections of samples.

We obtain the cross-sections of defective devices presented in chapter 7 with a Zeiss NVision 40 CrossBeam FIB coupled to an ESEM microscope. The FIB instrument focuses Ga ions and accelerates them through electrostatic lenses. The high energy of the accelerated Ga ions permits to precisely cut cross-sections of the samples.

3.1.3 Atomic force microscopy (AFM)

Atomic force microscopy AFM consists of scanning the surface of the sample using a cantilever with a sharp tip at its end. When this tip is close to the sample surface, interaction between the tip and the sample take place. This interaction leads to a deflection of the cantilever, which is measured using a laser technique. The scanning of the surface by the cantilever is controlled through a piezoelectric tube. Images obtained with this technique gives 3D information of the surface topology.

We performed the AFM measurements for this work in the non-contact (tapping) mode on a scanning probe microscope from Vista Burleigh Instruments. The scan resolution is 256×256 points for a scan size of 5×5 μm.

The Root Mean Square values of the surface roughness σ_{RMS} is determined from Atomic Force Microscopy (AFM) measurements using :

$$\sigma_{RMS} = \sqrt{\frac{1}{n}\sum_{i=1}^{n} z_i^2} \qquad (3.1)$$

where n is the total number of data points, and z_i is the vertical distance from the average line of the ith data point.

3.1.4 X-ray diffraction (XRD)

We measured the crystallographic orientation of the layers using X-ray diffraction (XRD) spectroscopy technique. The principle, illustrated in figure 3.1, consists of focusing a X-ray beam on the sample with an angle θ and measuring the angles of diffraction of the scattered beam.

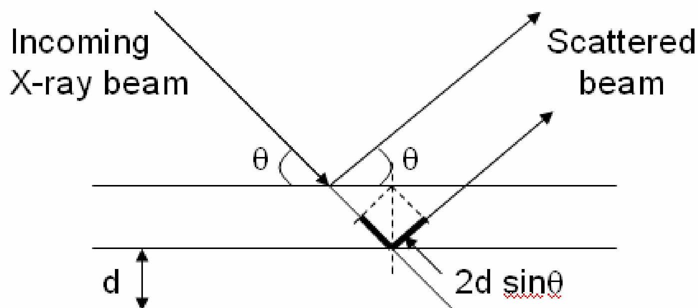

Figure 3.1 *The schematic diagram of the* θ*-*2θ *configuration for XRD measurements.*

When Bragg's law (equation 3.2) is verified, constructive interferences are formed and an intensity peak is measured.

$$2d\sin\theta = n\lambda \qquad (3.2)$$

d is the distance between the lattice plan, λ the X-ray wavelength, n the diffraction order, θ and the angle defined on figure 3.1.

The X-ray spectrometer employed during this study is a Philips PW3020 diffractometer used in the Bragg-Brentano geometry (θ-2θ scans). We used an accelerating voltage of 30 kV and a current of 40 mA to produce Cu Kα radiation at a wavelength of 1.5418 Å. The diffraction spectrum of ZnO layers measured in this configuration showed a maxima of intensity, which correspond to crystalline plane orientations parallel to the substrate.

3.1.5 Rutherford backscattering spectroscopy (RBS)

Rutherford Backscattering Spectroscopy RBS is an ion scattering technique used for elemental thin film analysis. During an RBS measurement, high-energy (MeV) He++ ions are directed onto a sample and the energy distribution and yield of the backscattered He++ ions at a given angle is recorded. Since the backscattering cross-section for each element is known, it is possible to obtain quantitative depth profiles from the RBS spectra [EAG 2008]. For this work, an external company, CAFI-EIAJ, measured the samples using an RBS instrument using a 2 Mev proton beam.

3.1.6 Secondary ion mass spectroscopy (SIMS)

Secondary ion mass spectroscopy SIMS is a measurement technique used for elemental analysis of thin film samples. A high energy primary ion beam is directed on the sample whose composition is to be determined. The interaction of the primary ions with the sample surface produces secondary particles (atoms and small molecules) that are ejected from the sample. An electrical field between the sample and an extraction lens extracts the charged particles of one polarity (i.e. secondary ions) from the sputtering area. These accelerated secondary ions constitute a secondary ion beam, which lead into a mass spectrometer. There, an ion detector (i.e. an electron multiplier, a Faraday cup or a channel plate), count the secondary ions by mass. The count rate of different secondary ion species gives information about the composition of the sample in the sputtered area.

SIMS technique measures most of the elements of the periodic table, including hydrogen, with a typical resolution of a few ppm. During a measurement, the sample is slowly sputtered away, therefore SIMS is capable of measuring depth profiles [Uni St Louis 2008]. For this study, an external company, Cascade Scientific Ltd, measured the samples using a PHI quadrupole SIMS instrument.

3.2 Optical characterizations

3.2.1 Ultra-Violet / Visible / Near InfraRed spectroscopy

We measured the sample transmittance and reflectance spectra with a Perkin Elmer dual beam UV/VIS/NIR Lambda 900 spectrometer equipped with an integrating sphere. Deuterium and halogen lamps are used as light sources. A grating monochromator produces a monochromatic beam over the range of 200 nm to 3000 nm. This monochromatic light is directed on the sample, which is placed at the entrance port of the integrating sphere. The integrating sphere reflects the incoming light beam homogeneously. In the dual beam technique, a second monochromatic beam enters the sphere through an open port : the "reference beam". A chopper technique successively lets enter into the integrating sphere : no beam, the "sample beam", and the "reference beam". Detectors (a photomultiplier and a lead sulphide detector) placed inside the integrating sphere measure the related intensities. The change in reflectivity of the sphere due to the open port and the sample is deduce from measurement of the intensity of the dark and the "reference beam" and taken into account to correct the sample beam intensity.

This equipment measures optical reflectance and transmittance of samples that diffuse the light. We acquire a first intensity spectrum with a 100 % reflectance reference (spectralon) without a sample mount. The intensity measured $I_{background}$ is used as 100 % background. Then, we place the sample at the entrance of the sphere and we acquire a second intensity spectrum. The total transmittance (*TT*) is deduced from the ratio between the measured intensity I_{sample} and the background intensity $I_{background}$:

$$TT = \frac{I_{sample}}{I_{background}} \qquad (3.3)$$

We obtain the diffuse transmittance (*DT*) spectrum using the same procedure as for *TT*, but with an open port at the back side of the sphere. This hole lets the specular transmitted light get out of the sphere, thus only the diffuse part stays inside the sphere and is measured.

We measure the total reflectance (*TR*) by putting the sample at the back of the sphere, tilted at a 7° angle in order to not let the primary reflection get out of the sphere through the incoming beam port. We measure the diffuse reflectance (*DR*) by opening a port that allows the primary reflection of the sample to leave the sphere. Figure 3.2 illustrates the different configurations of the sample on the integrating sphere used to measure *TT*, *DT*, *RT* and *DR*.

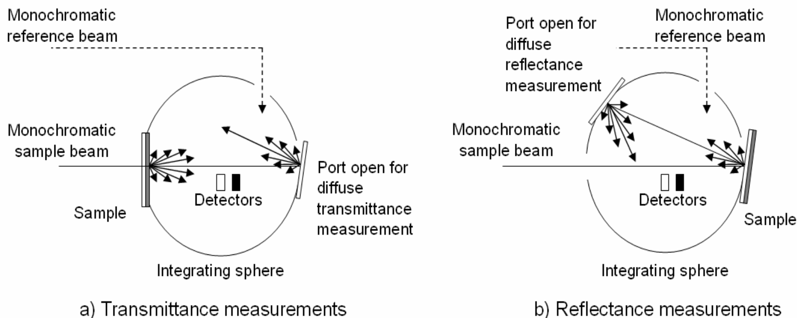

Figure 3.2 *The schematic diagram of the configurations used to measure the transmittance and reflectance with an integrating sphere.*

The haze factor $H(\lambda)$ is defined as the ratio between the diffuse transmittance $DT(\lambda)$ and the total transmittance $TT(\lambda)$:

$$H(\lambda) = \frac{DT(\lambda)}{TT(\lambda)} \quad (3.4)$$

We take the haze factor value at 600 nm as an indicator for the light scattering capability of diffusing TCOs used in thin film solar cell applications.

3.2.2 Fourier Transform InfraRed spectroscopy (FTIR)

We measure the reflectance of the samples in the infrared region with a Perkin Elmer 1720X FTIR spectrometer equipped with a specular reflectance accessory. Light from a broadband infrared source enters an interferometer and is directed on the sample. The reflected intensity is measured on a detector and the reflectance spectrum can be reconstructed using a Fourier transform.

3.2.3 Angular distribution function (ADF)

We measure the angular distribution function with a setup built at the IMT. A 632.8 HeNe laser beam is used as source and directed under normal incidence on the sample, usually from the glass side. A silicon detector mounted on a step motor rotate around the sample and measure the diffused beam intensity at each angle with a lock-in technique. Measurements are performed either in reflection or in transmission.

It is important to compare normalized ADF. Since the haze values determine the total amount of scattered light, comparison of normalized ADF gives us more clear information about the directional dependency of scattered light. We chose the normalization factors such that the maximum values of the absolute intensity for each sample are equal.

3.2.4 Ellipsometry spectroscopy

A light beam is linearly polarized by a polarizer and reflected onto the sample. After reflection, a detector through a second polarizer, called an analyzer, measures the change in polarization, at an angle ϕ. r_s and r_p are the normalized reflection amplitudes of the two components of the incident polarized light (s correspond to oscillation perpendicular to the plane of incidence and parallel to the sample surface, and p to oscillation parallel to the plane of incidence).

The fundamental equation of ellipsometry express the mesurable quantity r_p/r_s as :

$$\rho_{el} = \frac{r_p}{r_s} = \tan \Psi e^{i\Delta} \qquad (3.5)$$

where *tan* Ψ is the amplitude, Δ the phase shift and ρ_{el} the ellipsometry reflection coefficient.

A dielectric model analysis is performed in order to extract the sample's properties (the dielectric function tensor ε, the complex refractive indexes, and the thickness) as well as to identify possible roughness or porosity. Equation 3.6 is an example of a model valid for a semi infinite abrupt non-transparent medium.

$$\varepsilon = (n + ik)^2 = \sin^2 \phi \left(1 + \tan^2 \phi \frac{(1 - \rho_{el})^2}{(1 + \rho_{el})^2} \right) \qquad (3.6)$$

where n is the refraction index, k the absorption coefficient and ϕ the angle of incidence.

3.2.5 Raman spectroscopy

Micro-Raman spectroscopy consists of a laser excitation beam that is focused through a microscope on the sample surface. The back scattered light intensity is measured as a function of its frequency shift. These shifts are induced by the inelastic energy exchange between photons and vibrational modes. The spectra obtained gives information on the bonding environment in the sample.

Raman spectra measurement were made at the Hahn Meitner Institut in Berlin (Germany). The laser source used is a helium-neon laser emitting at 633 nm. The integration time is about several minutes.

3.3 Electrical characterizations

3.3.1 Four probe square resistance

We applied four in-line metallic probes spaced at 2 mm at the surface of the samples. A small current I is source between the two external probes and the resulting voltage drop U is measured between the two internal probes.

We deduce the square resistance $R_\square$ from :

$$R_\square = C\frac{U}{I} \qquad (3.7)$$

where C is a constant dependent on the geometry of the sample [Smits 1958], for a infinite sample C = 4.53. The resistivity ρ of the sample is evaluated using :

$$\rho = R_\square d \qquad (3.8)$$

where d is the sample thickness.

3.3.2 Hall effect

We systematically investigate the carrier mobility μ_{Hall} and the carrier density N_{Hall} of LPCVD ZnO layers with an HEM-3000 Hall system.

This equipment first measures the resistivity of the samples with the Van der Pauw configuration [Van d Pauw 1958] as described in figure 3.3. Four contacts A,B,C,D, are ultrasonically soldered at the corners of about 1 cm^2 samples.

A small current I_{AB} is applied between A and B and the resulting voltage V_{DC} between D and C is measured. The same measurements are repeated for a source current I_{BC} between B and C and a voltage V_{AD} measured between A and D. Two resistance values R_1 and R_2 are deduced :

$$R_1 = \frac{V_{DC}}{I_{AB}} \quad (3.9) \qquad R_2 = \frac{V_{AD}}{I_{BC}} \quad (3.10)$$

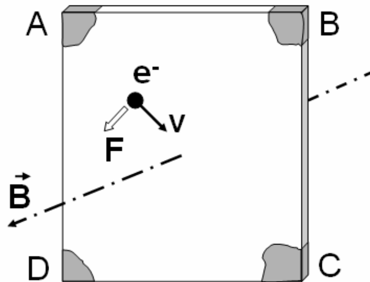

Figure 3.3 *The schematic diagram of the Van der Pauw configurations.*

The square resistance $R_\square$ is then deduced by numerically resolving the equation :

$$e^{\left(\frac{-\pi R_1}{R_\square}\right)} + e^{\left(\frac{-\pi R_2}{R_\square}\right)} = 1 \qquad (3.11)$$

The resistivity is finally calculated from the square resistance and the thickness using equation 3.8. ZnO resistivity measure with the Hall measurement setup and with the 4 probes setup (3.3.1) are consistent.

Then we place the sample in a 0.51 T magnetic field B. The Lorentz force F is applied at the moving charge carriers :

$$F = ev \times B \qquad (3.12)$$

where e is the charge of the electron.

When a current I_{AC} is applied between A and C, the electrons are deviated by the Hall force and induce a voltage V_{BD} between B and D. The resistance R_3 is define as :

$$R_3 = \frac{V_{BD}}{I_{AC}} \qquad (3.13)$$

The Hall coefficient R_H is given by :

$$R_H = \frac{d}{B} \Delta R_3 \qquad (3.14)$$

where d is the thickness, B the magnetic field and ΔR_3 is the difference between the R_3 resistance value with and without the applied magnetic field.

The Hall mobility μ_{Hall} is given by :

$$\mu_H = \left| \frac{R_H}{\rho} \right| \qquad (3.15)$$

where ρ is the resistivity.

The carrier density N_{Hall} can therefore be deduced using:

$$\frac{1}{\rho} = eN_{Hall}\mu_{Hall} \qquad (3.16)$$

3.3.3 Temperature dependence of the conductivity

We measure the temperature dependence of the conductivity using a four-probe configuration (see 3.3.1). We place the samples in a cryostat cooled with liquid helium. The temperature is precisely controlled with a heater using a feedback loop based on an in situ temperature sensor measurement. A Keitley 2600 sourcemeter executes the current voltage measurements during a temperature ramp from 300 K to 30 K.

3.4 Solar cell characterizations

3.4.1 Solar cell deposition

The solar cells were fabricated by Very High Frequency plasma-enhanced chemical vapour deposition (VHF-PECVD). See [Meier 2004] for a comprehensive review about the VHF-PECVD technique for deposition of amorphous and microcrystalline solar cells.

3.4.2 Illuminated current-voltage measurement

The current voltage characteristics of the illuminated solar cells are obtained under a class A WXS140s Wacom sun simulator. The 1000 Wm^{-1} AM1.5G solar spectrum is reproduced with two continuous light sources, a xenon lamp and a halogen lamp. The AM1.5G spectrum corresponds to the sun energy incident normalized at 1000 $W.m^{-2}$, at each wavelength, on a 37° sun-facing tilted surface relative to the horizontal under standard atmospheric conditions (see [IEC 2005] for a complete description of these standards conditions). The open-circuit voltage (V_{oc}), the fill factor (FF), and the short-current density (J_{sc}) are deduced from a four probe voltage sweep measurement operated with a Keithley 2700 sourcemeter. We performed the measurements at a cell temperature of 25°C stabilized by ventilation.

3.4.3 External quantum efficiency

The external quantum efficiency (EQE) (i.e. the number of electrons produced in the device per incident photon in short circuit condition) is measured with a custom made setup. Using a lockin technique, the cell current density is measured at each wavelength and divided by the incident photon flux determined with a calibrated reference detector. We can expose the cell to a stabilized white bias light in order to measured the device performance under its operating conditions. Bias voltage can be applied. Under sufficient reverse bias, the recombination losses are negligible and

all generated electron-hole pairs are collected, allowing us to distinguish between the optical and the collection losses.

3.4.4 Lockin thermography

Lockin thermography measurements localize electrical shunts in solar cells (or other electrical components). Figure 3.4 illustrates the principles of functioning of the lockin thermography. A periodic square bias voltage is applied to the sample. The current flows predominantly in the shunts and induces a local heat dissipation that is analyzed by an infrared lockin camera. The IR camera is coupled to an optical microscope, allowing the precise determination of the position of the shunt.

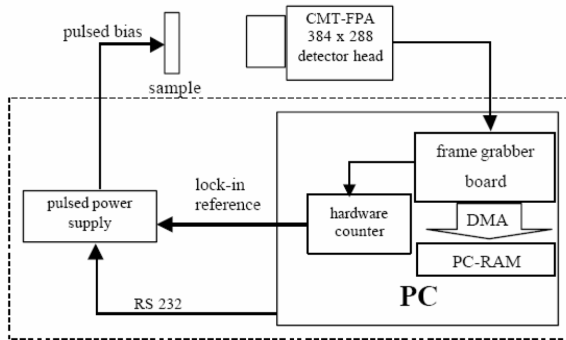

Figure 3.4 *The schematic diagram of the lock-in thermography.*

CHAPTER 4 *Fabrication and growth of LPCVD ZnO:B films*

This chapter is a short summary of detailed investigations made by Faÿ and Selvan [Faÿ 2006, Faÿ 2005, Faÿ 2003, Faÿ 2000, Selvan 1998] on the LPCVD ZnO:B process used in this study. Their studies, summarized below, allow the fabrication of state of the art low pressure chemical vapor deposition ZnO layers doped with boron (LPCVD ZnO:B). As we investigate the properties of these films in detail in the following chapters, it is useful to have the most important effects of the fabrication parameters in mind.

First, we describe the LPCVD deposition system and the chemical reactions that occur during growth. We summarize the correlations between the deposition parameters and the film's properties. We recapitulate the deposition parameters and the layers characteristics of typical LPCVD ZnO:B films designed for thin film silicon solar cells. Then, we summarize the structural properties of layers. Finally, we present results obtained within the framework of this study, on the elemental composition of the LPCVD ZnO:B layers.

4.1 Fabrication of LPCVD ZnO:B

4.1.1 Low pressure chemical vapor deposition system

The ZnO layers are made using low pressure chemical vapor deposition (LPCVD). Basically, it consists of mixing reactant gases (or vapors) in order to grow a film on a heated substrate (see 2.2.1) [Pierson 1999].

Figures 4.1 and 4.2 show a schematic view and a picture of the LPCVD reactor used in this study, respectively. A root pump evacuates a vacuum chamber. We obtain base vacuum levels inferior to 1 µbar. During deposition, the pressure is controlled by changing the pumping speed via a butterfly valve. The usual deposition pressure is about 0.5 mbar.

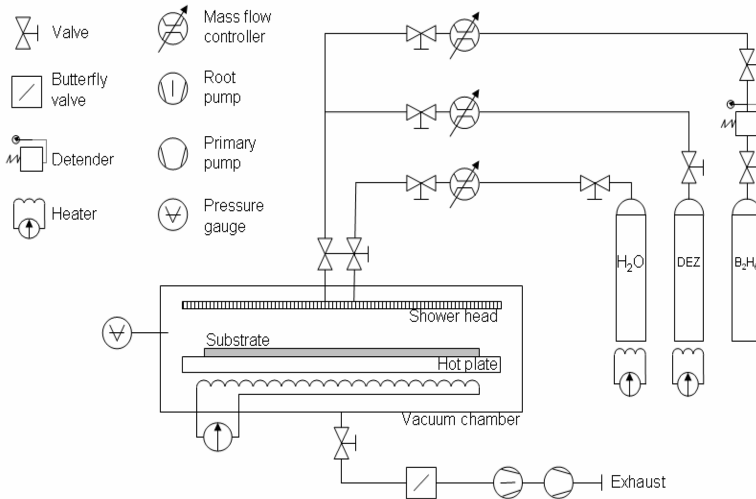

Figure 4.1 *Schematic drawing of the LPCVD ZnO:B system used at the IMT.*

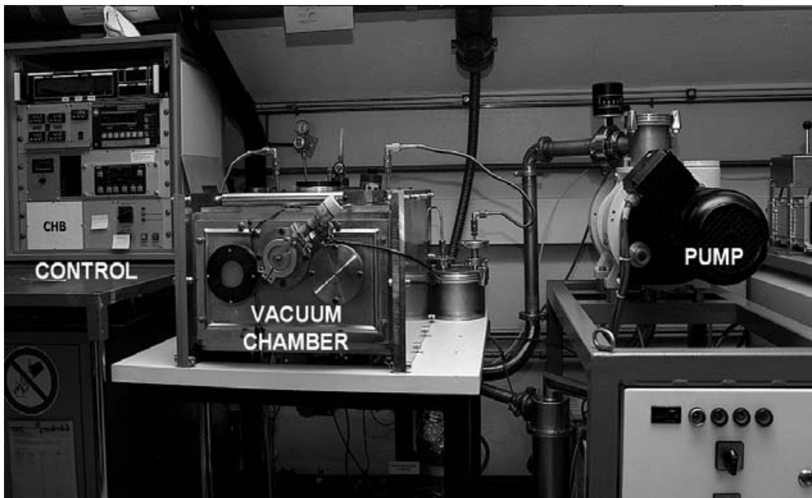

Figure 4.2 *Picture of the LPCVD ZnO:B system used at the IMT.*

The deposition area is a 30×30 cm temperature controlled hot plate. Temperature can be set from ambient to 300 °C.

We introduce the gases and vapors in the vacuum chamber through a shower cooled with ambient temperature water. The cooling is necessary in order to avoid deposition inside the showerhead.

We use vapors of liquid diethylzinc (DEZ) and water as precursors, directly evaporated in the reactor without any bubbler gas. The DEZ and the water vapor lines are heated at 35°C in order to avoid condensation. We use diborane gases 1 % diluted in argon as doping gases. Mass flow controllers control the flow of vapors and gases introduced in the vacuum chamber.

4.1.2 Chemical reactions

In the LPCVD ZnO deposition process, the deposition occurs as a result of chemical reactions of vapor phase precursors on an heated substrate. This section presents a review of the literature of the chemical reactions that may occur during the LPCVD ZnO:B layer fabrication [Smith 2003, Pierson 1999, Herold 1962].

Our chemical process uses diethylzinc (DEZ, $(C_2H_5)_2Zn$) and water vapor (H_2O) as precursors. Figure 4.3 presents the structure of the precursors. As the DEZ is a metal organic compound, the process is also called metal organic chemical vapor deposition (MOCVD).

The hydrolysis reaction that leads to the formation of ZnO from DEZ and water vapor during CVD is described via the equation :

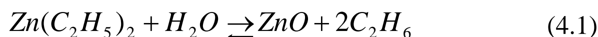

$$Zn(C_2H_5)_2 + H_2O \rightleftarrows ZnO + 2C_2H_6 \qquad (4.1)$$

This reaction occurs in at least two steps.

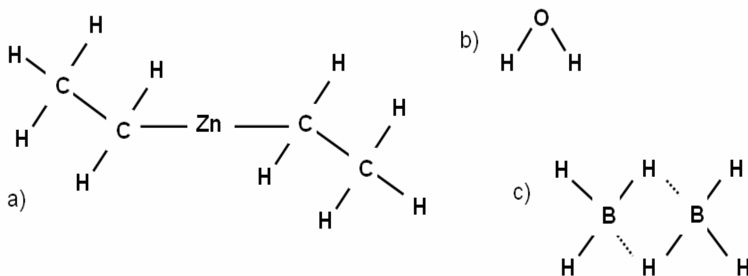

Figure 4.3 *The structure of the precursors used to growth LPCVD ZnO. a) Diethylzinc, b) Water, c) Diborane.*

The first step must consist of a partial hydrolysis of the DEZ leading to formation of ethylzinc hydroxide (C_2H_5ZnOH) :

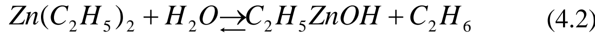

$$Zn(C_2H_5)_2 + H_2O \rightleftarrows C_2H_5ZnOH + C_2H_6 \qquad (4.2)$$

Further hydrolysis to $Zn(OH)_2$ is also possible :

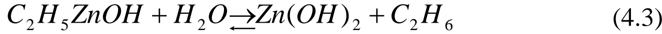

$$C_2H_5ZnOH + H_2O \rightleftarrows Zn(OH)_2 + C_2H_6 \qquad (4.3)$$

The $Zn(C_2H_5)OH$ and $Zn(OH)_2$ produced can also form dimmers, tetramers or higher oligomers.

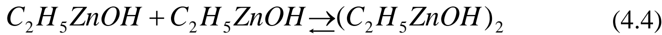

$$C_2H_5ZnOH + C_2H_5ZnOH \rightleftarrows (C_2H_5ZnOH)_2 \qquad (4.4)$$

$$(C_2H_5ZnOH)_2 + (C_2H_5ZnOH)_2 \rightleftarrows (C_2H_5ZnOH)_4 \qquad (4.5)$$

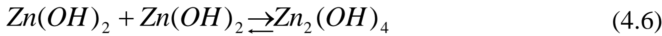

$$Zn(OH)_2 + Zn(OH)_2 \rightleftarrows Zn_2(OH)_4 \qquad (4.6)$$

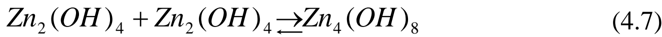

$$Zn_2(OH)_4 + Zn_2(OH)_4 \rightleftarrows Zn_4(OH)_8 \qquad (4.7)$$

Using products resulting from reactions described by equations 4.2 to 4.7, ZnO formation can occur through several reactions :

$$C_2H_5ZnOH \rightleftarrows ZnO + C_2H_6 \qquad (4.8)$$

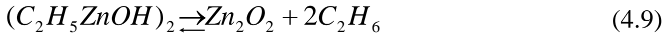

$$(C_2H_5ZnOH)_2 \rightleftarrows Zn_2O_2 + 2C_2H_6 \qquad (4.9)$$

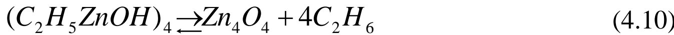

$$(C_2H_5ZnOH)_4 \rightleftarrows Zn_4O_4 + 4C_2H_6 \qquad (4.10)$$

$$Zn(OH)_2 \rightleftarrows ZnO + H_2O \qquad (4.11)$$

$$Zn_2(OH)_4 \rightleftarrows Zn_2O_2 + 2H_2O \qquad (4.12)$$

$$Zn_4(OH)_8 \rightleftarrows Zn_4O_4 + 4H_2O \qquad (4.13)$$

The formation of Zn_2O_2 and Zn_4O_4 is energetically unfavorable but may occur from larger oligomers.

Diborane reactions and incorporation in the ZnO crystal during the LPCVD process remain unclear. Basically, at rather low deposition temperatures, the diborane is decomposed and the ion B^{3+} is incorporated in the ZnO crystal. We know that B_2H_6 is highly reactive and may react with water or oxygen and carbon compounds [Pierson 1999]. Therefore, the boron atoms incorporated in the layer may not only be the B^{3+} ion but also boron compounds.

4.1.3 Review of the main deposition parameter effect

The structural, optical and electrical characteristics of LPCVD ZnO:B layers are sensitive to the deposition parameters. This makes the LPCVD ZnO:B process a very convenient tool for the optimization of TCO layers. Summarized below are the main parameters of the LPCVD process and their influences on the layer characteristics, based on the work of Faÿ and Selvan [Faÿ 2006, Faÿ 2005, Faÿ 2003, Faÿ 2000, Selvan 1998].

- ***Temperature***

Temperature is the most sensitive parameter in LPCVD ZnO deposition. It strongly influences the crystalline structure of the film and thus the surface roughness, the electrical and the optical parameters.

The deposition rate strongly depends on the temperature : between 130°C and 240°C, it increases with the increasing temperature. This indicates a growth almost partially reaction-rate limited.

LPCVD ZnO:B films are usually polycrystalline, having a wurtzite structure (see 4.2.1). The most commonly preferred crystallographic growth axis is with the c-axis (direction [0002]) perpendicular to the substrate. This corresponds to the closest packed plane (0002) parallel to the substrate. We observed this preferential orientation for ZnO deposited by sputtering as well as for LPCVD layers deposited below 150°C. This orientation gives a smooth film surface.

For LPCVD ZnO:B films grown at higher temperatures, the preferential crystallographic orientation is with the direction $[11\bar{2}0]$ perpendicular to the substrate (the planes $(11\bar{2}0)$ are parallel to the substrate), and a pyramidal textured growth surface is formed.

At deposition temperatures higher than 200°C, the enhanced surface diffusion of adatoms leads to random oriented small grain structure. Figure 4.4 shows a schematic drawing visualizing the crystal orientations and their corresponding film type.

LPCVD ZnO:B films show good transparency, independently of the temperature. The main optical characteristic that strongly changes is the diffuse transmittance (DT). In fact the DT is linked to the surface features (see 5.2). Films grown at low temperature are flat and the diffuse transmittance is low. For layers growth at a higher temperature, the DT becomes important due to the presence of a surface texture.

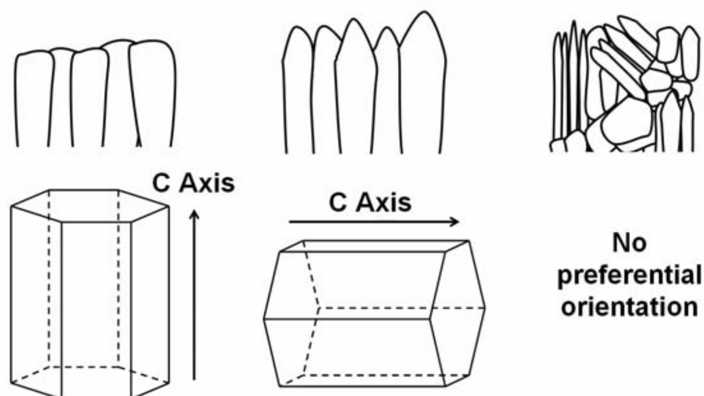

Figure 4.4 *The schematic drawing of the cross section of polycrystalline ZnO (top) and an illustration of their preferential growth orientation (bottom).*

Concerning the electrical characteristics, the resistivity shows a minimum of about 10^{-3} Ωcm around 150°C. Films deposited at higher or lower temperature exhibit a drastic decrease in electron mobility and carrier density leading to films with low conductivity. This optimum resistivity in regard to the deposition temperature value is strongly influenced by the total gas flow value.

- ***Pressure***

The deposition pressure mainly influences the deposition rate. At a deposition temperature of 172°C and gas flow value of [H_2O] = 60 sscm, [DEZ] = 50 sccm, [B_2H_6] = 30 sccm, the deposition rate increases from 60 to 130 Ås^{-1} by increasing the pressure from 0.5 to 5 mbar.

- ***Water vapor to DEZ gas flow ratio***

The water to DEZ gas flow ratio [H_2O]/[DEZ] influences the absorptance of the films. An excess of DEZ leads to films with low transparency, therefore the [H_2O]/[DEZ] is usually maintained at ~1.1.

- ***Diborane to DEZ gas flow ratio***

The diborane to DEZ gas flow ratio [B_2H_6]/[DEZ] controls the doping level. The carrier density, and thus the conductivity, is directly dependent on this parameter. A tradeoff has to be found between the electrical conductivity and the optical absorption induced by free carriers (see 5.2).

Table 4.1 summarizes the main influences of the deposition parameters on the layer characteristics.

4.1.4 Standard LPCVD ZnO:B layers deposition parameters and characteristics

Table 4.2 presents the deposition parameters as well as the properties of two types of LPCVD ZnO:B layers that constitute standard layers for the development of thin film silicon solar cells at IMT. The first type is designed to be integrated in aSi:H cells. The second type, developed within the framework of this study, is designed to be integrated in µcSi:H solar cells and is also used in micromorph cells.

These two layers are optimized to have a square resistance of 8-10 $\Omega_{\square}$. They are highly transparent, i.e. the total transmittance *TT* is superior to 80 % and the absorptance below 2 % in the wavelength region 450 - 600 nm.

The ZnO layer for aSi:H cells, originally developed by Faÿ [Faÿ 2003] is 2.2 µm thick and exhibits a haze value of about 38 %@600nm. The ZnO layer designed for µcSi:H cells is developed within the framework of this study. It needs a higher light trapping capability. To achieve this, we enlarge the surface features by increasing the thickness of the film up to 5 µm (see 5.2). Due to the higher thickness, we can lower the resistivity keeping a square resistance inferior to 10 $\Omega_{\square}$. As the carrier density of these films is low and the carrier mobility high, the film is highly transparent due to a low free carrier absorption (see 5.1.1).

Table 4.1 *The main influences of the LPCVD deposition parameters on the layer characteristics.*

Parameter	Symbol	Typical value	Range	Main influences on the layer characteristics
Deposition time	t_d	15'	1 – 60 '	Thickness
Pressure	P	0.3 mbar	0.1 – 1 mbar	Deposition rate
Temperature	*T*	175°C	25 – 300 °C	Surface texture, deposition rate, crystalline orientation
Total gas flow	[DEZ] + [H_2O] + [B_2H_6]	290 sccm	50-400 sccm	Deposition rate
Water to DEZ gas flow ratio	[H_2O]/[DEZ]	1.1	0.8 – 1.4	Transparency
Diborane to DEZ gas flow ratio	[B_2H_6]/[DEZ]	0.6	0 – 2	Conductivity, transparency

Table 4.2 *The deposition parameters and layer characteristics of LPCVD ZnO:B design for aSi:H cells and for μcSi:H cells.*

	LPCVD ZnO:B design for a-Si:H cell	LPCVD ZnO:B design for μc-Si:H cell
Deposition parameters		
T (°C)	178	178
P (mbar)	0.3	0.3
DEZ flow (sccm)	95	95
H_2O flow (sccm)	120	120
B_2H_6 flow (sccm)	78	17
$[H_2O]/[DEZ]$	1.1	1.1
$[B_2H_6]/[DEZ]$	0.6	0.3
Deposition time (min)	14	33
Layer properties		
Thickness d (μm)	2.2	5
Square resistance $R_\square$ ($\Omega_\square$)	8	10
Resistivity ρ ($\times 10^{-3}\Omega$cm)	1.7	5.2
Conductivity σ (Scm^{-1})	576	192
Hall mobility μ ($cm^2V^{-1}s^{-1}$)	30	40
Hall carrier density N ($\times 10^{20}$ cm^{-3})	1.2	0.35
Absorption coefficient (cm^{-1})	100@480nm	15@550nm
Transmittance@750nm (%) Measured in air, light coming from glass side	>80	>80
Haze@600nm (%)	38	84
Ref	[Faÿ 2003]	[Steinhauser 2005]

4.2 Structural and chemical properties of LPCVD ZnO:B films

4.2.1 Crystallographic orientation

Figure 4.5 shows the measured X-ray diffraction spectrum of an LPCVD ZnO:B layer designed for aSi:H cells (see 4.4 for the detailed deposition parameters) using the θ-2θ configuration (see 3.1.4). The spectrum shows a strong preferential crystallographic orientation, within the $(11\bar{2}0)$ plane parallel to the surface.

The peaks position observed for LPCVD ZnO:B concur with the literature for ZnO layers that crystallize in the hexagonal wurtzite (B4 type) structure and fit in the space group P63mc [ASTM 36-1451]. The preferential crystallographic growth axis is within the plane $(11\bar{2}0)$, parallel to the substrate. This preferential orientation is typical for ZnO film growth by LPCVD [Wenas 1991, Faÿ 2005] in the range of temperatures (i.e. 150 °C – 200 °C) that produce films with a rough surface, suitable for thin film solar cells applications.

Figure 4.6 shows a representation of the position of the atoms in the elementary cell for the hexagonal wurtzite structure of ZnO. The lattice parameters are a = 3.25 Å and c = 5.602 Å [Reeber 1970]. The structure is composed of two interpenetrating hexagonal close packed sublattices; zinc atoms are surrounded by four oxygen atoms that form a tetrahedral pyramid, and vice versa. This tetrahedral coordination corresponds to a sp3 covalent bond, but this material also has a strong ionic character [Jagadish 2006]. Due to the non-symmetry of the [0002] and $[000\bar{2}]$ directions, this structure shows two possible polarities along the c axis. Authors [Dong 2008, Jagadish 2006, Losurdo 2005, Segawa 1997, Sun 1994] report that the ZnO polarity influences many characteristics of the material such as thermal stability, impurity incorporation, doping efficiency, and gas adsorption and reactivity. For LPCVD ZnO:B layers deposited in this study, the polar faces are perpendicular to the substrate, therefore the polar facets may be located at grain boundaries.

4.2.2 Electron microscopy investigations

Figure 4.7 shows scanning electron micrographs (SEM) of the surface of the LPCVD ZnO:B sample optimized for aSi:H cells on glass (see 4.4). The sample thickness is d = 2.2 μm, and its root mean square surface roughness is about σ_{rms} = 60 nm.

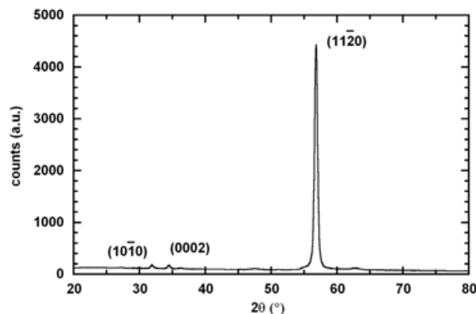

Figure 4.5 *The XRD diffraction spectrum of an LPCVD ZnO:B layer designed for a aSi:H cells measured in the θ-2θ configuration.*

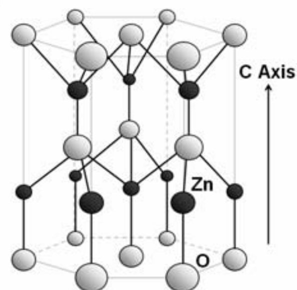

Figure 4.6 *The schematic drawing of the hexagonal wurtzite structure of ZnO.*

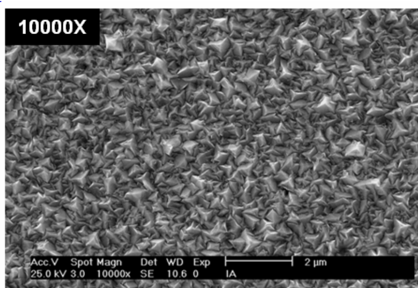

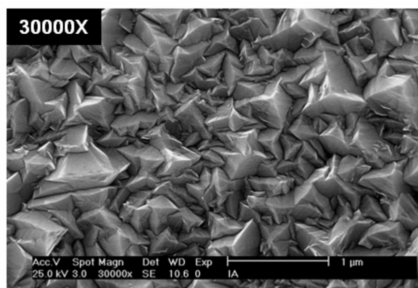

Figure 4.7 *Surface SEM micrographs of a LPCVD ZnO layer deposited on glass.*

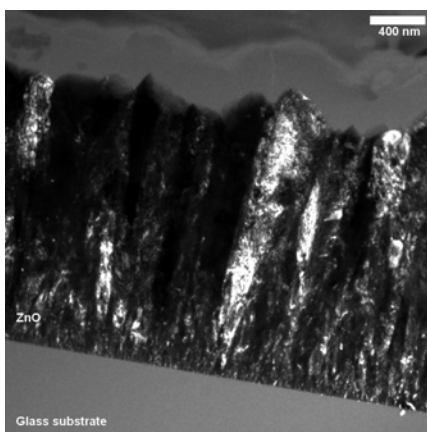

Figure 4.8 *TEM micrograph of a LPCVD ZnO deposited on a glass substrate.*

Two magnifications are presented : 10000× and 30000×. Pyramidal features appear randomly distributed at the surface. The lateral width of the pyramids is about 100 – 400 nm.

Figure 4.8 shows a transmission electron micrograph (TEM) of a similar ZnO:B sample. Preparation of the slice is performed by mechanical polishing. The first 300 nm of ZnO on the top of the glass substrate, i.e. the bottom of the ZnO layer, is composed of small crystallites. At greater thickness, the film is composed of vertically-stack monocrystalline grains that enlarge themselves as the film thickness increases. We can observe these large grains that appear at the surface as pyramids on the TEM micrograph in the upper part of the layer and on the SEM micrographs. The structure and the growing mechanisms of LPCVD ZnO:B layers have been extensively described by Faÿ [Faÿ 2005, Faÿ 2003, Faÿ 2000].

The first 300 nm of the layer is composed of small grains with no preferential orientation and has poor electrical conductivity. The larger crystallites compete the smaller ones, leading to a columnar growth of vertically-stack grains with good electrical conductivity. These grains appear at the surface as pyramids. Further increases in the thickness lead to larger grain size and larger surface features.

4.2.3 Chemical properties

In this section we discuss the chemical composition of LPCVD ZnO:B layers analyzed in the framework of this study using various characterization tools.

Experimental results

Figure 4.9 presents an energy-dispersive X-ray spectroscopy (EDX, see 3.1.2) spectrum acquired by a ESEM on a LPCVD ZnO:B film designed for aSi:H cells (see 4.4). Lines of zinc and oxygen are present. EDX technique cannot detect boron. Other elements are below the detection limits (~1% at.).

Figure 4.10 shows the depth profile of the atomic concentration of Zn and O measured by Rutherford backscattering spectroscopy RBS (see 3.1.5). The measured sample is similar to LPCVD ZnO:B samples optimized for aSi:H cells except at a reduced thickness of 1080 nm. Boron and other possible elements are not detected using RBS measurements. This analysis reveals a constant ratio over the whole film thickness between the Zn and O equal to 53.7 % at Zn and 46.3 % at O.

Figure 4.11 shows the Secondary ion mass spectroscopy (SIMS, see 3.1.6) depth profile of a 1.5 μm thick sample similar to LPCVD ZnO:B samples optimized for aSi:H cells. We analyse the B, Fe, H, C, O, Cu and Si depth

profile. We do not carry out quantification due to the lack of standards in ZnO. Therefore, we leave the profile as raw secondary ion counts. As quantification is not possible, we discuss the results qualitatively.

Discussion

The results of the RBS analysis clearly prove and quantify the non-stochiometry of as grown LPCVD ZnO:B. The ratio between the measured atomic percentage is Zn/O = 1.094. This value is surprisingly high, and can be induce by the imprecision of the RBS measurement (~1 %). However, a close value measured by energy dispersive X-ray spectroscopy on sputtered ZnO : Zn/O = 1.09 have been reported [Bensmaine 2007].

Authors [Ellmer 2007, Jagadish 2006, Nickel 2004, Tomlins 2000. Look 1999] related the excess of zinc with the n type doping character of intrinsic zinc oxide. The exact doping mechanisms are still hardly discussed, but it is generally admitted that Zn interstitial and oxygen vacancies act as electron donors in ZnO. If we consider an atomic density of $4.19\ 10^{22}$ cm^{-3} [Ellmer 2007] and that only the doubly charge zinc interstitials (or oxygen vacancies) contribute to the excess of electrons, we find a carrier density of $3.7\ 10^{21}$ cm^{-3}, which is about 100 times higher than electron density measured by hall measurement on intrinsic LPCVD ZnO films. One hypothesis to explain this difference could be self-compensating p doping from acceptor centers such as zinc vacancies or nitrogen on oxygen sites [Ellmer 2007, Jagadish 2006, Nickel 2004].

SIMS analysis shows the incorporation of boron. These measurements also indicate the presence of hydrogen and carbon in the film. Hydrogen and carbon could be incorporate during the deposition through the decomposition of diethylzinc and diborane. Moreover, Zn and B can be incorporated in their atomic form but also as compounds bound with oxygen, hydrogen or carbon.

Recently, authors found that hydrogen can act as a shallow donor in ZnO [Bang 2008,Van de Walle 2000]. This fact, in addition to the non-stoechiometry of the film, explain the strong n type doping character of our intrinsic layer.

As the structure of the film is polycrystalline, we suspect that compound containing hydrogen and carbon could precipitate at the grain boundaries [Domingos 2004, Fionova 1993].

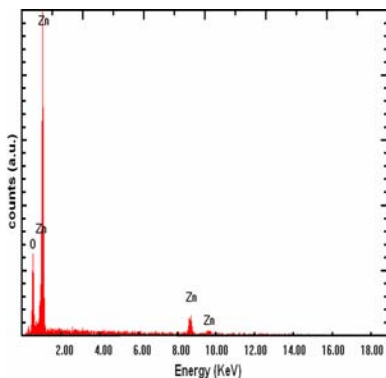

Figure 4.9 *The EDX spectrum of an LPCVD ZnO:B designed for aSi:H cells deposited on a glass substrate.*

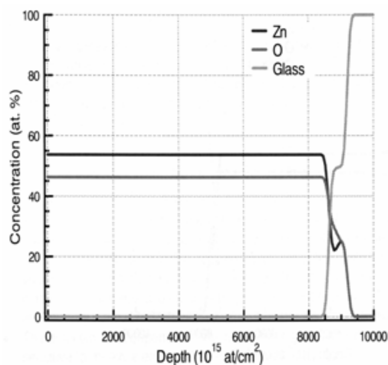

Figure 4.10 *The depth profile of the atomic concentration measured by RBS of an LPCVD ZnO:B designed for aSi:H cells deposited on a glass substrate.*

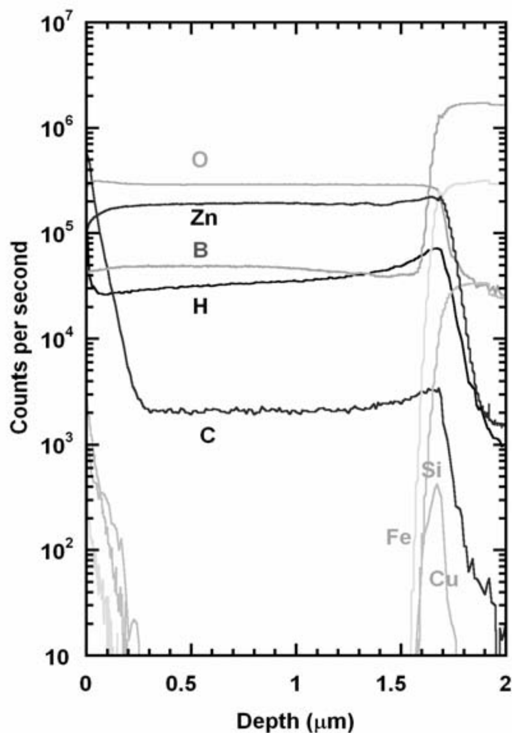

Figure 4.11 *The depth profile of raw secondary ion counts of various elements measured by SIMS of an LPCVD ZnO:B designed for aSi:H cells deposited on a glass substrate.*

4.3 Conclusions

We show that the LPCVD ZnO:B deposition process is a very flexible and convenient tool to achieved films with various characteristics. In fact, varying the process parameters, easily change the properties of the deposited films.

We show that LPCVD ZnO:B layers have an hexagonal wurtzite structure oriented within the $(11\bar{2}0)$ plane parallel to the surface. The films are polycrystalline, composed of large columnar monocrystalline grains. This columnar structure leads to surface pyramidal shape features. We observe the presence of an incubation layer of about 300 nm made of small crystallite.

Finally, chemical analysis on LPCVD ZnO:B layers provides evidence of its non stoechiometry as well as the presence of carbon and hydrogen in the layers.

CHAPTER 5 *Optical properties of LPCVD ZnO:B films*

Understanding the mechanisms that govern the transparency of LPCVD ZnO:B layers in the visible and near infrared (NIR) range is crucial in order to get films suitable as TCO for thin film solar cells. Moreover, analyzing the optical behavior at other wavelengths such as the ultra-violet (UV) or infrared regions (IR) gives important knowledge about the material properties.

In this chapter, we analyze the optical properties of LPCVD ZnO:B layers. We describe the transmittance, reflectance and absorptance of LPCVD ZnO:B films for a broad range of wavelengths extending from the UV to the IR. We analyze the band gap absorption, the infrared free carrier absorption and the reflection as a function of the doping level of the layer. We study the light scattering capability resulting from the as grown rough surface of the ZnO films. Finally, we present Raman analyses of LPCVD ZnO:B with different doping levels.

5.1 Transmission and reflection studies

5.1.1 Overview

This section presents transmittance, reflectance, absorptance spectra and ellipsometry results of typical LPCVD ZnO:B films in the wavelength range from 0.2 μm to 3μm.

Experimental results
The following measurements are performed on LPCVD ZnO:B layers designed for aSi:H cells deposited with the parameters given in chapter 4, table 4.2. The samples are deposited on glass, the thickness d of the films is about 2 μm and the carrier density N is around 1 10^{20} cm^{-3}.

Figure 5.1 shows the transmittance (*TT*) and the reflectance (*TR*) measured with a UV-visible photospectrometer (see 3.2.1) in the visible range and with an FTIR spectrometer (see 3.2.2) in the near infrared region.

Figure 5.2 shows the absorptance (*A*) deduced from the transmittance and reflectance using the equation :

$$A = 1 - TT - TR \qquad (5.1)$$

For the deduction of *A*, we measure *TT* and *TR* with diiodomethane (CH_2I_2) as index matching liquid in order to avoid internal reflections (see 3.2.1).

Figure 5.3 shows the optical constants *n* and *k* extracted from ellipsometry spectroscopy (see 3.2.4) measurements performed on a LPCVD ZnO:B layers for aSi:H cells. The dielectric function used to model this ZnO layer is a sum of two Lorentzien oscillators and a Drude oscillator (see 2.2.2). The roughness of the films is modeled with an additional layer considering the dielectric characteristics of air and ZnO. In the visible range, the refractive index is about $n \sim 1.9$ and the extinction coefficient $k < 0.2$.

Specialists from Prague University (Institute of physics, Academy of Sciences of the Czech Republic) measured the absorption coefficients by photothermal deflection spectroscopy [Jackson 1982] after polishing the samples.

Figure 5.4 shows the absorption coefficients for LPCVD ZnO:B designed for aSi:H and for μcSi:H cells. Chapter 4, table 4.2 gives the deposition parameters and the layer's properties of the analyzed samples. The first sample, (LPCVD ZnO:B layer designed for aSi:H cell) absorbs about 2 % of the incoming light in the spectral region 430-580 nm. The second sample (LPCVD ZnO:B layer for μSi:H cells) absorbs only 0.7 % of the incoming light in the region 480-650 nm despite its greater thickness. The minimum absorption coefficients listed table 5.1, are respectively 100 cm^{-1} at 480 nm and 15 cm^{-1} at 550 nm for the first and the second samples.

Discussion

Above an incident radiation energy of about 3.3 eV (wavelengths below λ = 375 nm), the extinction coefficient *k* of LPCVD ZnO:B sample strongly increases. This increasing *k* value is related to the fundamental band gap absorption, which is due to interband transition, i.e. formation of electron-hole pairs (see 2.1.1). We discuss details and models about these mechanisms in section 5.1.2.

In the visible region (i.e. photon energy between 1.4 eV and 3 eV), transmission is limited only by reflection losses and by the low absorptance $A > 2\%$. This can be caused by both residual absorption due to free carriers and defect-related absorption. These two absorption mechanisms are discussed here after.

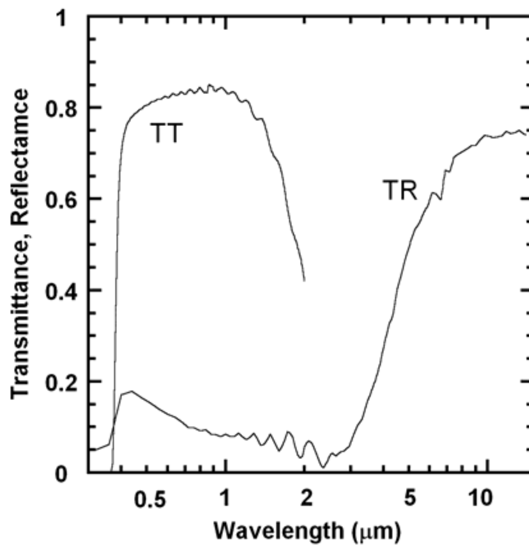

Figure 5.1 *The transmittance (TT) and the reflectance (TR) spectra of a LPCVD ZnO:B layer for aSi:H cell as a function of the wavelength.*

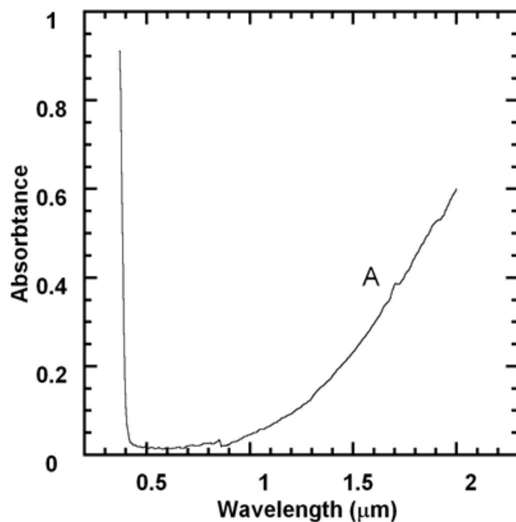

Figure 5.2 *The absorptance (A) of a LPCVD ZnO:B layer for aSi:H cell as a function of the wavelength.*

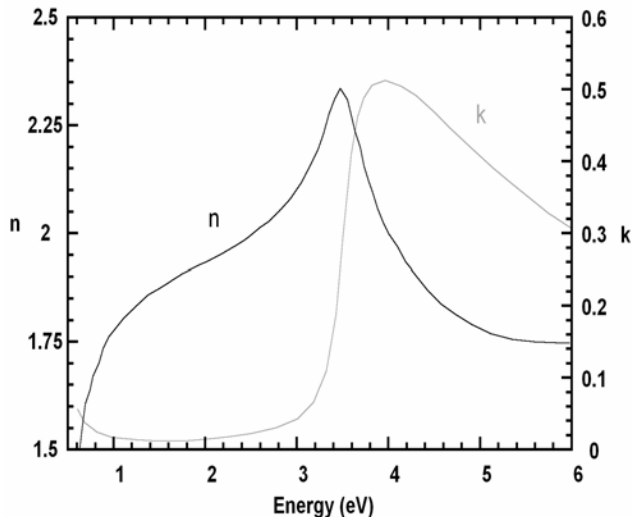

Figure 5.3 *The optical constants n and k extracted from a fit of an ellipsometry spectroscopy measurement of a LPCVD ZnO:B layer for aSi:H cell.*

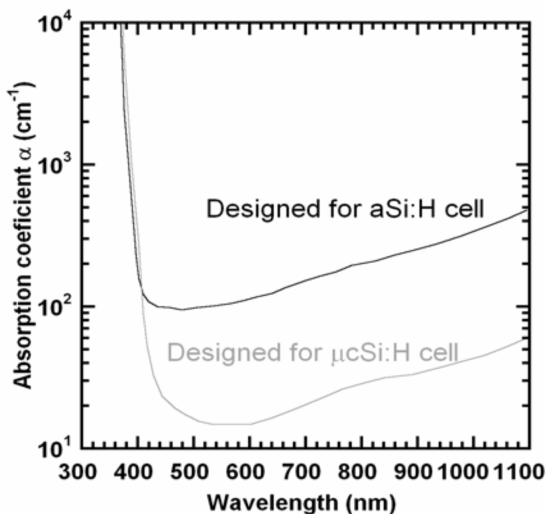

Figure 5.4 *The experimental absorption coefficient α deduced from photothermal spectroscopy measurement.of a LPCVD ZnO:B layer for aSi:H cell and LPCVD ZnO:B for μSi:H cell.*

Table 5.1 *The experimental and calculated absorption coefficient α of a LPCVD ZnO:B layer for aSi:H cell and LPCVD ZnO:B for μSi:H cell. The measured absorption coefficient $\alpha_{experimental}$ is deduced from photothermal spectroscopy measurement. The calculated absorption coefficient α_{theory} is extracted from equation 5.2 with $m = 0.28m_0$, $\mu = 100$ $cm^2V^{-1}s^{-1}$, and $n = 1.9$.*

	Thickness after polishing (μm)	Hall carrier density ($\times 10^{20}$ cm^{-3})	**Experimental absorption coefficient $\alpha_{experimental}$ (cm^{-1})**	**Calculated absorption coefficient α_{theory} from equation 5.1 (cm^{-1})**
LPCVD ZnO:B for aSi:H cell	2.1	1.2	**130 @650nm**	**179 @650nm**
LPCVD ZnO:B for μcSi:H cell	4.2	0.3	**18 @650nm**	**45 @650nm**

- The free carrier absorption coefficient α follows the relationship [Chopra 1983] :

$$\alpha = \frac{\lambda^2 e^3 N}{4\pi^2 \varepsilon_0 c^3 n m^2 \mu} \quad (5.2)$$

where N is the free carrier concentration, μ their mobility, n the refractive index, m their effective mass, ε_0 the permittivity of free space, c the light velocity, and λ the wavelength. It should be noted that the free carrier absorption is an increasing linear function of the carrier density, and is inversely proportional to the mobility. It increases with the square of the wavelength.

Table 5.1 gives the measured and calculated absorption coefficient for LPCVD ZnO:B samples designed for aSi:H and μcSi:H cells. The calculated absorption coefficients α_{theory} are deduced from equation 5.2 using the carrier density N evaluated from Hall measurements, the mobility μ = 100 $cm^2V^{-1}s^{-1}$ is typical for monocrystalline ZnO [Gordon 2000, Ellmer 2001], $m = 0.28m_0$, and $n = 1.9$.

The values of α_{theory} and $\alpha_{experimental}$ are close. The slight difference between these two values can be due to the measurement uncertainty and to the uncertainty of the value of μ and N taken for the calculation. This indicates that for these LPCVD ZnO:B samples, the residual FCA is the main factor governing the absorption in the visible range. Therefore, following equation 5.2, a decrease in the carrier concentration or an increase in the

mobility can further reduce the absorption coefficient in the visible wavelength range.

♦ Selvan [Selvan 1998] mentioned that LPCVD ZnO:B films can exhibit defect absorption resulting in a slight yellow coloration of the films. This absorption is due to an optical assisted charge transfer of an electron from the valence band to a deep donor like level located in the forbidden band. These deep levels could be related to interstitial zinc atoms or clusters forming a donor like species. This absorption was observed for layers grown with a gas phase ratio $[H_2O]/[DEZ] < 1$. For films grown with a $[H_2O]/[DEZ] > 1$, such as the ones presented here, the absorption resulting from this phenomenon is negligible.

In the IR region, strong absorption and reflection occur. We discuss this infrared optical response of LPCVD ZnO:B layers in Section 5.1.3.

The oscillations present in both reflection and transmission spectra are due to constructive and destructive interferences resulting from multiple reflections inside the thin ZnO layer [Hecht 1987]. Because the samples are rough, the interference amplitudes are attenuated compared to the theoretically calculated ones for layers with flat interfaces. We can explain this phenomenum by a loss in the coherence of light due to the surface roughness [Beckmann 1963].

Conclusions
Band gap absorption at low wavelength, transparency in the visible range, and free carriers absorption and reflection in the infrared region constitute the typical optical behavior that is observed for LPCVD ZnO:B samples.

We attributed the slight absorption of LPCVD ZnO:B that remains in the visible range to residual free carrier absorption.

5.1.2 Band gap absorption

This section discusses the fundamental band edge of LPCVD ZnO:B layers and its variation with the doping level.

Experimental results
2 µm thick LPCVD ZnO:B layers are deposited on glass with a gas phase doping ratio $[B_2H_6]/[DEZ]$ varying from 0 to 2, leading to free carrier density N increasing from $1.9\ 10^{19}\ cm^{-3}$ to $2.2\ 10^{20}\ cm^{-3}$ respectively.

We measure the total transmittances of these samples by UV spectroscopy (see 3.3). Figure 5.5 shows the near band gap transmittance as a function of the wavelength for all the series of samples. We observed a shift of the transmittance edge to a higher energy as the doping level increases.

In the range from 300 nm to 420 nm, we evaluate the optical absorption coefficient α from the measured transmittance TT value using [Pankove 1975] :

$$\alpha = \frac{1}{d} \ln\left(\frac{1}{T}\right) \qquad (5.3)$$

where d is the film thickness.

In a direct band gap material, such as ZnO, we can express the dependence of α as a function of the photon energy ($h\nu$) as [Pankove 1975]:

$$\alpha = A\sqrt{(h\nu - E_g)} \qquad (5.4)$$

where A is a constant, and E_g the optical band gap energy.

We calculate the absorption coefficient α for all the samples from equation 5.3. Figure 5.6 shows a plot of α^2 as a function of $h\nu$ for ZnO layers with various boron doping levels. Following equation 5.4, we obtain the band gap energy E_g by extrapolating the linear part of the curve α^2 versus the photon energy to $\alpha^2 = 0$. The E_g values obtained for the series of samples are increasing with the doping level from 3.24 eV for the undoped sample to 3.44 eV for the heavily doped one.

Discussion

We can partly explain the widening of the band gap with the increase of the carrier density by the filling of the lowest states in the conduction band. This effect is known as the Burnstein-Moss (BM) shift [Burnstein 1954], which predicts a band gap widening that follows the equation:

$$\Delta E_{BM} = \frac{h^2 N^{2/3}}{8m\left(\frac{\pi}{3}\right)^{2/3}} \qquad (5.5)$$

where h is Planck’s constant, N is the free carrier density and m is the effective mass.

A second phenomenon that affects the optical absorption edge with the increasing carrier density is a band-gap-narrowing (BGN) effect due to electron-electron repulsive interactions and screening of the potential due to the presence of many electrons.

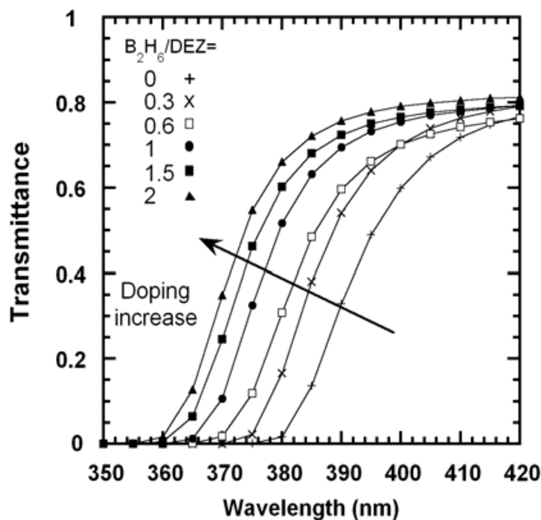

Figure 5.5 *The near band gap total transmittance for 2 μm thick LPVCVD ZnO:B films, for which the gas phase doping ratio [B_2H_6]/[DEZ] used during the deposition was varied from 0 (undoped) to 2 (higly doped).*

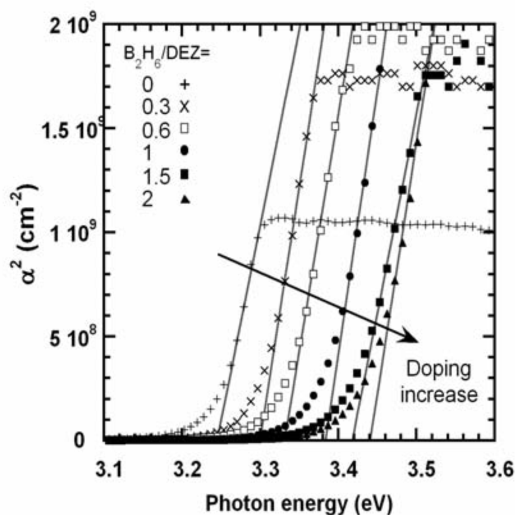

Figure 5.6 *The square of the absorption coefficient α as a function of incident photon energy $h\nu$ for LPCVD:B ZnO films grown with gas phase doping ratio [B_2H_6]/[DEZ] varying from 0 to 2. Full lines are fits to equation 5.3 and their intercept with abscissa gives the value for the optical band gap Eg.*

This effect is described by several authors [Roth 1982, Sernelius 1988, Jin 1988] that found a gap shrinkage in heavily doped ZnO (ΔE_{BGN}) proportional to $N^{1/3}$. Therefore, ΔE_{BGN} as a function of N is written:

$$\Delta E_{BGN} = CN^{1/3} \quad (5.6)$$

where C is a constant.

The expression for the band gap energy is then written:

$$Eg = E_0 + \Delta E_{BM} - \Delta E_{BGN} \qquad (5.7)$$

where E_0 is the theoretical intrinsic band gap.

Figure 5.7 shows experimental values of E_g (see figure 5.6) plotted versus N. The dashed line is the theoretical prediction of the band gap widening following only the Burstein-Moss shift law. The BM widening is calculated from equation 5.5 with $E_0 = 3.3$eV (band gap of the ZnO single crystal [Ellmer 2007]) and $m = 0.28m_e$. The experimental values of E_g strongly differ from the theoretical ones. This indicates that the Burnstein-Moss shift effect alone is not well suited to explain the band gap shift in LPCVD ZnO:B. The solid line represents the predicted variations of E_g taking into account both BM and BGN effects. These correspond well with the experimental values by setting $C = 5.4\ 10^{-8}$ eVcm in equation 5.6, in agreement with Roth et al. [Roth 1982], who obtained a constant $C = 3.6\ 10^{-8}$ eVcm foor ZnO samples prepared by sputtering and MOCVD. Therefore, it demonstrates that the degeneracy of LPCVD ZnO induce non-negligible band gap narrowing effects.

In the energy range slightly lower than the band gap, the absorption coefficient α follows an exponential law expressed by:

$$\alpha = \alpha_0 e^{\left(\frac{h\nu}{E_e}\right)} \qquad (5.8)$$

where α_0 is a constant, E_e an energy which is interpreted by authors [Urbach 1953, Natsume 2000] as an the exponentially decreasing tail of states in the band gap.

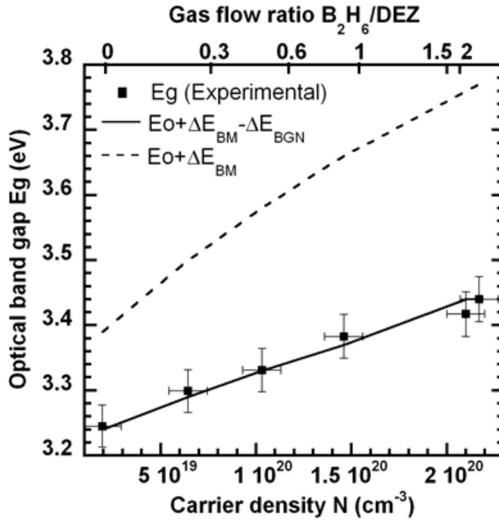

Figure 5.7 *The optical band gap energy Eg as a function of the carrier density N. The lines are theoretical predictions. The dashed lines take into account the Burnstein-Moss law alone. The solid line takes into account both Burnstein-Moss and band gap narrowing effects (equation 5.7). For these calculations we take* $E_0 = 3.3$ *eV,* $m = 0.28m_0$.

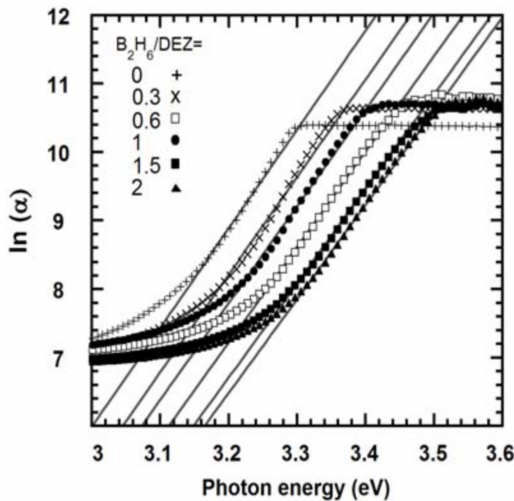

Figure 5.8 *The logarithm of the absorption coefficient* $ln(\alpha)$ *as a function of incident photon energy* $h\nu$ *for ZnO films grown with gas phase doping ratio* $[B_2H_6]/[DEZ]$ *varying from 0 to 2. Full lines are fits to equation 5.7 for E > Eg and assuming* $\alpha_0 = 5.61\ 10^{-17}\ cm^{-1}$. *The slopes of the fitted curves give the value of* $1/E_e$.

Table 5.2 *The band gap energy E_g and the parameter E_e for 2 μm-thick ZnO films grown with gas phase doping ratio $[B_2H_6]/[DEZ]$ varying from 0 to 2.*

Gas flow ratio B_2H_6/DEZ	Hall carrier density ($\times 10^{20}$ cm^{-3})	Band gap energy E_g (eV)	E_e (meV)
0	0.2	3.25	69.1
0.3	0.6	3.30	70.1
0.6	1	3.33	70.8
1	1.5	3.38	71.7
1.5	2.1	3.42	72.5
2	2.2	3.44	72.9

Figure 5.8 shows the fits of the experimental absorption coefficient with equation 5.8 for the doping series of LPCVD ZnO:B. They are obtained for $E < Eg$. We list the obtained values of E_e in table 5.2, $\alpha_0 = 5.61\ 10^{17}$cm^{-1}. E_e increases with the doping level of the ZnO:B samples from 69.1 meV for the undoped sample to 72.9 meV for the heavily doped one.

We can relate this slight increase of E_e with the increasing doping level to an increase of the number of states in the band gap induced by the increasing numbers of incorporate boron atoms. This conclusion is in agreement with interpretation of similar behavior reported by [Aghamalyan 2003] on sputtered ZnO:Ga.

The laser beam energy used for scribing silicon solar cells (355 nm, i.e. 3.49 eV) is close to the optical band gap energy of LPCVD ZnO:B layers. Therefore, our results show that the ZnO doping level absorption dependence has to be taken into account when performing the optimization of the laser scribing process for TCO.

Conclusions

In conclusion, the direct optical band gap edge of LPCVD ZnO:B occurs in the UV range around 3.3eV. The value of E_g is shifted toward larger energies as carrier density increases following the Burstein-Moss plus band gap narrowing effects. At an energy level slightly lower than E_g, we observe exponential band tail absorption due to states in the band gap.

5.1.3 Infrared response

In the near infrared region, the free carrier absorption and reflection describe with the Drude model dominate the optical properties of LPCVD ZnO:B layers (see 2.2.2). This section analyzes the IR response of LPCVD ZnO:B layers with various doping levels.

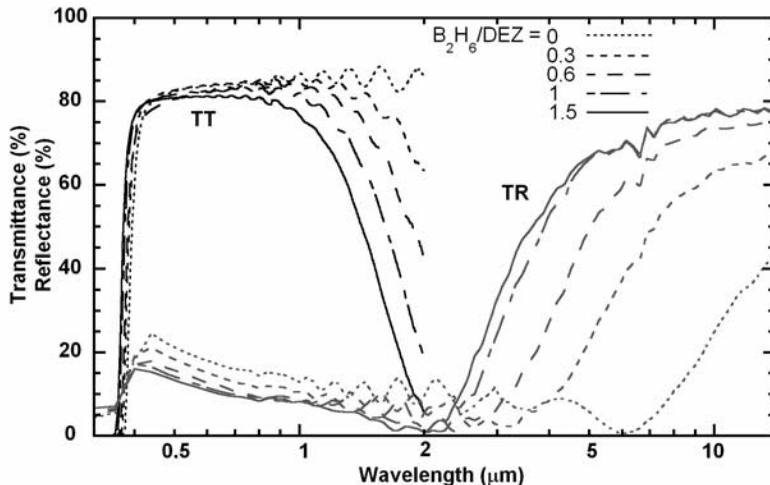

Figure 5.9 *The total transmittance TT and reflectance TR for 2-μm thick ZnO films, for which the gas phase doping ratio [B_2H_6]/[DEZ] used during the deposition was varied from 0 (undoped) to 1.5 (higly doped).*

Experimental results

We study the same series of LPCVD ZnO:B layers as in paragraph 5.1.2 (2 μm thick ZnO layers grown on glass with gas phase doping ratio varying from 0 to 2).

We evaluate the visible transmittance and reflectance of the series of samples with a UV-visible photospectrometer (see 3.2.1). We measure the total reflectance in the near infrared and infrared range with a FTIR spectrometer (see 3.2.2).

Figure 5.9 shows the measured reflectance *TR* and transmittance *TT* spectra as a function of the wavelength. These films have an average transmittance TT > 80% and the absorbance $A = 1\text{-}TT\text{-}TR < 3$ % in the visible range (wavelength between 0.4 to 1 μm). In the near infrared region (wavelength between 1 and 2 μm), *TT* decreases. The inflexion point is shifted towards shorter wavelengths with increasing doping ratios, due to the related increase of free carrier absorption (FCA). At longer wavelengths, *TR* abruptly increases after the so-called plasma resonance wavelength. The plasma wavelength is progressively lowered as the boron content and consequently the free carrier density is increased.

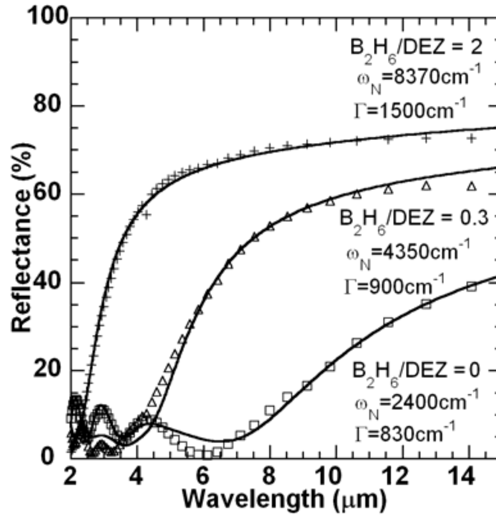

Figure 5.10 *Examples of fits using the Drude model (solid lines) of near normal reflectance spectra of ZnO films (symbol) deposited with different gas phase doping ratio [B_2H_6]/[DEZ] .*

Discussion

At a distance from the band gap, the optical behavior of the films can be described using the classical Drude model detailed in chapter 2 (see 2.1.3) [Hamberg 1986, Jin 1988, Aghamalyan 2003]. The corresponding dielectric function ε is expressed as :

$$\varepsilon(\omega) = \varepsilon_\infty - \frac{{\omega_N}^2}{\omega^2 + i\Gamma\omega} \qquad (5.9)$$

where ε_∞ is the high frequency dielectric function, Γ is a damping frequency and

$${\omega_N}^2 = \frac{N_{optic} e^2}{\varepsilon_0 m} \qquad (5.10)$$

where N_{optic} is the free electron density, e the electron charge, ε_0 the permittivity of free space and m the electron effective mass.

Assuming $\varepsilon_\infty = 4$ and $m = 0.28m_e$ where m_e is electron mass [Jin 1988, Qiao 2006], the reflectance spectra of ZnO films could be fitted with this model taking into account the glass substrate and using ω_N and Γ as fitting factors.

Example of fits for ZnO layers with different doping ratios are given in figure 5.10. We obtain a good convergence of the fitted curves with the experimental data in the range of validity of the Drude model. We will discuss in chapter 6 the relation between the optical parameters and the electrical properties of the films.

Conclusions

The Drude model in its simplest form is sufficient to describe the NIR optical behavior of LPCVD ZnO:B films.

5.2 Light scattering capabilities

For thin film solar cell applications, one of the most important characteristics for a front contact TCO is its capability to scatter the light in order to increase the optical path through the solar cell. The LPCVD ZnO:B layer has the advantage to possess an as grown roughness leading to surface texture with efficient light scattering capability without any post treatment. This paragraph studies this light scattering behavior in detail.

Experimental results

A series of five LPCVD ZnO:B layers with thicknesses of 1.4 μm, 1.9 μm, 2.4 μm, 4.0 μm, and 6.3 μm respectively are deposited on glass substrates. We obtain the different thicknesses by changing the deposition time. We adapt the gas phase doping ratio [B_2H_6]/[DEZ] used during ZnO deposition for each sample in order to obtain layers with the same sheet resistance of 10 $\Omega_\square$. We vary the [B_2H_6]/[DEZ] from 0 (thick undoped ZnO) to 2 (thin heavily doped ZnO). In order to simplify their denomination we label the samples with their thickness values.

We determine the root mean square values of the surface roughness σ_{rms} by Atomic Force Microscopy (AFM) measurements (see 3.1.3). Figure 5.11 shows 3D interpretations of the AFM pictures for the 1.4 μm, 1.9 μm, 2.4 μm, and 6.3 μm samples. Their respective deduced RMS roughness values are : 60 nm, 86 nm, 109 nm, 226 nm.

We measure the total and diffuse optical transmittance (*TT* and *DT*, respectively) for each sample in air with a photospectrometer (see 3.2.1). Figure 5.12 shows the *TT* and *DT* spectra of the five samples. In the NIR range, the *TT* increases with the increasing thickness of the samples. In the visible range, the *TT* decreases and the *DT* increases with the increasing thickness of the samples.

Figure 5.13 shows the absorptance of the series of samples as a function of the wavelength. Despite the increasing thickness of the layers, the A value is progressively lowered as the doping level decreases and thus the FCA.

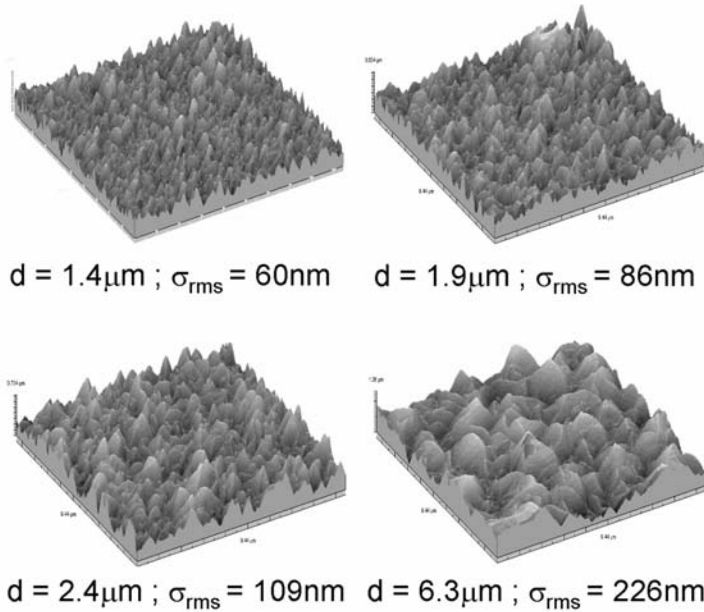

Figure 5.11 *3D atomic force microscopy (AFM) pictures for ZnO layers for which thickness was varied from 1.4 to 6.3 μm implying a surface roughness rms varying from 60 to 226 nm.*

The haze factor is defined by the ratio between the diffuse transmittance *DT* to the total transmittance *TT* :

$$H(\lambda) = \frac{DT(\lambda)}{TT(\lambda)} \qquad (5.11)$$

Figure 5.14 shows the deduced haze factor *H* for each sample of the series as a function of the wavelength. The haze factors strongly increase in the visible range with the increasing thickness of the ZnO:B samples.

Figure 5.15 shows a normalized angular distribution function (see 3.2.3) measured for the thinner and thicker sample. We choose the normalization factors for each sample in order to equalize the maximum values of the absolute intensities. In the thinner sample the ratio between intensity of light scattered at large angles (scattering angle > 60°) and intensity of light scattered at small angle (scattering angle < 60°) is higher compared to the thicker sample, which diffuses light closer to the specular direction.

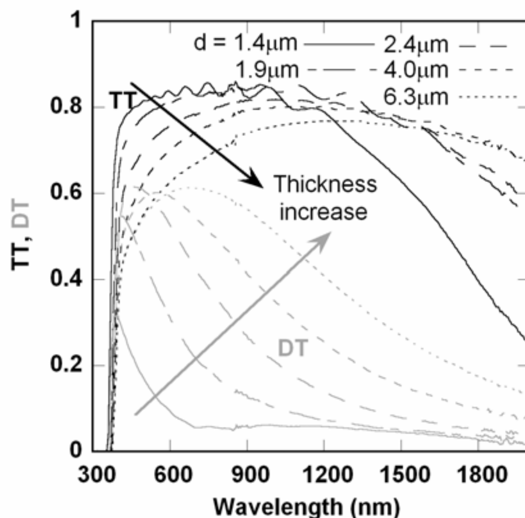

Figure 5.12 *Total and diffuse transmittance as a function of the wavelength for ZnO layers for which thickness was varied from 1.4 to 6.3μm inducing a surface roughness σ_{RMS} varying from 60 to 226 nm.(measured without index matching liquid).*

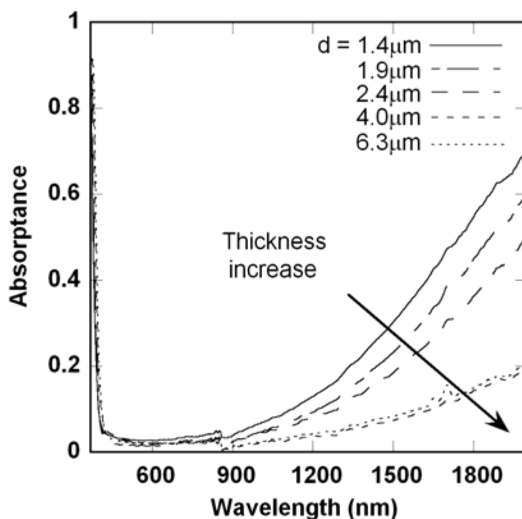

Figure 5.13 *Haze factor as a function of the wavelength for ZnO layers for which thickness was varied from 1.4 to 6.3μm inducing a surface roughness σ_{RMS} varying from 60 to 226 nm (measured with index matching liquid).*

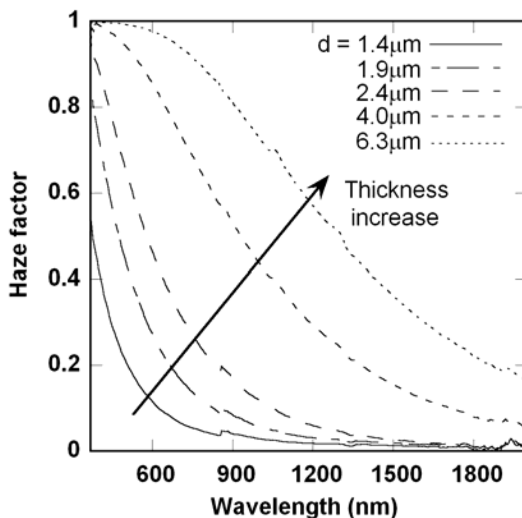

Figure 5.14 *Haze factor as a function of the wavelength for ZnO layers for which thickness was varied from 1.4 to 6.3μm inducing a surface roughness σ_{RMS} varying from 60 to 226 nm.*

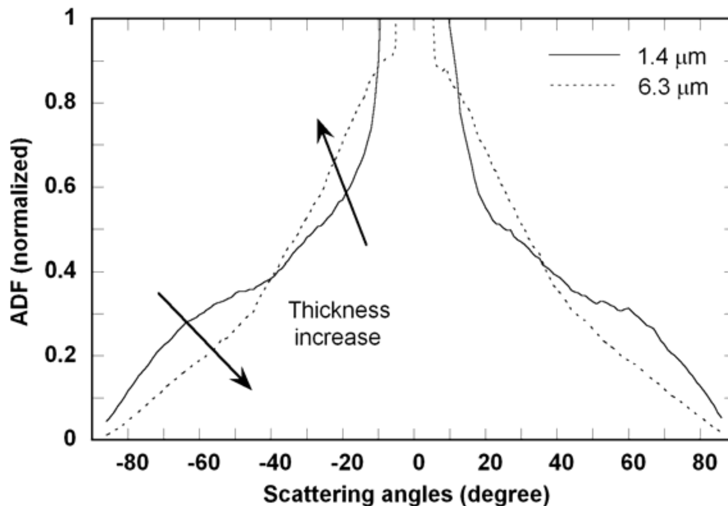

Figure 5.15 *Normalized* (*the normalisation factors for each sample are chosen in order to equalize the maximum values of the absolute intensities) angular distribution function of two ZnO layers : one sample 6.3μm thick with large surface features, and one sample 1.4μm with small surface features.*

Discussion

The light scattering capability of the layers is induced by their roughness. In first approximation, we can describe this phenomenon with the scalar scattering theory [Beckmann 1963]. This model assumes a diffuse transmittance DT given by :

$$DT = 1 - e^{-\left(\frac{4\pi\sigma_{rms}(n_0 - n_1)}{\lambda}\right)^2} \quad (5.12)$$

where, n_0 and n_1 are the refractive index of the two interface media e.g. air and ZnO, σ_{rms} is the RMS roughness of the interface and λ the wavelength of the incident light. Note that the exponential factor shows a λ^{-2} dependence.

We can fit the *DT* spectrum of the 6.3 μm ZnO sample (i.e. sample with the large surface features) with equation 5.12 with satisfying convergence (see figure 5.14). However, similar fit with the DT curve of the 1.4 μm-thick sample (i.e. sample with small surface features) does not gives satisfying convergence. This indicate that the equation 5.12 does not correspond well with the light scattering behavior of all types of LPCVD ZnO:B samples. Similar disagreement has already been observed for Asahi U-type SnO_2:F layers [Zeman 2000].

Equation 5.12 is reported to be a good approximation of the haze parameters only for a certain type of surface morphology [Beckmann 1963]. As mentioned by Krc [Krc 2002], the equation gives a good approximation of *DT* if the roughness of the interface is completely random and has a Gaussian height distribution. In the case of small feature size, the AFM height distribution reveals deviations from the normal distribution.

A condition of validity of the scalar scattering theory is that the correlation length of the interface morphology, which is a lateral parameter of the interface roughness, has to be much larger than the wavelengths of the incident light. For the sample with small surface feature size, this condition is not fulfilled.

These conditions, which are clearly not satisfied for the 1.4 μm-thick sample (i.e. sample with small surface features) explain the disagreement with equation 5.12.

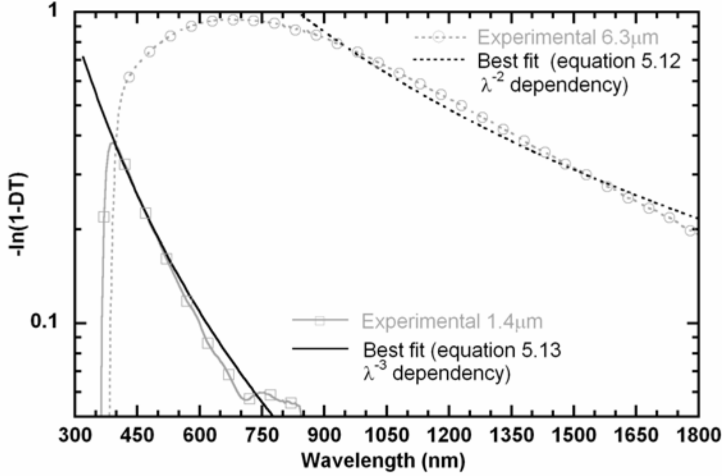

Figure 5.16 *Diffuse transmittance fit with equations 5.12 and 5.13 (see text) of two ZnO layers : one sample 6.3µm-thick with large surface features, and one sample 1.4µm-thick with small surface features. See text for details.*

In order to modelize the diffuse transmittance of layers that have small surface feature size, Zeman [Zeman 2000] introduces an empirical formula derived from equation 5.12:

$$DT = 1 - e^{-\frac{C}{\lambda}\left(\frac{4\pi\sigma_{rms}(n_0 - n_1)}{\lambda}\right)^2} \quad (5.13)$$

C is a fitting factor. In this case, the exponential factor shows a λ^{-3} dependence.

We obtain fit with satisfying convergence, using equation 5.13 for the DT of the 1.4 µm-thick sample.

Figure 5.16 shows experimentally determined DT curves for two rough ZnO layers, the 6.3 µm-thick sample with large surface feature (σ_{RMS} = 226 nm), and the 1.4 µm-thick sample, with small surface features (σ_{RMS} = 60 nm). The plain lines are fits with equations 5.12 and 5.13.

The differences in the angular distribution function (figure 5.15) are related to the morphology of the surface roughness. Theories that model the angular distribution of light scattered by randomly rough interfaces are highly complexe and are not presented here. See [Beckmann 1963] and [Harvey 1989] for a complete review of these models.

We can intuitively explain the phenomenon with the help of theory that has been applied to periodic grating. The light transmitted through a periodic grating will have maxima intensities at angles θ_m given by :

$$\sin\theta_m = \frac{m\lambda}{\Lambda} \qquad (5.14)$$

where m is an integer, Λ is the period of the grating, and λ is the wavelength in the media. Considering the first order of diffraction $m = 1$, the light is scattered at large angle for structure with a period Λ that is small compared to the wavelength in the media.

Intuitively, it is possible to consider a randomly textured interface as a random superposition of periodic gratings. In this case, we regard the value of the lateral feature sizes of the random textured interface as the center of the distribution of the periods of these superposed gratings. Applying this assumption to equation 5.14 explain the fact that the 1.4 µm sample with small surface features diffuse the light at larger angles compared to the 6.3µm sample with large surface features. Note that this behavior is very important for solar cell integration of rough TCO, because light scattered with large angles is more efficiently trapped [Haase 2007]. We discuss now the tendencies of the total transmittance of the samples.

In the NIR range, the *TT* increases with the increasing thickness of the samples. Thick ZnO layers have lower absorbance than thin ones although they have larger thicknesses. This is due to a drastically reduced free carrier absorption in the NIR range, see 5.1.3. In the visible range, the *TT* decreases with the increasing thickness of the samples. We link this phenomenon to higher absorptance related with the increasing thickness of the films. However, as the doping level is low for the thick sample, the residual free carrier absorption is not sufficient to explain the low value of *TT*. During the measurement in air (see 3.2.1), in addition to the absorption of the sample and the expected reflection at each interface, the surface roughness of the TCO-air interface induces additional losses in the *TT*. As the roughness increases, the amount of back scattered light at the TCO-air interface increases leading to higher reflection and thus lower transmittance. In the silicon solar cell device, this additional reflection is considerably lower as the index of refraction of silicon is higher than the index of refraction of air.

Conclusions

We achieved a large variation in surface morphology by varying the thickness and the doping level of LPCVD ZnO:B layers. In this way, we observed different light scattering behaviors. For samples with small feature size, haze factor is low, and light scattering occurs at large angles.

For samples with large surface features, haze factor is high, and light is scattered more near the specular direction. We discuss the consequence of this morphological change on the solar cell current in chapter 7.1.

5.3 Raman analysis

This section presents Raman spectroscopy measurements on LPCVD ZnO:B.

Experimental results

We deposit a series of 2 μm-thick ZnO samples with three different doping levels. We obtain carrier densities of 2.8 $10^{19}cm^{-3}$, 1.1 $10^{20}cm^{-3}$, and 2.0 $10^{20}cm^{-3}$ by varying the gas phase doping ratio $[B_2H_6]/[DEZ]$ ($[B_2H_6]/[DEZ]$ equal to 0, 0.6, and 1.2 respectively).

We characterize the samples by micro-Raman backscattering spectroscopy (see 3.2.5). Raman spectra are recorded using the 633 nm line of a HeNe laser as the exitation source. We measure all spectra at room temperature in the backscattering configuration.

Figure 5.17 shows the shifted Raman spectra of the three measured samples as a function of the wavenumber. For all samples, the sharp peak of the wurtzite ZnO E_2 phonon mode [Bundesmann 2003] is visible at 438 cm^{-1}. As the doping level increases, the intensity of the 438 cm^{-1} line progressively decreases contrary to the intensity of other mode at 580 cm^{-1} that increases. Also, a shoulder appears at 470 cm^{-1}.

Discussion

Authors [Limmer 1998, Wieser 1999] link changes in the Raman spectra of ZnO films with disorder in the layer. Manjón [Manjón 2005] attributes the line at 580 cm^{-1} to a Raman scattering mode caused by doping disorder in ZnO. The incorporation of dopants caused a breakdown of the translational lattice symmetry leading to the emergence of additional modes. In our case, the increasing intensity of the phonon mode at 580 cm^{-1} and its correlation to the doping level constitute a signature of the disorder in the layers due to the incorporated boron.

The decreases of the 438 cm^{-1} line and the increases of the shoulder at 470 cm^{-1} could also be attributed to the disorder induced by the boron incorporation .

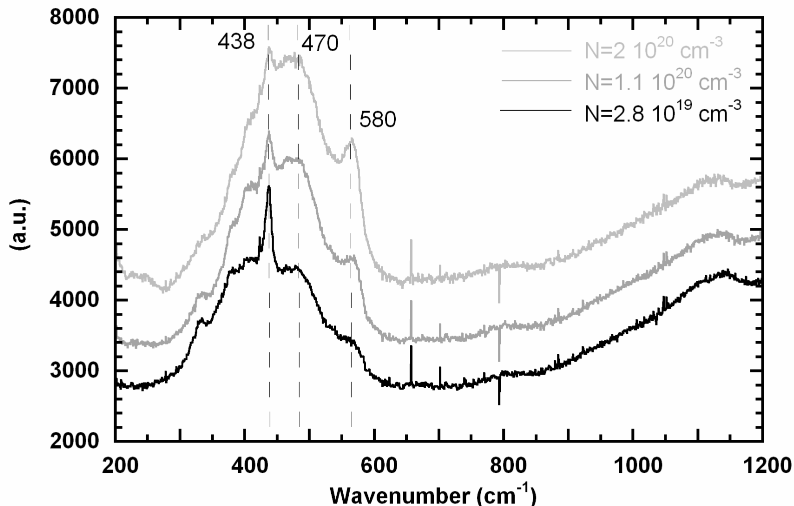

Figure 5.17 *Raman spectra of LPCVD films deposited with gas phase doping ratios B2H6/DEZ equal to 0, 0.6, and 1.2 leading to carrier density of 2.8 $10^{19}cm^{-1}$, 1.1 $10^{20}cm^{-1}$, 2.0 $10^{20}cm^{-1}$ respectively.*

Conclusions

The incorporation of boron in LPCVD ZnO:B layers increases the contribution of a molecular line-vibrational modes in the Raman spectra. Therefore, we can use these modifications of the Raman spectra as indications of the presence of dopants in LPCVD ZnO:B films.

5.4 Conclusions

In this chapter, we presente an important understanding of the mechanisms that govern the optical properties of LPCVD ZnO:B layers. We verify the validity of the Drude model in the visible and IR part of the spectrum for LPCVD ZnO:B layers with various doping level. Therefore, it is possible to predict the reflection and absorption of LPCVD ZnO:B films in the visible and infrared region using this model. We demonstrate that free carrier absorption is the predominant absorption mechanism in LPCVD ZnO:B in the NIR and also the visible range. We obtain highly transparent layers (with an absorption coefficient $\alpha < 20cm^{-1}$) by reducing the doping level of the film and thus the free carrier absorption.

We describe the link between the carrier density value of LPCVD:B ZnO films and the band gap energy value. In LPCVD ZnO:B the band gap

energy shifts toward higher energies by increasing the carrier density, following a Burnstein-Moss plus band gap narrowing model.

We relate the light scattering properties of LPCVD ZnO:B layers to the surface texture parameters. Basically, the total scattered light intensity depends on the roughness of the film. The light scattering angles depend on the lateral size of the surface texture. We achieved LPCVD ZnO:B films with a haze value greater than 80 %.

Finally, we demonstrate that Raman measurements can be used for the detection of the boron incorporation in LPCVD ZnO:B layers.

CHAPTER 6 *Electrical properties of LPCVD ZnO:B films*

This chapter presents the electrical properties of LPCVD ZnO:B films. First, we analyze the influence of the doping level on the electrical properties of LPCVD ZnO:B films. Then, we discuss the electrical model that we introduced in chapter 2, with the results of three different experiments : 1) the comparison between the Hall and optical mobility and carrier density as a function of the doping level, 2) the measurement of temperature dependence of the conductivity, and 3) the measurement of the electrical properties of LPCVD ZnO:B films during exposure to water vapor.

6.1 Overview of the electrical properties of LPCVD ZnO:B films

This section describes the resistivity, the carrier density and the mobility of LPCVD ZnO:B layers. We analyze the influences of doping level variations on these physical properties.

Experimental results

A series of samples with various gas phase doping ratios $[B_2H_6]/[DEZ]$ within the range of 0 to 2 is deposited on glass substrates. In this series, we seek a constant grain size in order to keep the influence of the grain size on the carrier mobility stable. Incorporating boron influences the grain size of the layers [Faÿ 2003]. In consequence, we adapt the thicknesses of the films in order to reach a constant surface grain size. Therefore, the thicknesses of the samples vary slightly between 2.0 μm and 2.3 μm inducing lateral grain size of ~300 nm.

We perform thickness (see 3.1.1), resistivity and Hall (see 3.3) measurements for all the series of the samples (table 6.1).

Figure 6.1 shows the measured resistivity ρ as a function of the Hall carrier density N_{Hall}. The correspondence between the gas flow ratio and the carrier

Table 6.1 *The measured electrical parameters μ_{Hall}, N_{Hall}, and σ_{Hall} for LPCVD ZnO:B films grown with gas phase doping ratio $[B_2H_6]/[DEZ]$ varied from 0 to 2.*

$[B_2H_6]/[DEZ]$	d (μm)	ρ ($\times 10^{-3}$ Ωcm)	σ (Scm^{-1})	μ_{Hall} ($cm^2V^{-1}s^{-1}$)	N_{Hall} ($\times 10^{19}$ cm^{-3})
0	2.2	13.3	75	23	1.9
0.15	2.1	6.89	145	26	3.7
0.3	2.2	3.4	294	29	6.4
0.6	2.2	1.98	503	30	10.3
1	2	1.39	718	29	14.6
1.25	2	1.27	782	27	18.5
1.5	2.3	1.33	751	23	21.0
2	2.2	1.38	724	22	21.7

density is shown on the two abscissa axes of the graph. For the unintentionally doped layer, i.e. $[B_2H_6]/[DEZ] = 0$, the carrier density value is 1.9 10^{19} cm^{-3} and the resistivity value is 1.3 10^{-2} Ωcm. As the gas flow ratio increases, the carrier density rises to 2.2 10^{20} cm^{-3}, leading to a decrease in resistivity down to 1.3 10^{-3} Ωcm for the sample deposited with $[B_2H_6]/[DEZ] = 2$.

Figure 6.2 shows the Hall mobility μ_{Hall} of the same series of samples as a function of the Hall carrier density N_{Hall}. For unintentionally doped layer, i.e. $[B_2H_6]/[DEZ] = 0$, μ_{Hall} is equal to 23 $cm^2V^{-1}s^{-1}$. As long as N_{Hall} is inferior to 10^{20} cm^{-3}, μ_{Hall} increases with the increasing carrier density. The mobility reaches a maximum value of 30 $cm^2V^{-1}s^{-1}$ for a film with a carrier density of 1.0 $10^{20}cm^{-3}$. For films with $N_{Hall} > 1.0$ $10^{20}cm^{-3}$, μ_{Hall} changes its tendency and decreases with the increasing carrier density. We measured the value of 21 $cm^2V^{-1}s^{-1}$ at a carrier density of 2.2 $10^{20}cm^{-3}$ for the sample deposited with $[B_2H_6]/[DEZ] = 2$.

Discussion

We first discuss the high value of the carrier density $N_{Hall} = 2.0$ 10^{19} cm^{-3} of the non-intentionally doped film. This high value obtained without extrinsic dopant, can partly be caused by deviation from stoichiometry. In fact, LPCVD ZnO film shows an excess of zinc (see 4.2.3) likely linked to defects such as zinc interstitial or oxygen vacancies. These defects act as shallow donors and constitute dopants [Jagadish 2006, Tomlins 2000, Look 1999]. In addition to this stiochiometry deviation, Van de Walle [Van de Walle 2000] demonstrate that hydrogen constitutes shallow donors in zinc oxide. Since the LPCVD process introduces hydrogen in the films (see 4.2.3), this effect can also contribute to the relatively high value of N measured in non-intentionally doped samples.

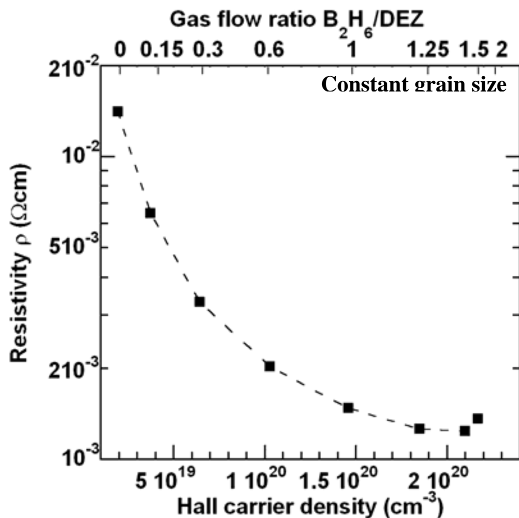

Figure 6.1 *The resistivity ρ versus the free carrier density N_{Hall} for ZnO films grown with gas phase doping ratio $[B_2H_6]/[DEZ]$ varied from 0 to 2. The curve is a visual guide.*

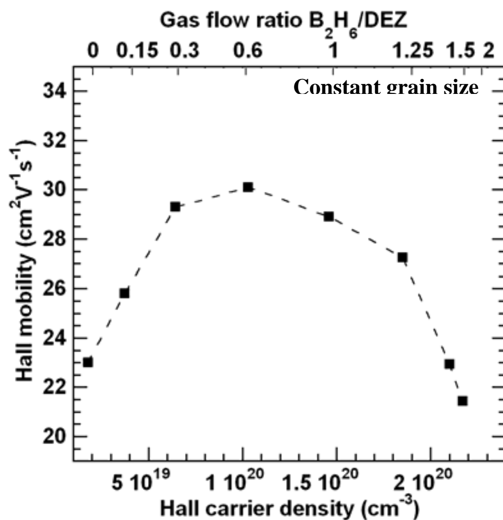

Figure 6.2 *The Hall mobility μ_{Hall} versus the free carrier density N_{Hall} for LPCVD ZnO:B films grown with gas phase doping ratio $[B_2H_6]/[DEZ]$ varied from 0 to 2. The curve is a visual guide.*

Varying the doping level of LPCVD ZnO:B films strongly influences their electrical properties. In our case, increasing the $[B_2H_6]/[DEZ]$ gas flow ratio incorporates more boron in the film, inducing a strong increase of the carrier density. Group III atoms such as boron act as extrinsic n-type dopant in zinc oxide. It is assumed that they are substitutionaly incorporated at the zinc lattice sites, releasing an additional electron (not required for the bonding) to the conduction band [Jagadish 2006].

As the carrier density in LPCVD ZnO:B is high ($N_{Hall} > 2.0\ 10^{19}$ cm^{-3}), the classical description of charge transport in metals applies [Exarhos 2007] (see 2.2.3). The electrical resistivity is given by :

$$\rho = \frac{1}{\sigma} = \frac{1}{eN_{Hall}\mu_{Hall}} \qquad (6.1)$$

where σ is the conductivity, N_{Hall} is the carrier density, μ_{Hall} their mobility and e is the elementary charge of the electron.

From equation 6.1, we see that increasing the carrier density of the film by doping with boron is a very convenient way to lower the resistivity. However, for solar cells applications, it is undesirable to have too high carrier densities because of enhanced free carrier absorption in the near infrared range (see 5.1.1). Therefore achieving high carrier mobility constitutes an important issue in order to fabricate films with both high conductivity and high transparency.

Figure 6.1 shows that the resistivity does not vary linearly with the inverse of the carrier density, in disagreement with what is expected from equation 6.1. This behavior is related to the fact that the carrier mobility is a function of the carrier density (see 2.2.3).

The relationship between μ_{Hall} and N_{Hall} for the deposited serie of LPCVD ZnO:B layers is shown in figure 6.2. We have to discuss this behavior keeping in mind the theory developed in section 2.2.3 and illustrated in figure 2.5. For lightly doped films ($N_{Hall} < 1.0\ 10^{20}$cm^{-3}), the increasing mobility with the increasing carrier density indicates a mobility limited by grain boundary scattering [Ellmer 2007, Minami 2000]. We explain this scattering mechanism in section 2.2.3. Basically, filled traps states form potential barriers at the grain boundaries and limit the electronic transport.

As long as $N < 10^{20}$ cm^{-3}, μ_{Hall} increases with the increasing carrier density. We explain this behavior by an increasing carrier concentration that facilitates the transport by lowering and narrowing the potential barrier at grain boundaries (see 2.2.3).

For N_{Hall} > 1.0 10^{20}cm^{-3}, we relate the decrease in the mobility with the increasing carrier density to bulk scattering. For heavily doped TCO the main scattering mechanism is usually attributed to ionized-impurity scattering [Minami 2000, Ellmer 2001, Young 2000, Zhang 1996, Minami 1985]. This scattering mechanism has a $\mu = f(N)$ behavior that is in agreement with the behavior of the mobility observed here (see 2.2.3).

However, Agashe [Agashe 2004] reported a high mobility value of 44.2 cm^{2}V^{-1}s^{-1} for heavily doped sputtered ZnO:Al (N > 4.0 10^{20}cm^{-3}), in which mobility is limited by intragrain ionized impurity scattering. Ellmer [Ellmer 2001] used the Masetti formula to fit experimental data for ZnO from various fabrication processes (see 2.2.3) and found a mobility of around 40 cm^{2}V^{-1}s^{-1} for film with N ~ 2.0 10^{20} cm^{-3} . Here, the mobility limitation is attributed to ionized impurity scattering and clustering scattering.

The relatively low mobility of heavily doped LPCVD ZnO:B, i.e. 23 cm^{2}V^{-1}s^{-1} at 2.0 10^{20} cm^{-3}, indicates that additional bulk scattering phenomena occur. As reviewed by Ellmer [Ellmer 2001], we can explain this lower mobility compared to the mobility calculated for ionized impurity scattering values by several other mechanisms that could occur in LPCVD ZnO:B. These include the formation of impurity clusters and neutral defects, higher charge state of the ionized donors (due to self doping by oxygen vacancies) or extrinsic dopants on interstitial sites. The distinction between these mechanisms demands high-level analysis of the temperature dependence of the mobility, which is not carried out in this study.

Conclusions

By varying the gas flow ratio [B_2H_6]/[DEZ] between 0 and 2, we achieved ZnO:B films with resistivity varying by a factor of 20. This make the LPCVD process a convenient technique for the optimization of the resistivity of ZnO films.

We show that different scattering behavior occurs depending on the carrier density value. The doping series of LPCVD ZnO:B layers show a continuous transition from a grain boundary scattering limited mobility at low doping level to a bulk scattering limited mobility at high doping level. These assumptions will be further validate in the next sections.

6.2 Advanced electrical characterizations

In this section, we present an experiments done to achieve a better understanding of the electronic transport mechanisms in LPCVD ZnO:B films and validate our interpretation done in section 6.1. First, an optical method to extract the intragrain mobility and carrier concentration is described and applied to LPCVD ZnO:B films. Then, we measure and

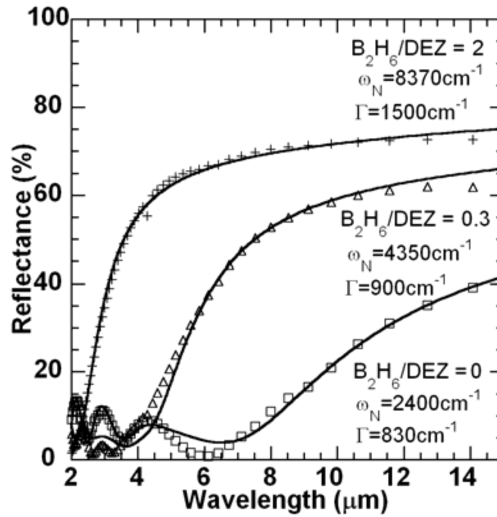

Figure 6.3 *Examples of fits applying the Drude model (solid lines) to near normal measured reflectance spectra of ZnO films (symbol) deposited with different gas phase doping ratio [B_2H_6]/[DEZ].*

discuss the temperature dependence of the conductivity. Finally, we study the variation of the electrical properties of LPCVD ZnO:B films during an exposure to a humid environment.

6.2.1 Optical measurements of electrical parameters

Experimental results

In TCO materials, the optical properties are closely linked to the electrical ones. Section 5.1.3 shows that the Drude model in its simplest form is sufficient to describe the NIR optical behavior of LPCVD ZnO:B films. We obtain good agreement between modelized reflectance spectra and the experimental data using the unscreened plasma frequency ω_N and the damping frequency Γ as fitting parameters.

These near infrared optical parameters are coupled to the charge transport. The density of charge carriers is related to the plasma frequency with (see 2.1.2):

$$\omega_N^2 = \frac{N_{Optic} e^2}{\varepsilon_0 m} \tag{6.2}$$

Table 6.2 *The fitting factors Γ and ω_N resulting from best fit to the infrared reflectance spectra. The optical electrical parameters μ_{optic}, N_{optic}, and σ_{optic} deduced from the fit for ZnO films grown with gas phase doping ratio $[B_2H_6]/[DEZ]$ varied from 0 to 2. The measured Hall electrical parameters μ_{Hall}, N_{Hall}, and σ_{Hall} are given for comparison.*

$[B_2H_6]/[DEZ]$	t (μm)	ω_N (cm^{-1})	Γ (cm^{-1})	μ_{optic} ($cm^2 V^{-1} s^{-1}$)	μ_{Hall} ($cm^2 V^{-1} s^{-1}$)	N_{optic} ($\times 10^{19}$ cm^{-3})	N_{Hall} ($\times 10^{19}$ cm^{-3})	σ_{optic} (S cm^{-1})	σ_{Hall} (S cm^{-1})
0	2.2	2400	830	41	23	1.8	1.9	118	75
0.15	2.1	3600	900	37	26	4.0	3.7	236	145
0.3	2.2	4350	950	35	29	6.0	6.4	336	294
0.6	2.2	5700	1060	31	30	10.3	10.3	510	503
1	2	7400	1170	28	29	17.0	14.6	760	718
1.25	2	7700	1200	27	27	18.5	18.5	800	782
1.5	2.3	8200	1430	23	23	21.0	21.0	772	751
2	2.2	8370	1500	22	22	21.7	21.7	763	724

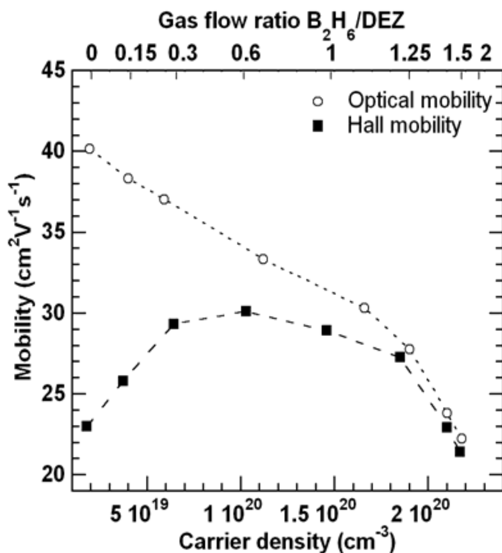

Figure 6.4 *The optical and the Hall mobilities versus the free carrier density for ZnO films grown with gas phase doping ratio (B2H6/DEZ) varied from 0 to 2. Curves are visual guide.*

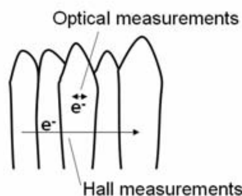

Figure 6.5 *Illustration of an electron displacement under optical and DC excitation (Hall measurements).*

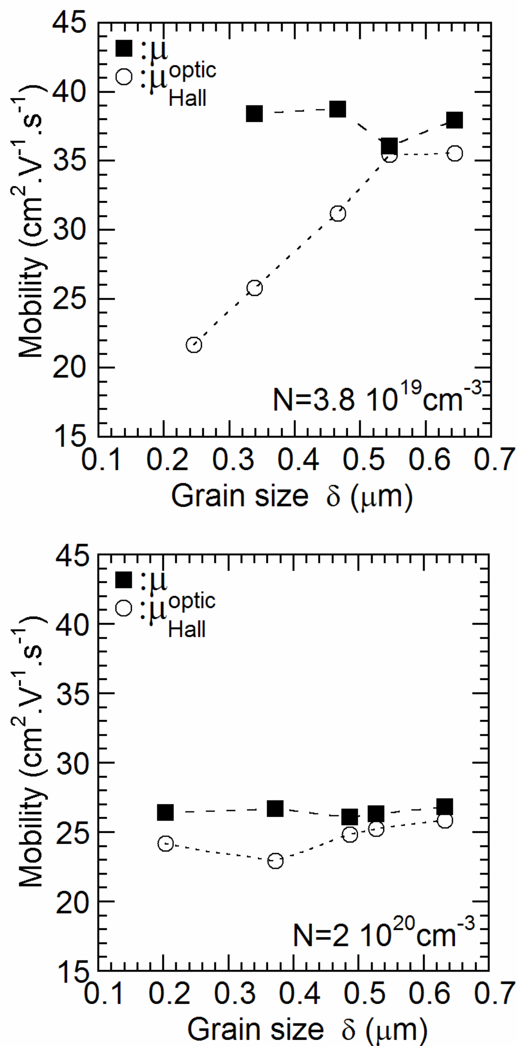

Figure 6.6 *The optical (circles) and Hall (squares) electron mobility as a function of grain size for films with a carrier density N=3.8 10^{19}cm^{-3} (top) and N=2 10^{20}cm^{-3} (bottom).*

where N_{optic} is the free electron density, e the electron charge, ε_0 the permittivity of free space and m the electron effective mass.

The optical mobility μ_{optic} is given by the equation (see 2.1.2) :

$$\mu_{Optic} = \frac{e}{\Gamma m} \qquad (6.3)$$

We obtain the optical conductivity from :

$$\sigma_{Optic} = eN_{Optic}\mu_{Optic} \qquad (6.4)$$

We measure and fit the infrared reflection of the previous series of samples having a variation of gas phase doping ratio $[B_2H_6]/[DEZ]$ from 0 to 2 and constant grain size to the Drude model (see spectra in figure 6.3, also in 5.1.3). Assuming $\varepsilon_\infty = 4$ and $m = 0.28m_0$ where m_0 is the electron mass [Ellmer 2001, Jin 1988], and using ω_N and Γ deduced from the fit with the experimental infrared reflectance spectra (see 5.1.3), the optical mobility μ_{optic} and carrier density N_{optic} are extracted using equations 6.2 and 6.3.

Table 6.2 summarizes the used fitting parameter Γ and ω_N and the deduced optical electrical parameters μ_{optic}, N_{optic} and σ_{optic} for all the samples. The measured Hall electrical parameters μ_{Hall}, N_{Hall} and σ_{Hall} are given for comparison.

Figure 6.4 shows the optical mobility μ_{optic} and the Hall mobility μ_{Hall} of the samples as a function of the optical carrier density N_{optic} and the Hall carrier density N_{Hall} respectively. For all measured samples, we found a value of the Hall electron density close to the one deduced from the optical measurements (within the measurement's uncertainty). This remarkable agreement strongly supports the validity of the Drude model and the chosen values for m and ε_0.

For the unintentionally doped layer, μ_{optic} has a value of 41 $cm^2V^{-1}s^{-1}$, much higher than the value of $\mu_{Hall} = 23$ $cm^2V^{-1}s^{-1}$. As long as $N < 1.0\ 10^{20}$ cm^{-3}, μ_{Hall} increases with the increasing carrier density, contrary to μ_{optic}. For $N > 1.0\ 10^{20}$ cm^{-3}, μ_{optic} and μ_{Hall} become similar and decrease with the increasing doping level.

We deposit two other series of samples. They consist of an increasing grain size series obtained by changing the film's thicknesses. The gas phase doping ratios are set to $[B_2H_6]/[DEZ] = 0.1$ and $[B_2H_6]/[DEZ] = 2$ leading in two different carrier densities : $N_{Hall} = 3.8\ 10^{19}$ cm^{-3} and $N_{Hall} = 2.0\ 10^{20}$ cm^{-3} for each series of samples, respectively.

Figure 6.6 shows μ_{hall} and μ_{optic} as a function of the grain sizes δ for the two series with different thicknesses of ZnO:B samples.

For ZnO:B layers with the low carrier concentration (N = 3.8 10^{19} cm^{-3}), the Hall mobility is found dependent on δ: it increases from 22 to 36 $cm^2V^{-1}s^{-1}$ with the increasing grain size. In contrast, the optical mobility of these samples remains constant at a high value of 38 $cm^2V^{-1}s^{-1}$, independently of the grain size. For heavily doped samples (N = 2 10^{20} cm^{-3}) both Hall and optical mobility remain nearly constant at a value around 25 $cm^2V^{-1}s^{-1}$, while δ is increased.

Discussion

Before discussing the results themselves, it is necessary to explain the differences between the optically deduced electrical parameters and the electrical parameter measured by Hall effect.The calculated electron mean free path in ZnO is in the range of a few nm (see 2.2.3) and, with the application of a rapidly oscillating electric field (i.e. under NIR light excitation) the average electron path length is much smaller than the typical grain size [Minami 2000, Guglielmi 1998]. Therefore, grain boundary scattering will not influence the measured value for the optical mobility, and only intra-grain scattering will influence μ_{optic}. Note that the depleted region at grain boundaries occupies only a small volume compared to the bulk of the grain and will not affect the optical measurements.

In the case of the Hall effect measurement, electrons have to travel over a macroscopic length (across several grain boundaries) and consequently both bulk scattering and grain boundary scattering will influence the measured value of μ_{hall}.

Figure 6.5 illustrates the scale of the displacement experiment by an electron when excited optically or with a DC source, e.g. during Hall effect measurements.

For the doping series of samples (figure 6.4), i.e. for samples with N < 1.0 $10^{20}cm^{-3}$, experimental results show differences between the optical and the Hall mobility values. For lightly doped layers, μ_{optic} has a value of 41 $cm^2V^{-1}s^{-1}$, much higher than the value of μ_{Hall} = 23 $cm^2V^{-1}s^{-1}$. As grain boundary scattering only affects the Hall mobility and as optical mobility is an indication of the bulk mobility, these differences evidence that at low doping level, μ_{Hall} is limited by grain boundary scattering. This result is consistent with the conclusion of section 6.1 that affirms that this scattering effect is dominant for lightly doped LPCVD ZnO:B layers.

For N > 1.0 $10^{20}cm^{-3}$, μ_{optic} and μ_{Hall} are close and decrease with the increasing carrier density, indicating that the intragrain scattering becomes the main limiting factor of the electron mobility. In this case, due to the

high carrier density, the potential barrier at grain boundary is low and narrow, facilitating thermionic emission and tunneling over and through the potential barrier. Therefore, grain boundary scattering no longer limits the conductivity (see 2.2.3).

In consequence, as the carrier density increases, we show a continuous transition in the behavior of μ between a mobility mainly limited by grain boundary scattering and a mobility mainly limited by intragrain bulk scattering. The carrier density value for which the main limiting scattering mechanism changes from grain boundary scattering to bulk scattering is around 1.0 10^{20} cm^{-3}.

Considering figure 6.6 and as discussed in the previous paragraph, for the lightly doped ZnO:B film, the observed differences between optical intra-grain mobility and Hall mobility values are due to grain boundary scattering limited mobility. As the grain size is increased, the grain boundary density is reduced. Therefore, the grain boundary scattering influence on μ_{Hall} decreases and μ_{hall} and μ_{optic} become almost identical. For $\delta > 600$ nm, the grain boundary scattering becomes too low to influence the measured Hall mobility. Therefore, obtaining high mobility close to the bulk mobility in low-doped LPCVD ZnO films is achievable by increasing the grain size through (in this case) an increase of the thickness of the film.

At heavy doping level (figure 6.6 right), grain boundary scattering plays only a minor role compared to intra-grain scattering mechanisms. Here, the optical and Hall mobility values become almost identical and the variation of grain size no longer affects the Hall mobility.

Conclusions

Using results from optical measurement of the mobility and carrier density, we confirm the conclusion of section 6.1 that shows that different scattering mechanisms limit the DC mobility, depending on the carrier density value. The maximum mobility achievable by increasing the grain size is determined for low-doped samples, reaching a value close to 40 $cm^2V^{-1}s^{-1}$.

6.2.2 Temperature dependence of the conductivity

Experimental results

We deposit a series of five LPCVD ZnO:B films with a gas phase doping ratio $[B_2H_6]/[DEZ]$ varying from 0 to 1. Table 6.3 summarizes the electrical parameters measured at room temperature for all the samples of the series.

Table 6.3 *The measured electrical parameters μ_{Hall}, N_{Hall}, and σ_{Hall} for LPCVD ZnO:B films grown with gas phase doping ratio[B_2H_6]/[DEZ] varied from 0 to 1.*

[B_2H_6]/[DEZ]	t (μm)	ρ (×10^{-3} Ωcm)	σ (Scm^{-1})	μ_{Hall} ($cm^2V^{-1}s^{-1}$)	Extrapolated μ_{Optic} ($cm^2V^{-1}s^{-1}$)	N_{Hall} (×10^{19} cm^{-3})
0	2.2	18.8	53	30	42	1.1
0.15	2.2	6.02	166	31	40	3.3
0.3	2.3	3.13	319	35	38	5.6
0.7	2.4	1.58	631	36	36	10.9
1	2.2	1.53	653	32	34	12.5

Figure 6.7 shows the measured dependence of the conductivity σ as a function of the inverse of the temperature T^{-1} measured from T = 300 K down to T = 30 K (see 3.3.3).

Below 150 K, σ remains almost constant. The strong differences in the absolute values of the conductivity are due to the different doping ratios used for each sample.

From 150 K to room temperature, σ becomes temperature dependent with two different trends, depending on the doping level of the films. σ increases with T for undoped and lightly doped samples (i.e. [B_2H_6]/[DEZ] < 0.7), whereas, for heavily doped films (i.e. [B_2H_6]/[DEZ] > 0.7), σ is reduced when T is increased.

Figure 6.8 shows simulated curves of dependence of the conductivity σ as a function of the inverse of the temperature T^{-1}, calculated with the model described in chapter 2. For the calculation, we use equations 2.17, 2.28, and 2.35 for the various mobility contributions. The parameters are set to L = 300 nm, $N_t = 8\ 10^{12}$ cm^{-2}, $m = 0.28m_e$, T = 300 K and l_{tun} = 5 nm. We shows in section 6.2.1 that the Masetti mobility is over evaluated for our LPCVD ZnO:B layers. Therefore, we take the extrapolated optical mobility as bulk mobility (see table 6.3). We deduce the total conductivity from equation 2.42 and 2.14. We vary the carrier density in the model according to the carrier density of the series of samples measured by the Hall effect.

Discussion

As the mobility only slightly varies between the samples, the strong differences in the absolute values of the conductivity are mainly due to differences in the carrier density. LPCVD ZnO:B films exhibit a finite conductivity at low temperature. The experimental data only extend down to the temperature of 30 K, but it can be extrapolated for lower temperatures, conductivity is higher than zero even for intrinsic samples. This behavior is explained by the degeneracy of the films

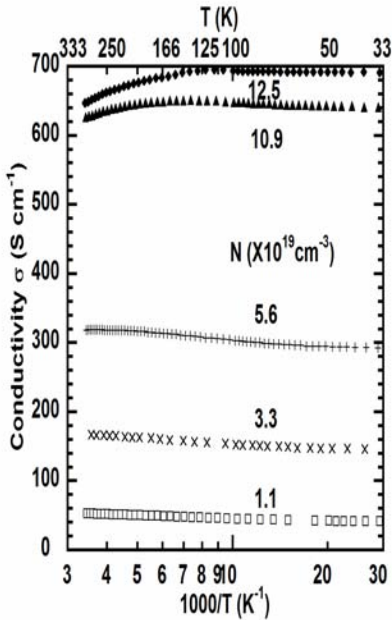

Figure 6.7 *The experimental measured dependence of the conductivity σ as a function of inverse of the temperature T^{-1} for ZnO films gas phase doping ratio [B_2H_6]/[DEZ] varied from 0 to 1. The measured Hall carrier density values are indicated on each curve.*

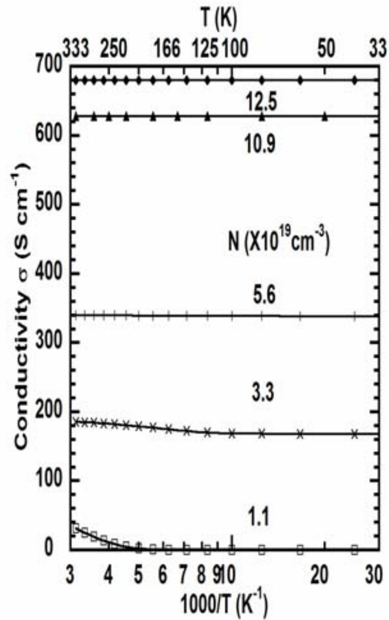

Figure 6.8 S*imulated curves of dependence of the conductivity σ as a function of the inverse of the temperature T^{-1}calculated with the model described in chapter 2. For the calculation, we use equations 2.17, 2.28, and 2.35 for the various mobility contributions. The parameters are set to L = 300 nm, N_t = 8 10^{12} cm^{-2}, m = 0.28m_e, T = 300 K and l_{tun} = 5 nm, the bulk mobility is the extrapolated optical mobility taken from table 6.3. We deduce the total conductivity from equations 2.42 and 2.14. We vary the carrier density value in the model according to the carrier density of the series of samples measured by the Hall effect, the value taken are indicated on each curve.*

due to the high concentration of the doping center, i.e. O vacancies, Zn interstitial and extrinsic doping with boron. The high quantity of defects forms an impurity band that overlaps the bottom of the conduction band (see 2.2.1). The degenerate electrons form a free electron gas that occupies the bottom of the conduction band and the impurity band and therefore participating to the conduction even at low temperature.

At temperatures higher than 100 K the conductivity starts to show a temperature dependence. We can link these dependencies to the transport scattering mechanisms.

The grain boundary scattering limited electronic transport is characterized by an increasing conductivity with the temperature. This behavior results from a thermionic current over the potential barrier height present at grain boundaries [Seto 1975]. The LPCVD ZnO:B samples with $N < 1.0\ 10^{20}\text{cm}^{-3}$ exhibit such a dependency, which confirms the results of previous sections, that conclude with a grain boundary scattering limited mobility at low doping level.

The decrease of the conductivity when the temperature is increased is observed for heavily doped ZnO:B in figure 6.7. This is characteristic of a metal-like behavior, for which the mobility is limited by thermal lattice vibration and depends inversely on the temperature. The positive temperature dependency of the conductivity is cancelled due to grain boundary scattering. Indeed, when the doping is increased, the potential barrier becomes smaller due to the higher carrier density in the grain as illustrated by figure 6.9. Field assisted tunneling through the potential barrier becomes dominant compared to thermionic emission. The transport by tunneling is independent of the temperature [Roth 1981].

These results shows that a transition from thermionic-like temperature dependency of the conductivity to metallic-like temperature dependency of the conductivity takes place with the increasing carrier density. Such a transition is also observed in pulsed laser deposited ZnO:Ga by [Bohsle 2006].

We reinforce the previous interpretations by comparing the experimental results with the calculated temperature dependence of the conductivity using the model described in chapter 2 (figure 6.8). This model takes into account the transport mechanisms previously discussed : a temperature dependent thermionic scattering over the barrier and temperature independent tunneling and bulk scattering.

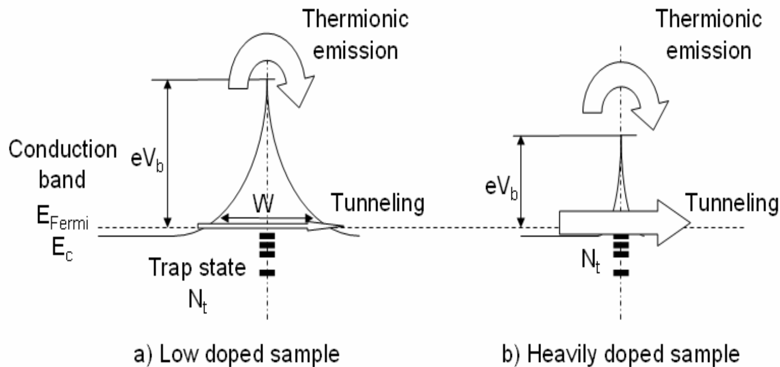

Figure 6.9 *The schematic drawing of the current path through a grain boundary barrier for lightly doped and heavily doped ZnO layers.*

We explain the differences with the experimental results in absolute conductivity values and the non-appearance of the decrease of the conductivity when the temperature is increased for heavily doped simulate ZnO, by the fact that we use the extrapolated optical mobility as bulk mobility.

Doing this we assume a bulk mobility independent of the temperature, which is not the case in real films. Further investigation, not carried out here, using model for the temperature dependence of the bulk mobility need to be performed to get better fit with the experimental data.

For lightly doped films, the differences between experimental and simulated temperature dependence of the conductivity is explain by the fact we use a simple thermionic emission model. Real films probably have a more complex mechanisms involving also thermionic field emission or variable range hopping transport [Myong 2007, Sze 1981].

However, despite these approximations, we obtain trends with the model that are similar to the experimental results. The good agreement obtained between the experimental and modelized conductivity corroborate our interpretations.

Conclusions

We again confirm the results of section 6.1 with the analysis of the temperature dependency of the conductivity. In this section we found that thermionic-like conduction related to grain boundary barrier influences the conductivity in lightly doped ZnO samples, whereas in heavily doped ZnO films, metal-like conduction limited by grain bulk scattering mechanisms occurs.

6.2.3 Water vapour exposure

The electrical properties of ZnO are affected by exposure to a humid atmosphere [Tohsophon 2006]. The stability of these films in a humid environment is a crucial issue for the use of these films as TCO in thin film silicon PV modules. In fact, in order to be commercialized, the modules have to pass the so called damp-heat test that consists of 1000 hours exposure in 85% humidity at 85°C. Studying the stability in humid environments allows us to understand the fundamental mechanism that governs such undesirable behavior.

Experimental results

We deposit a standard LPCVD ZNO:B film designed for aSi:H. See 4.4 for the details about deposition parameters and layers characteristics. After deposition, non encapsulated films are submitted to damp heat i.e. 100% relative humidity at a temperature of 40°C in an oven. These conditions are different from the standardized test (85°C, 85% humidity) to slow down the degradation kinetics in order to precisely record the changes in the electrical characteristics of the films.

Hall measurements, optical measurements of the electrical characteristics and conductivity σ measurements as a function of the temperature from T = 300 K down to T = 30 K are done on films exposed for varying durations.

Figure 6.10, 6.11 and 6.12 show the resistivity, the optical and Hall carrier density, and the optical and Hall mobility respectively as a function of the damp heat exposure time for a film with $N = 1.2\ 10^{20}$ cm^{-3}.

After 800 hours of damp heat exposure, the resistivity of the film increases from 2.2×10^{-3} to 4.6×10^{-2} Ω.cm. This increase is mainly due to a sharp drop of the Hall mobility, which decreases from 33 to 2 cm^{2}V^{-1}s^{-1}, whereas the Hall carrier density is only slightly affected. Optical values μ_{optic} and N_{optic}, relevant to intragrain scattering, remain constant after 800 hours of damp heat exposure.

In figure 6.13, the conductivity as a function of the inverse of the temperature is shown for the same sample after varying damp heat exposure times. The shape of the $\sigma(T^{-1})$ curves around ambient temperature change while the damp heat exposure time is increased. The conductivity decreases with the inverse of the temperature for non degraded samples and starts to increases with T^{-1} for longer damp heat exposure.

Figure 6.14 shows simulated curves of dependence of the conductivity σ as a function of the inverse of the temperature T^{-1}calculated with the model described in chapter 2. For the calculation, we use equations 2.17, 2.28, and 2.35 for the various mobility contributions. The parameters are set to

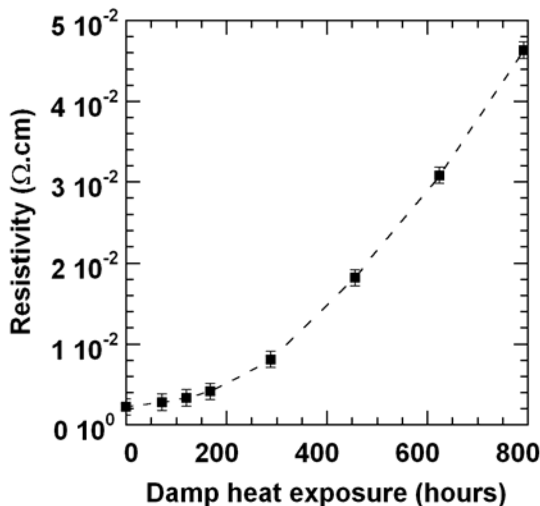

Figure 6.10 *The resistivity as a function of the damp heat exposure (40°C, 100% humidity) for an unencapsulated 2μm- thick ZnO:B.*

L = 300 nm, $m = 0.28m_e$, T = 300 K, l_{tun} = 5 nm, $N = 1.2\ 10^{20}$ cm^{-3},and a bulk mobility extrapolated from the optical mobility measurement μ_{Bulk} = 35 cm^{2}V^{-1}s^{-1}. We deduce the total conductivity from equation 2.42 and 2.14. We set the carrier density in the model according to the carrier density of the samples measured by the Hall effect $N = 1.2\ 10^{20}$cm^{-3}. We progressively need to increase the trap density N_t from 8 10^{12} cm^{-2} to 44.5 10^{12} cm^{-2} in the model in order to simulate the degradation of the sample during damp heat.

To study the effect of the doping level on the damp heat stability, three samples : a lightly doped LPCVD ZnO:B film ($N = 8\ 10^{19}$cm^{-3}), a heavily doped LPCVD ZnO:B film ($N = 2\ 10^{20}$cm^{-3}) and a ZnO film deposited by sputtering, which has a higher carrier concentration ($N = 4\ 10^{20}$cm^{-3}) were deposited and put into damp heat. LPCVD ZnO:B films are 2 µm-thick and the sputtered ZnO film is 1 µm-thick doped with aluminum. We measure the electrical characteristics of the samples as a function of the damp heat exposure.

Figure 6.15 shows the resistivity as a function of damp heat exposure duration. This figure shows that films with lower doping level are less stable against damp heat exposure. We strongly enhance the stability as we increase the doping level in LPCVD films. For sputtered film with a carrier density of $N = 4\ 10^{20}$cm^{-3}, we observe no degradation.

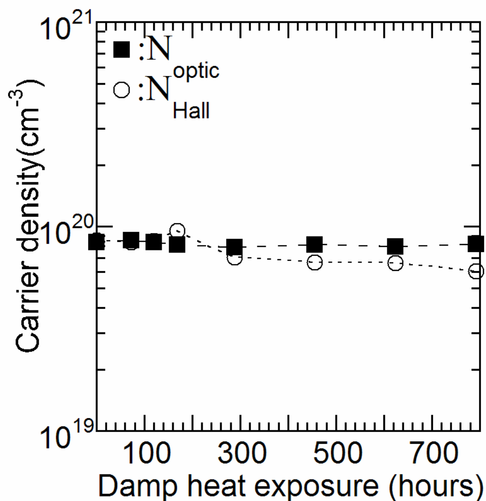

Figure 6.11 *Optical and Hall carrier density as a function of the damp heat exposure (40°C, 100% humidity) for an unencapsulated 2µm-thick ZnO:B.*

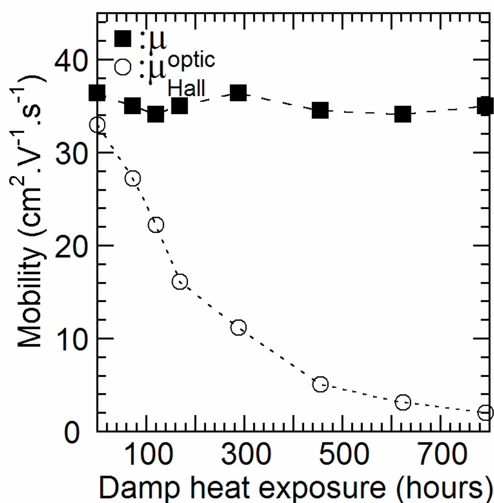

Figure 6.12 *Optical and Hall carrier mobility as a function of the damp heat exposure (40°C, 100% humidity) for an unencapsulated 2µm-thick ZnO:B.*

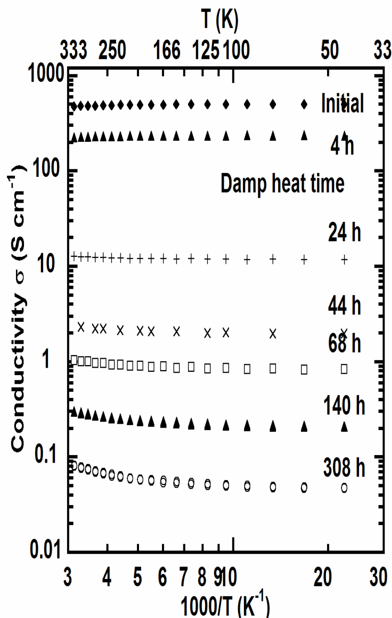

Figure 6.13 *Conductivity as a function of the inverse of the temperature for LPCVD ZnO film during damp heat exposure (40°C, 100% humidity).*

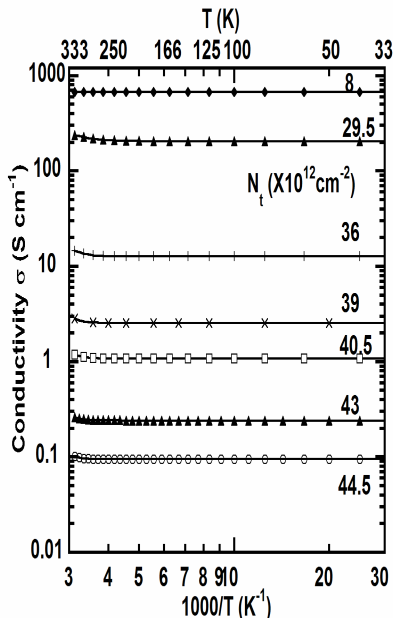

Figure 6.14 *The simulated curves of dependence of the conductivity σ as a function of the inverse of the temperature* T^{-1} *calculated with the model described in chapter 2. For the calculation, we use equations 2.17, 2.28, and 2.35 for the various mobility contributions. The parameters are set to* $L = 300$ *nm,* $m = 0.28m_e$*,* $T = 300$ *K,* $l_{tun} = 5$ *nm,* $N = 1.2\ 10^{20} cm^{-3}$*, and* $\mu_{Bulk} = 35\ cm^2V^{-1}s^{-1}$*. We deduce the total conductivity from equations 2.42 and 2.14. We progressively increase the trap density* N_t *from* $8\ 10^{12}\ cm^{-2}$ *to* $44.5\ 10^{12}\ cm^{-2}$ *in the model in order to simulate the degradation of the sample during damp heat.*

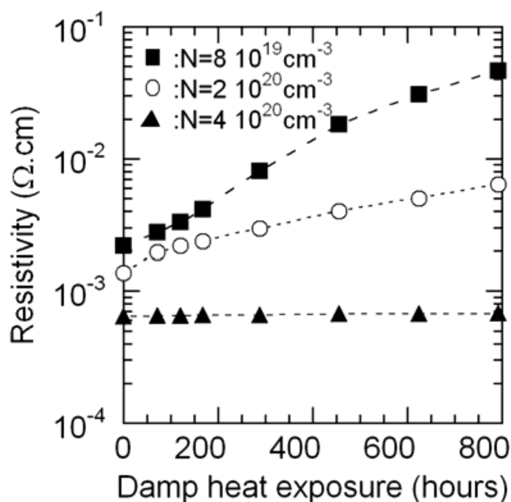

Figure 6.15 *The resistivity as a function of damp heat exposure (40°C, 100% humidity) for a doped LPCVD ZnO ($N=8\times10^{19}cm^{-3}$), a heavily doped LPCVD ZnO ($N=2\times10^{20}cm^{-3}$) and a sputtered ZnO film ($N=4\times10^{20}cm^{-3}$).*

Discussion

Our results indicate that, unprotected LPCVD ZnO:B films show an increase in resistivity during exposure to hot humid atmosphere, mainly due to a decrease in the Hall mobility. The carrier density and the optical mobility remain constant. Following the analysis developed in section 6.2.1, the significant difference between optical and Hall mobility for the degraded samples gives evidence of a electronic transport limited by grain boundary scattering. These results prove that potential barriers at grain boundaries increase after damp heat exposure, leading to higher electron scattering at grain boundary. Intragrain scattering remains stable as confirmed by the stability of μ_{optic}. Figure 6.16 shows a schematic diagram of these mechanisms.

We confirm this interpretation of our observations by measuring the experimental curves of the conductivity as a function of the temperature (figure 6.13) and comparing it with the calculated curves from the model described in chapter 2 (figure 6.14). These curves show a more and more thermionic-governed conductivity as the damp heat time increases.

Tosophon [Tosophon 2006] explain the damp heat degradation of the electrical property of sputtered ZnO:Al by diffusion of water vapor in the film. For LPCVD ZnO:B, diffusion of water vapor at grain boundaries that

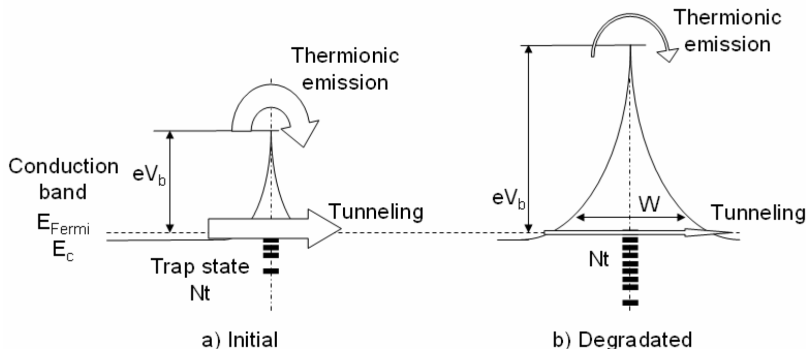

Figure 6.16 *The schematic drawing of the current path trough a grain boundary barrier for initial and damp heat degraded ZnO layers.*

lead to an increase of the trap state density, is in accordance with the experimental and modelized behavior of the films.

The stability differences between samples with different doping levels shown in figure 6.15 could be explained using the model of increasing charge states at grain boundaries during damp heat. A heavier doping of the ZnO grains reduces the width W and the height eV_b of the the grain boundary barrier to small values even with a high density of trap states (typically $W < 5$nm and $eV_b < 400$ meV, see 2.1.3). These small values of W allow an important current path via tunnelling through the potential barriers and thus more stable films.

The degradation the LPCVD ZnO:B layer exposed to water vapor implies that thin film silicon modules using these LPCVD ZnO:B layers as TCO should be encapsulated properly to avoid water vapor exposure. It has already been demonstrated by Oerlikon Solar [Kroll 2006] that properly encapsulated 1.4 m^2 amorphous single junction modules using LPCVD ZnO:B layers as back contacts successfully pass the international standard IEC damp-heat test.

6.3 Conclusions

We discuss the electrical characteristics of LPCVD ZnO layers in this chapter. The conductivity of the films depends on two main parameters : the mobility and the carrier density. We show that the doping of the film mainly governs the carrier density.

The double Schottky barrier model with two transport paths : thermionic emission over the barrier and tunneling through the barrier, introduced in chapter 2 for describing the grain boundary electrical behavior applies with good agreement to the experimental results.

We show that more complex mechanisms, that also depend on the carrier density, influence the Hall mobility. For films with low carrier density $N <$ 1 10^{20}cm^{-3}, the grain boundary scattering is the main limitation of the electron mobility. For heavily doped films $N >$ 1 10^{20}cm^{-3}, the bulk scattering governs the mobility.

The LPCVD ZnO:B is sensible to damp heat exposure. In fact, the resistivity increases with the damp heat exposure duration. We interpret this observation by an increase in the trap state density at grain boundary. We obtain more stable films when having high carrier density, because of an enhanced tunneling trough the potential barriers at grain boundary even if the trap density increases.

CHAPTER 7 *Integration of LPCVD ZnO:B films in thin film silicon solar cells*

The present chapter presents the effects of the LPCVD ZnO:B layers incorporated as electrodes in thin film silicon solar cells. These layers are used in amorphous (aSi:H), microcrystalline (μcSi:H), and micromorph tandem solar cells (aSi:H/μcSi:H).

First, we consider the light trapping enhancement induced by the roughness of LPCVD ZnO:B layers in μcSi:H cells. Then, we discuss the solar cell shunt issues that occur depending on the front deposition conditions. Finally we summarize the results of the best solar cells made with LPCVD ZnO:B as front and back contacts.

7.1 Light trapping in μcSi:H solar cells

As grown rough LPCVD ZnO:B films have a high capability to scatter the light at the TCO-cell interface. This aspect is especially important for thin-film solar cells in order to increase the effective absorption of light within the active layer of the cell. Chapter 5.2 discusses the main light scattering parameters of LPCVD ZnO:B layer : the haze factor and the angular distribution function. This section presents the short-circuit current improvement obtained with the implementation of rough front LPCVD ZnO:B layers in μcSi:H solar cells.

Experimental results

A series of seven different LPCVD ZnO:B layers is deposited with a gas phase doping ratio $[B_2H_6]/[DEZ]$ varying from 0 (undoped ZnO) to 2 (heavily doped ZnO). The thickness of each layer is adapted by changing the deposition time in order to achieve a square resistance of 10 Ω_{sq}, which is high enough for good lateral conduction in μcSi:H solar cells. In order to simplify their denomination, we name the samples with their respective gas phase doping ratio $[B_2H_6]/[DEZ]$ values.

Table 7.1 *The optical and electrical characteristics of the LPCVD ZnO:B samples series tested as front TCO.*

$[B_2H_6]$/ [DEZ]	d (μm)	$R_\square$ ($\Omega_\square$)	ρ ($\times 10^{-3}$ Ωcm)	μ_{Hall} ($cm^2V^{-1}s^{-1}$)	N_{Hall} ($\times 10^{19}$ cm^{-3})	σ_{rms} (nm)	Haze factor @600nm (%)	Transmittance @1000nm (%)
0	6.3	10.7	5	42	3	226	96	75
0.1	4	10.2	4	43	3.7		84	80
0.3	2.4	9.8	2.5	39	6.8	109	69	82
0.6	2	10.6	2	37	8	86	38	84
0.9	1.4	10	1.5	24	17	60	11	84
1.2	1.2	10.2	1.6	14	26		6	82
2	1	12.5	1.1	14	39	30	2	77

This series of LPCVD ZnO:B layers has thicknesses varying from 1 μm (for the heavily doped sample) to 6.3 μm (for the undoped sample). These differences in thickness lead to surface roughness from less than 60 nm to 226 nm, respectively (see chapter 4.2.2 for an explanation of the roughness dependency on the film thickness), and thus a haze factor at 600 nm varying from 2 % to 96 %, respectively. The series of LPCVD ZnO:B layers use here is similar to the one describe in section 5.2. See 5.2 for a complete description of the optical properties ($H=f(\lambda)$, $A=f(\lambda)$) of this series of samples.

Table 7.1 summarizes the optical and electrical characteristics of the seven different LPCVD ZnO:B layers used as front TCO in this study.

We deposit microcrystalline silicon pin solar cells on the seven different LPCVD ZnO:B front contacts described previously. We carry out four runs of cell deposition. μSi:H cells are deposited on four different ZnO layers in one run. Therefore, the same type of front contact has been tested in several cell deposition runs.

Thickness of μc-Si:H i-layers is approximately 2 μm. After the silicon deposition, we pattern out of the whole substrate sub-cells with a surface of approximately 1/3 cm^2. We use a LPCVD ZnO:B layer optimized for aSi:H cell (see 4.1.3) as back electrode without any back reflector.

We measure the external quantum efficiencies EQE of the cells (see 3.4.3) under a bias voltage of -1 V in order to achieved a good collection of the charge carriers. Figure 7.1 shows the EQE measured for μc-Si:H cells deposited on five different front LPCVD ZnO:B layers. We observe an increase of the EQE over the whole spectrum as the $[B_2H_6]$/[DEZ] ratio decreases. The EQE increase is larger in the IR and NIR range.

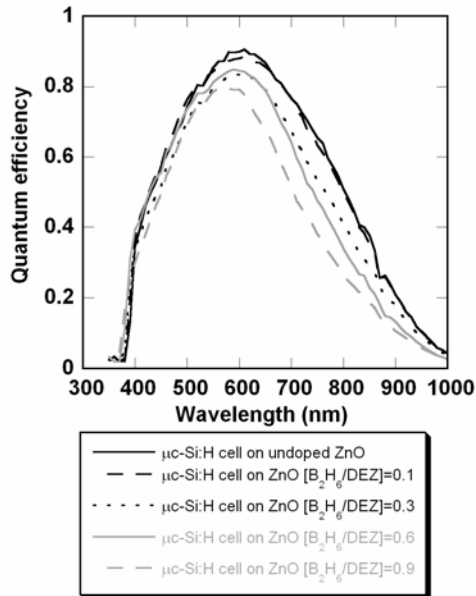

Figure 7.1 *The external quantum efficiency EQE of microcrystalline silicon solar cells deposited on five different front TCO's of the LPCVD ZnO:B series.*

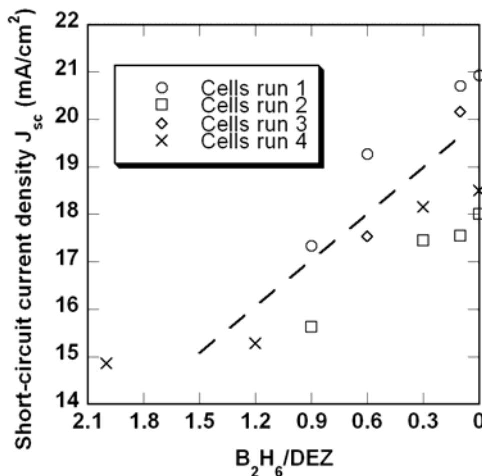

Figure 7.2 *The short-circuit current density photo-generated within 2 μm microcrystalline silicon solar cells deposited on the LPCVD ZnO:B series of substrates, represented in function of the gas phase doping ratio [B2H6]/[DEZ] used during the ZnO layers deposition. No back reflector is incorporated.*

The short-circuit current density J_{sc} was evaluated from the measured external quantum efficiency data and the AM1.5G solar spectrum. Figure 7.2 gives *Jsc* obtained for µc-Si:H cells versus the $[B_2H_6]/[DEZ]$ ratio used for the front LPCVD ZnO:B layer deposition. A continuous increase of *Jsc* from 15 to 21 $mAcm^{-2}$ with the decreasing $[B_2H_6]/[DEZ]$ ratio is observed. These current values are modest due to the absence of white dielectric back reflectors and to the non optimal µcSi:H cell properties. See section 7.3 for results on optimized cells.

The efficiencies of the cells measured under AM1.5 (see 3.4.2) as a function of the different ZnO are between 5 and 6.5 %. The open circuit voltage *Voc* and fill factor *FF* are relatively low for these series of cells. In fact the cell deposition parameters are not optimum here, however the tendencies discussed for the current are valid.

Discussion

We can explain the increase in current density with the $[B_2H_6]/[DEZ]$ ratio of LPCVD ZnO:B films of the series of front TCO by various effects. We discuss these effects below in regard to the wavelength range where they are active.

♦ In the total spectral range of interest ($380 < \lambda < 1000$ nm), a reduction of the reflection at the p/TCO interface take place. This anti-reflection effect come from the sub wavelength features of the rough interface that produce a graded index of refraction [Lechner 2004]. This effect induce a relative reflection reduction of 10~20 % compared to a flat interface [Hagemann 2008].

We need further investigation to quantify difference in reflectance due to this effect in our series of samples. In this case, even the heavily doped sample has a high roughness (σ_{RMS} = 30nm), and this effect takes place [Hagemann 2008]. Therefore, we consider that the reflection changes only slightly in this series of samples.

♦ In the red and infrared range ($550 < \lambda < 1000$ nm), the increase of the current density is attributed to two effects :

- Firstly, a lower free carrier absorption in layers with low $[B_2H_6]/[DEZ]$ ratio (see 5.1).
- Secondly, a higher light scattering effect in samples with front ZnO with low $[B_2H_6]/[DEZ]$ ratio because of their higher surface roughness [Krc 2003].

EQE between cells deposited on undoped ZnO layers (i.e. $[B_2H_6]/[DEZ] = 0$) and lightly doped layers (i.e. $[B_2H_6]/[DEZ] = 0.1$) does not show significant differences, although these layers have different haze factors. The residual free carrier absorption is very low and its variation can be

Table 7.2 *The parameters used to simulate the LPCVD ZnO:B sample series tested as front TCO and the variation of p-Si layer thickness used to obtain figure 7.4.*

$[B_2H_6]$ / [DEZ]	d (µm)	σ_{rms} (nm)	ADF	EMA ratio of mixed index [ZnO - Si]	α_{ZnO} @ 550nm (cm^{-1})	p-Si layer thickness (nm)
0	6.3	230	ADF_{ZnO} optimized for aSi:H	[2/5-3/5]	50	25
0.1	4	190	ADF_{ZnO} optimized for aSi:H	[2/5-3/5]	60	27
0.3	2.4	80	ADF_{ZnO} optimized for aSi:H	[2/5-3/5]	80	32
0.6	2	65	ADF_{ZnO} optimized for aSi:H	[2/5-3/5]	90	36
0.9	1.4	40	ADF_{ZnO} optimized for aSi:H	[2/5-3/5]	160	40

neglected for these two samples. This means that further increase of the thickness after a threshold value is of no further use to improve the current density for a given photoactive thickness. This effect is explained by the fact that despite of the increasing haze factor, the light is no longer scattered in large angles for surface morphology exhibiting large surface features (see 5.2) as it is the case for the 6.3 µm-thick undoped ZnO layers. This losses of light scattered at large angles explain the stagnation of the current density despite the increasing haze factor.

♦ In the "blue" spectral range ($380 < \lambda < 550$ nm), the EQE increases with the decrease of the ZnO layers doping level. We relate this effect to a change in the optical absorption of the silicon p layer :

- Firstly, a variation in thickness of the p layer due to change in the effective surface of the TCO/p interface.
- Secondly, a different optical path length in the p layer induced by different scattering angles [Krc 2003].

In order to verify these assumptions, optical modeling of the experiment are made for comparison.

We use a Monte Carlo simulation program [Springer 2002] to calculate the optical behavior of solar cells structure. The simulated structure is : glass / front ZnO / EMA /p-Si / i-Si / n-Si / back ZnO / air.

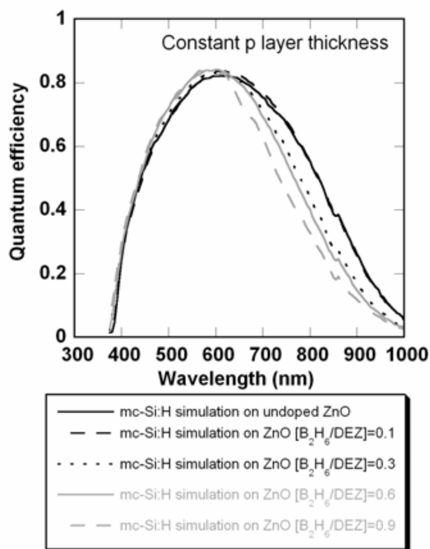

Figure 7.3 *The simulated external quantum efficiency curves of μc-Si:H solar cells with a 2 μm thick i layer deposited on five different front TCO of the LPCVD ZnO:B series of substrate. The silicon p layer thickness is constant set to 30 nm.*

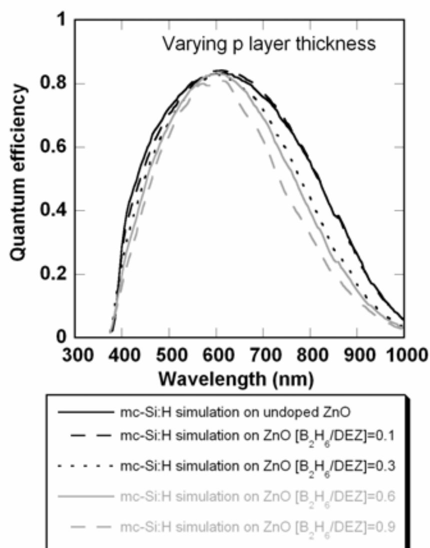

Figure 7.4 *The simulated quantum efficiency of 2 μm-thick i layer microcrystalline silicon solar cell on five different front TCO of the LPCVD ZnO:B series of substrate. The silicon p layer thickness changes from 40 nm on flat highly doped ZnO to 25 nm on rough undoped ZnO.*

The front ZnO is simulated using experimentally determined wavelength-dependent optical coefficients *n* and *k* extracted from transmittance and reflectance measurements (see 3.2.1). We use experimental thickness and experimental or extrapolated σ_{RMS}. The σ_{RMS} value is used for the calculation of the diffuse transmittance using scalar scattering theory (see 5.2). A layer model the decreases in reflection compared to flat interface at the front ZnO / p-Si interface by mixing 2/5 of n_{ZnO} and 3/5 of n_{Si} (effective media approximation EMA). It is important to note that the angular distribution functions of the interfaces are kept identical for all the samples. The angular distribution function chosen is an experimentally determined polynomial function that corresponds to the ADF of a LPCVD ZnO optimized for aSi:H cells.

Table 7.2 shows the parameter used in the simulation for the various front ZnO.

We use experimentally determined wavelength-dependent complex refractive indexes given by Poruba [Poruba 2000] as parameters for simulating the optical characteristics of the silicon layers. The thickness of i-Si and n-Si layers are set to 2 µm and 20 nm, respectively. We assume that the morphologies of the interfaces within the full pin solar cell are conformal copies of the roughness of the front ZnO layer.

Simulated EQE curves are obtained by assuming an ideal extraction of charge carriers from the i layer. The photon absorbed in the p and n layers do not contribute to the current.

Fig 7.3 shows simulated EQE curves of µcSi:H solar cells (2 µm thick i layer) deposited on five different front LPCVD ZnO:B of the series of substrates. The silicon p layer thickness is constant, set to 30 nm.

Fig 7.4 shows simulated EQE curves obtained with the same model parameters as the simulations described previously except that the silicon p layer thickness is gradually lowered from 40 nm for flat highly doped front ZnO to 25 nm for rough undoped front ZnO (see table 7.2).

Simulations are able to reproduce the EQE enhancement in the red and NIR range, and confirm an improved photogeneration potential of thick, highly rough, lightly doped ZnO layers.

EQE simulated with a constant 30 nm p-layer thickness did not show any differences in the blue range. This modelization is in disagreement with the experimental curves. We obtain better agreement by adapting the p layers thickness in the simulated structure from 40 nm for flat highly doped ZnO, to 25 nm for rough undoped ZnO.

This reduction of the simulated p layer thickness, necessary for a good agreement between the experimental and simulated data, is very important (-62 %). The increase of the effective surface of the series of front ZnO measured by AFM is about 33%. Therefore, we cannot expect such a big different in the p layer thickness of the experimental cells due to an increase of the effective surface of the front TCO.

We can explain the additional absorption in the p layer for heavily doped ZnO sample by differences in the angular distribution function of the series of ZnO samples. In chapter 5.2 we demonstrate that sample with large surface features (here the lightly doped sample) scattered light more near the specular direction. Therefore, the optical path length in the p layer is reduced compared to the sample with small surface features (here the heavily doped sample) [Krc 2003].

The efficiency of the cells only slightly increases with the series of front LPCVD ZnO:B contacts despite the increase of J_{sc}. This is due to low *FF* and V_{oc} values induced by shunt and poor microcrystalline cell quality, due to by the morphology of the front LPCVD ZnO:B layer. We discuss these effects in the next section (see also [Python 2008, Bailat 2006]).

7.2 Front contact induced shunt issues

An important cause of low V_{oc} and *FF* in silicon solar cells is shunts. Basically shunts are short circuits between the front and the back contacts of a cell. Short circuit can be induced by particles or by the morphology of the front contact. This section first presents characterization results of shunts due to particles. Then we discuss the link between the morphology of the front contact and the presence of shunts in thin film silicon solar cells. Finally, we present the work of Bailat [Bailat 2002, Bailat 2006] that introduces a plasma treatment of the front LPCVD ZnO:B, which improves the performance of thin film silicon solar cell grown on LPCVD ZnO:B layers.

7.2.1 Particles and its influence on shunting behaviors

Experimental results

28 aSi:H pin solar cells are deposited on a front LPCVD ZnO designed for aSi:H solar cells (see 4.1.3). We measure the V_{oc} at low illumination with a multimeter under a light box (0.1sun). We take lockin thermography pictures of each cell under a reverse bias of 0.3V (see 3.4.4).

The left part of figure 7.5 shows the lockin thermography pictures of 28 aSi:H pin solar cells tested. The white points on the thermography lockin pictures correspond to the location where an increase of the temperature

occurs. In parallel, on the right side, the value of the Voc measured at low illumination is given.

Figures 7.6 and 7.7 show complete analysis of shunts due to particles on aSi:H cells deposited on a front LPCVD ZnO:B designed for aSi:H solar cells (see 4.1.3). We localize and mark the shunts with the help of the lockin thermography and an optical microscope, then we perform SEM analysis of the surface and cross-sections obtained by FIB cutting of the nearest surface anomaly. Appendix A presents additional samples that have undergone the same analysis.

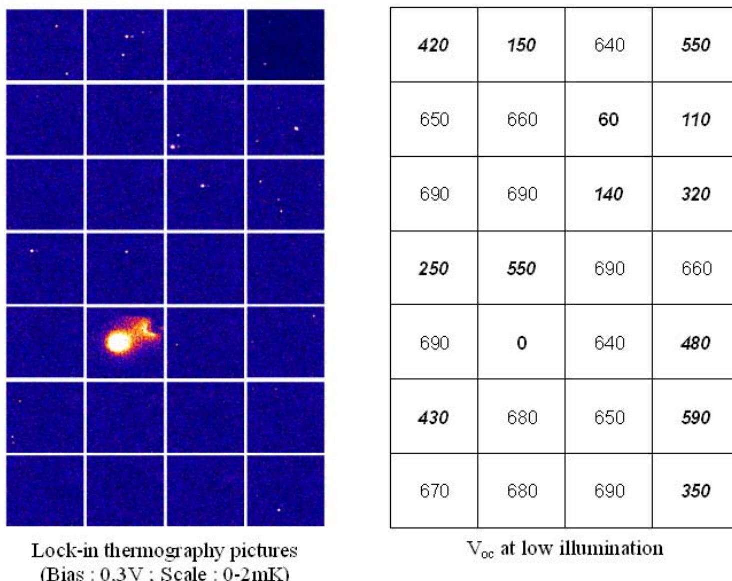

420	150	640	550
650	660	60	110
690	690	140	320
250	550	690	660
690	0	640	480
430	680	650	590
670	680	690	350

Figure 7.5 *The lockin thermography picture and V_{oc} at low illumination (0.1sun) of 28 aSi:H cells.*

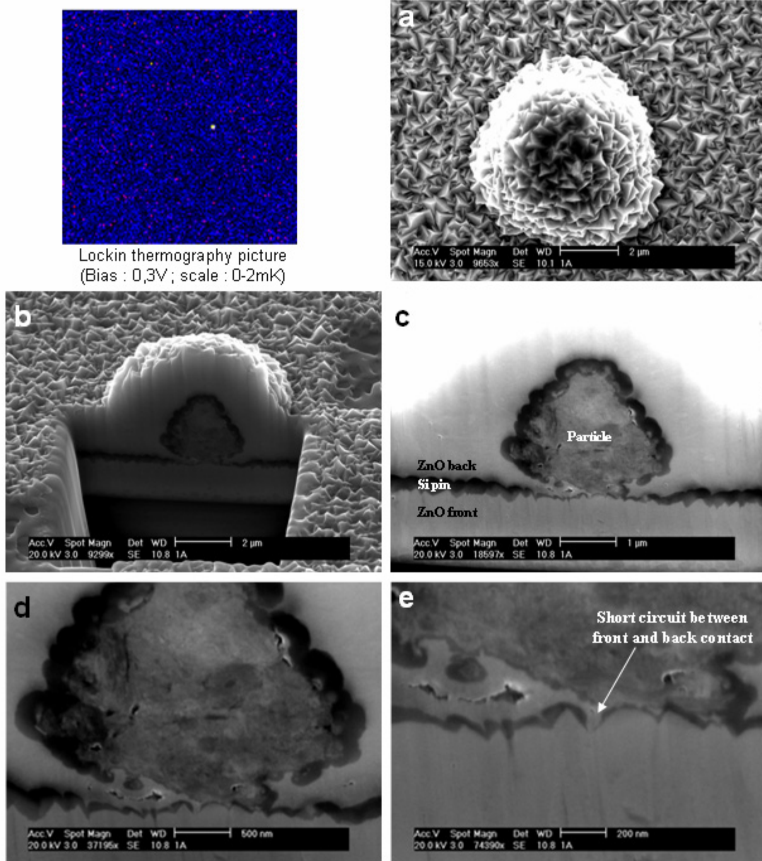

Figure 7.6 *Lockin thermography picture, SEM micrograph of the surface (a), and SEM micrographs of the cross section obtained by FIB (b,c,d,e) of a surface anomaly located at a thermography hot spot in an aSi:H cell.*

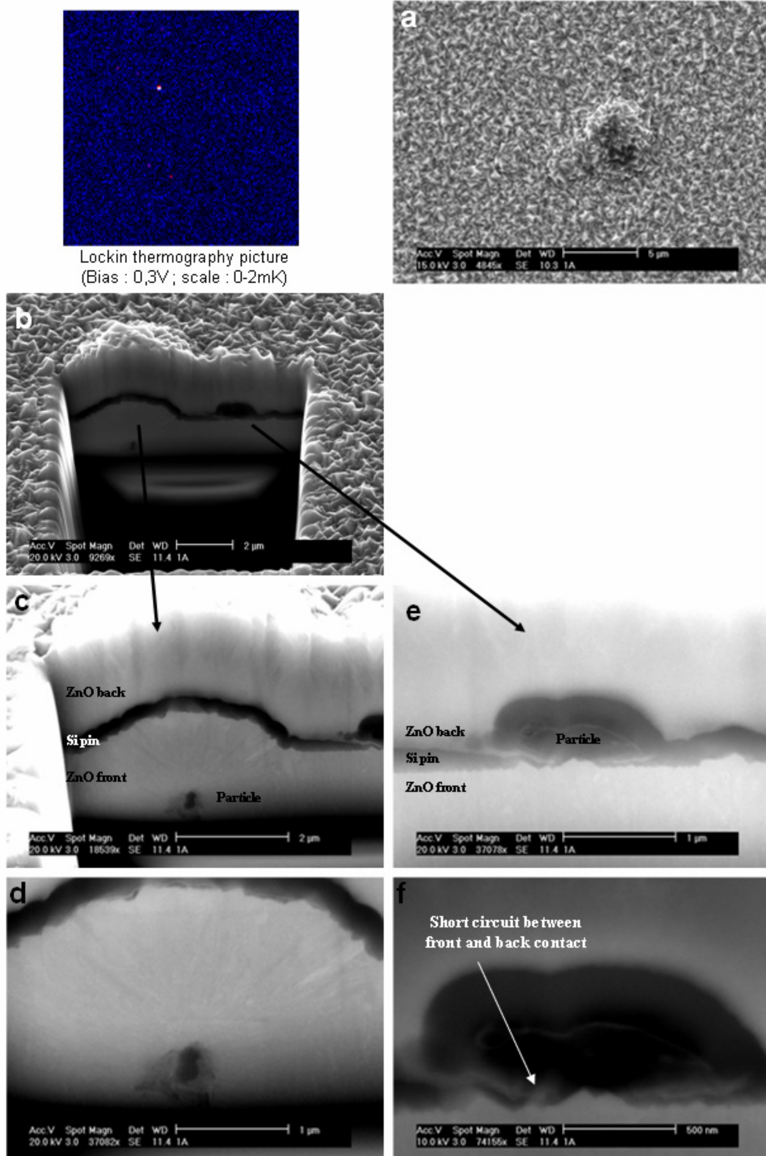

Figure 7.7 *Lockin thermography picture, SEM micrograph of the surface (a), and SEM micrographs of the cross section obtained by FIB (b,c,d,e,f) of a surface anomaly located at a thermography hot spot in an aSi:H cell.*

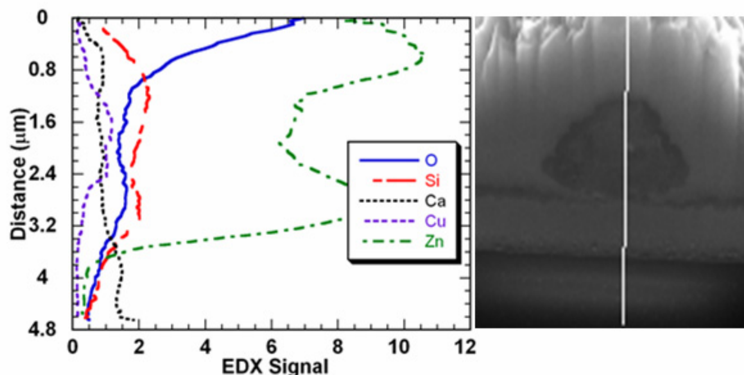

Figure 7.8 *The EDX profile (following the white line) of a surface anomaly located near a thermography hot spot and obtained by FIB cross-cutting in an aSi:H cell .*

Figure 7.8 is an EDX profile of the cross section of a surface anomaly (localized as describe in the previous paragraph). We observe a slight increase of the Cu and the Si lines when crossing the particle.

Discussion

We give evidence of a clear correlation between the V_{oc} value at low illumination and the lockin thermography hot spots in figure 7.5. The cells showing a hot spot usually also exhibit V_{oc} under 600 mV. The hot spots shown on the lockin thermography picture as well as a low V_{oc} are the signature of localized shunt.

If during the handling of the TCO-coated glass a foreign particle falls on the substrate, the subsequent deposition of the Si-based layer and back contact easily form shunted devices, as identified on figures 7.10 and 7.7e/f.

Particles present on glass do not induce short circuit. Figure 7.7c/d shows an example of a particle located on the glass. The complete cells, including front and back contacts, are deposited on the particle, which creates a bump on the surface. However, no evidence of short circuit shunt is observed in these cases because all the layers are deposited with good conformity over the particle.

The EDX analysis, such as presented on figure 7.8, does not allow a definitive identification the composition of the particle. EDX does not possess enough spatial sensitivity for such cross sections. However, an increase of the copper line is likely observed in the EDX scan. There are several possible sources of particles. Glass cutting, dust from the operator as well as the substrate environments are all possible sources of particles.

The deposition reactors (LPCVD, PECVD) can also produce particles. A close control of the environment as well as the deposition system is necessary to reduce particle induced shunts. As particles present on the front ZnO are particularly destructive for the cells, we could envisage cleaning the front substrate (as it is performed after the laser scribing in module production) in order to get rid off the problem. Mechanical, high pressure gas flow or wet cleaning are all possible solutions.

However, we cannot prove a perfect correlation with a particle presence for all shunts located by lockin thermography and low illumination V_{oc}. Some runs of cells present shunting behavior despite of a perfectly clean substrate and the absence of any particles. In these cases, other effects such as the front TCO morphology cause losses in V_{oc} and FF. We discuss these effects in the next section.

Conclusions

In this section, we demonstrated that lockin thermography is a powerful characterization tool to localized shunts due to particles. The presence of particles on the glass substrate does not systematically induce shunts, contrary to the presence of particles on the front TCO.

7.2.2 Morphology and its influences on shunting behavior

Experimental results

We deposit a temperature series of LPCVD ZnO:B. We vary the deposition temperature from 149°C to 175°C. We adapt the thickness of each sample in order to get the same roughness σ_{RMS}. We name the different ZnO substrates of the series according to their deposition temperature values.

Figure 7.10 shows SEM and AFM pictures of the samples. The varying deposition temperature induces different types of morphologies. Samples deposited at high temperature exhibit sharp, well designed pyramids, in contrast to samples deposited at low temperature that show a more random texture made of either small or large pyramidal features.

To obtain statistical data, we pattern a set of 200 1 cm^2 aSi:H cells codeposited on each front ZnO of the series. We measure the V_{oc} of the cells under low illumination. We qualify cells with a low illumination V_{oc} value below 100 mV as shunted. We consider cells with a low illumination V_{oc} between 100 mV and 600 mV as "bad", and cells with a low illumination V_{oc} higher than 600 mV as "good cells". In this case, the lockin thermography does not indicate the presence of localized shunts.

Figure 7.9 shows the percentage of shunted and good cells as a function of the front ZnO deposition temperature. The percentage of good cells increases as the deposition temperature decreases. The maximum number

of good cells is obtained at 150°C, which correspond to the random pyramid size features. At higher temperature, the number of bad cells increases. At 170°C all the cells are completely shunted.

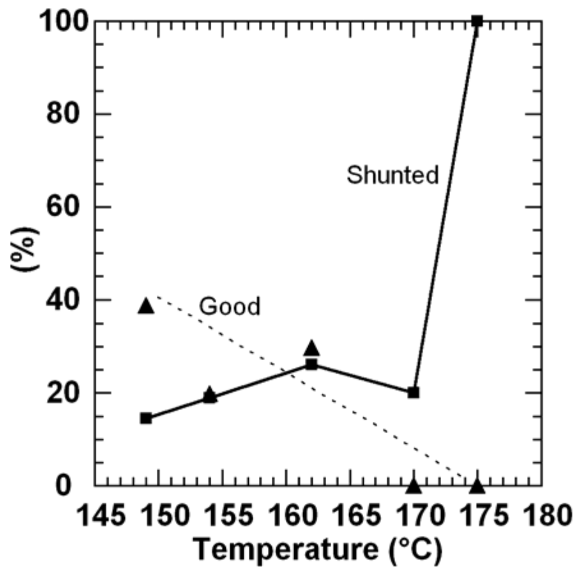

Figure 7.9 *The percentage of shunted, bad and good amorphous cells as a function of the front ZnO deposition temperature. Statistics made on 200 cells.*

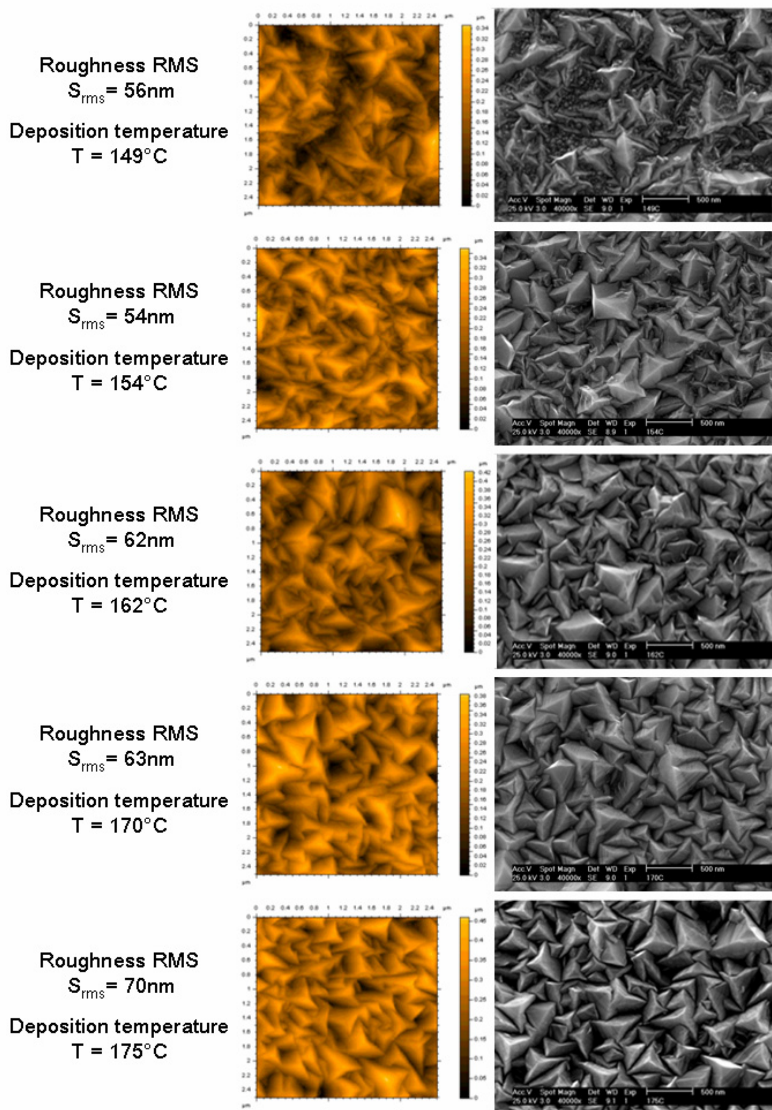

Figure 7.10 *The AFM and the SEM pictures of front ZnO deposited at different temperatures. The thickness of each film has been adapted to achieve the same roughness.*

Discussion

The surface morphology of the front TCO plays a role in the cell's quality. The sharp valley present on layers deposited at high temperature lead to the formation of voids and cracks in the silicon cells [Python 2008, Bailat 2006, Löffler 2005]. These voids induce leak in the current between front and back contacts, i.e. a shunting behavior. We assume that critical features (e.g. too sharp valley) occur with a different rate of recurrence for the different LPCVD regime and are likely not uniformly distributed on the substrate.

For front ZnO deposited at low temperature, the valley are not as sharp as ZnO deposited at high temperature, leading to substrates with less critical features, on which it is more easy to grow silicon solar cells with good performances.

The experiments described here are achieved on amorphous cells, but microcrystalline cells are even more sensitive to the morphology [Python 2008, Bailat 2006]. In fact, in order to achieve high current density, microcrystalline cells need a high surface roughness in order to enhance light trapping. This high roughness, in addition to tough surface features, makes microcrystalline very sensitive to the front TCO morphology.

Strong interdependence exists between the front contact surface texture and the subsequent silicon solar cell growth on it. It is therefore crucial to develop the front contact and the solar cell PECVD process together. In fact, the solar cells deposition processes can vary in their sensitivity to the morphology of the front TCO. Recent results show that high yield and high current can be achieved on rough LPCVD ZnO:B layers using improved silicon PECVD process [Meier 2008, Benagli 2008, Benagli 2007].

7.2.3 Plasma surface treatments

Paragraph 7.2.1 and 7.2.2 describe the difficulties that can occur when growing aSi:H cells on LPCVD ZnO:B layers. In fact, due to presence of particles and the sharp surface morphology of the front ZnO layer, obtaining high values of solar cell open circuit voltages and fill factors is sometimes difficult. This section presents a plasma treatment introduced by Bailat [Bailat 2006] on the surface of the LPCVD ZnO:B layer developed in this study, that improved the performance of silicon solar cells grown on it.

An Ar plasma treatment is applied to the front ZnO layer. This surface treatment profoundly modifies the morphology of the ZnO surface (figure 7.11). The surface becomes slightly smoother with a decrease of σ_{RMS} from approximately 200 nm (without treatment) to 175 nm and 150 nm after surface treatments of 40’ and 80’ duration, respectively.

The sharp edges of the larger pyramids remain visible after the treatment, forming a network of salient and curved lines at the surface. However, the sides of the pyramids that are initially flat appeared to have been hollowed by the treatment. This is the reason why the V-shaped valleys seen in figure 7.11a turn into U-shaped valleys in figure 7.11b [Bailat 2006].

The efficiency of the μcSi:H solar cells subsequently grown on these substrates, increased from 3.3 to 9.2% after 40' of surface treatment. Further optimization of the solar cell deposition parameters led us to μcSi:H cells with conversion efficiencies as high as 9.9% [Bailat 2006].

Authors mentioned that cracks and voids have often been observed in μc-Si:H [Python 2008, Bailat 2006, Bailat 2002] and aSi:H [Löffler 2005] solar cells grown on rough substrate. These cracks usually arise from the tip of the V-shaped valleys within the i-Si layer. Investigations by transmission electron microscopy (TEM) on similar samples to the one treated 80' showed that cracks and voids are no longer observed when the valleys have a U-shape, i.e. after the plasma treatment. The absence of cracks during the subsequent deposition of the μcSi:H layers may be caused by the TCO surface having a different shading effect on the impinging silicon precursors. This depends on the TCO's surface morphology. The presence of cracks is associated with poor carrier collection. Carrier collection immediately improves with the surface treatment [Bailat 2006]. However, as the treatment reduces the short circuit current due to lower light scattering capability of the treated surface morphology, a compromise between the V_{oc}, FF and I_{sc} has to be found in order to produce the best solar cell.

Further improvement has to be carried out in order to reduce the treatment time. For instance, changing the composition of the plasma by adding methane may increase the etching speed [Ip 2002]. Wet etching with acid could also lead to promising surface features.

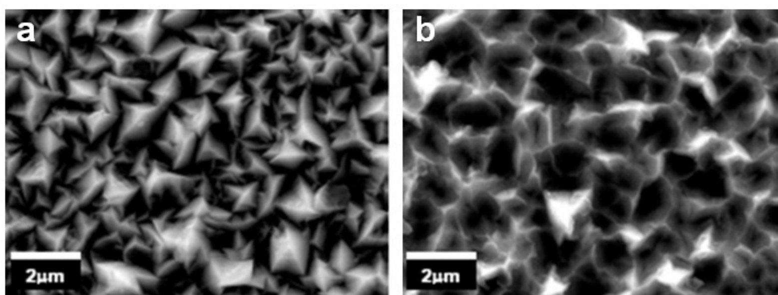

Figure 7.11 *SEM micrographs of surface morphologies of front ZnO before and after 80' plasma treatment.*

7.3 High current and best solar cell results

Thin film silicon solar cells have been studied and optimized at the IMT for more than 10 years. This long-term work is published in numerous papers, see for instance [Dominé 2008, Shah 2006, Bailat 2006, Steinhauser 2005, Meier 2003, Shah 1999].

Table 7.3 summarizes the best solar cells results obtained at the IMT with LPCVD ZnO:B used as front and back TCO. Please see reference for the exact experimental details.

These results show that LPCVD ZnO:B layers are well suited in order to achieve high performance thin film silicon solar cells.

The best pin aSi:H cell obtained on LPCVD ZnO:B with an antireflection (AR) coating on glass has an efficiency of η = 9.5 % with FF = 63 %, V_{oc} =860 mV and J_{sc} = 17.5 $mAcm^{-2}$ [Meier 2003].

Table 7.3 *The electrical characteristics of thin film silicon solar cells obtained at IMT with LPCVD ZnO:B used as front and back TCO.*

Solar Cell	Front TCO	Back TCO	Jsc ($mAcm^{-2}$)	FF (%)	Voc (V)	η (%)	ref
aSi:H pin stabilized, with AR glass	LPCVD ZnO 1.9µm	LPCVD ZnO 1.9µm + white paint	17.5	63	0.86	9.5	[Meier 2003]
µSi:H pin without AR glass	LPCVD ZnO 4.1µm plasma treated	LPCVD ZnO 1.9µm + white paint	24.7	74.1	0.54	9.9	[Bailat 2006]
micromorph aSi:H pin/µSi:H pin stabilized, without AR glass	LPCVD ZnO 4.8µm plasma treated	LPCVD ZnO 1.9µm + white paint	12.5	67.2	1.32	11.1	[Dominé 2008]
micromorph aSi:H pin/µSi:H pin initial, with AR glass	LPCVD ZnO 4.8µm plasma treated	LPCVD ZnO 1.9µm + white paint	13.8	70.8	1.36	13.3	[Dominé 2008]

The best pin μcSi:H solar cell obtained so far on the plasma treated LPCVD ZnO:B has a 1.6μm thick i layer and reached an efficiency of η = 9.9 % with FF = 74.1 %, V_{oc} = 545 mV and J_{sc} = 24.7 mAcm^{-2} [Bailat 2006]. High current up to 26.25 mAcm^{-2} are obtain in reverse bias for 2.5μm thick pin μcSi:H solar cell without AR coating on glass [Ballif 2006].

The best stabilized micromorph cell is deposited on plasma treated LPCVD ZnO:B without AR coating on glass and yield η = 11.1 % with FF = 67.2 %, V_{oc} = 1.32 V and J_{sc} = 12.5 mAcm^{-2} [dominé 2008]. The thickness of the top and the bottom cell are 300 nm and 3 μm, respectively. Initial efficiency of η = 13.3 % is reported for a aSi:H/μcSiH deposited on plasma treated LPCVD ZnO:B with an AR coating on glass and a 3.5 μm thick bottom cell. This cell shows a remarkable sum of the J_{sc} of the component cells equal to 27.7 mAcm^{-2} [dominé 2008].

These efficiencies and current densities compares very well with the best results of other groups that work with other front TCO (e.g. sputtered and etch ZnO) [Finger 2008, Schropp 2007, Matsui 2006, Rech 2005].

These results demonstrate the versatility of the LPCVD ZnO:B process, which is used to achieve front and back TCO for aSi:H, μcSi:H and aSi:H/μcSi:H. In fact, for each type of cells the LPCVD ZnO:B layer can be adapted in order to achieve the specific requirement needed.

7.4 Conclusions

We demonstrate that rough ZnO layers can be successfully implemented in thin film silicon solar cells. High current density in μcSi:H and aSi:H/μcSi:H solar cells is achieved with thick, large grain, high mobility, low absorption LPCVD ZnO:B films as front TCO.

We identify the important role of the particles and the morphology of the front TCO in shunts issues in thin film solar cells. In order to achieve high value of V_{oc} and FF, it is important to avoid any dust on the front TCO.

The surface morphology of the front TCO also plays a crucial role for the cells quality. Valley that are too sharp induce low V_{oc} in the cell. Therefore, an adapted deposition temperature of the LPCVD ZnO:B has to chosen in order to get a surface morphology well suited for the growth of silicon solar cells.

Finally, we show that applying a Ar plasma surface treatment on the front ZnO greatly improves the electrical parameters of the μcSi:H cells subsequently grown on it.

CHAPTER 8 *Final conclusions*

8.1 Conclusions

The object of the present work was to provide a better understanding of LPCVD ZnO:B and to show its full technical potential as a transparent conductive contact in thin film solar cells.

In this work we study "LPCVD ZnO:B layers, from the deposition process to the final application" and focus especially on their electrical and optical properties.

The LPCVD ZnO:B film studied is a transparent conductive oxide polycrystalline material, made of large columnar grains that typically appear at the surface as large pyramid features. These surface features scatter the light in the subsequently-grown solar cell and thus increase their current density.

The layer properties depend strongly on the deposition parameters. By varying the parameters of the LPCVD process, we can obtain a large range of film transparency and conductivity, as well as a large variety of surface features. In order to maximize solar cell efficiencies, it is important to adapt the TCO film properties to the requirement of the solar cells in which they are used.

In this work, we focus on understanding the physics of the LPCVD ZnO:B film properties in order to efficiently optimize its characteristics to obtain TCO films well suited for thin film solar cell applications.

To achieve a better understanding of the LPCVD ZnO:B film physics, several characterization techniques were used for the first time on our layers:

- ***Raman analysis :***

  We successfully link the increasing intensity of a mode at 580 cm^{-1} measured by Raman spectroscopy with the doping level of LPCVD ZnO:B layers.

- ***Elemental analysis :***

  We measure LPCVD ZnO:B layers with SIMS and RBS techniques. The results provide evidence of the non stoechiometry of LPCVD ZnO:B films and the presence of hydrogen and carbon in the layers.

- ***Solar cell shunt study :***

  We demonstrate that lockin thermography is a powerful characterization tool to localize solar cell shunts due to particles.

We determine and verify theoretical models that describe the optical and electrical properties of LPCVD ZnO:B films:

- ***Optical model for the visible and infrared region of the light spectrum :***

  We show that the Drude model in its simplest form is sufficient to describe the NIR optical behavior of LPCVD ZnO:B films. We attribute the low absorption of LPCVD ZnO:B films that remains in the visible range to residual free carrier absorption also described by the Drude model.

- ***Band gap behavior model :***

  We prove that changing carrier density shifted the value of the band gap energy according to a Burstein-Moss and band gap narrowing law effects. At energies slightly lower than Eg, we observe exponential band tail absorption due to states in the band gap.

- ***Light scattering model :***

  We observed different light scattering behaviors depending on the surface morphology of the LPCVD ZnO:B films. For samples with small surface feature, the haze factor is low, and light scattering occurs at large angles. For samples with large surface features, the haze factor is high, and light is scattered more closely to the specular direction.

- ***Electrical model :***

  We found that the electron mobility is limited by grain boundary scattering at low carrier densities and by bulk scattering at high carrier densities. The transition between these regimes is continuous in the range of doping level achievable in LPCVD ZnO:B films.

We systematically changed the ZnO film properties and evaluated the effect this had on the solar cells deposited on such layers. Considering the results of those measurements, we optimize our front ZnO contact and achieve improved cell performances.

- ***Influence of the light scattering capability on the current in μcSi:H cells :***

  We observe a high improvement in current density of μcSi:H cells, which we attribute to good light trapping and low absorption in highly rough, lightly doped front LPCVD ZnO:B layers.

  We measure a significant improvement of current density with an increasing film thickness due to light trapping and low absorption due to the reduced doping level.

- ***Shunt issues :***

  We show that, in order to achieve high V_{oc} and *FF* values in silicon solar cells, it is important to avoid the presence of dust on the front TCO.

  The surface morphology of the front contact also plays a crucial role in the cell quality. We demonstrate that, when used as a front contact, the overly sharp valley of the LPCVD ZnO:B surface can result in solar cells with low V_{oc} and *FF*. Therefore, we have to choose an adapted deposition regime in order to get a surface morphology well suited to the growth of silicon solar cells.

- ***Development of an optimized TCO for μcSi:H cells and aSI:H/μcSi:H cells :***

  Taking into account all the previous results, we develop a LPCVD ZnO:B layer especially designed for high efficiency μcSi:H and aSi:H/μcSi:H cells. This layer has high light trapping capability. To achieve this, we enlarge the surface features of the LPCVD ZnO layer by increasing the thickness of the film up to 5 μm. Due to the higher film thickness and high mobility, we achieved the required sheet resistance of 10 $\Omega_{\square}$ even with low carrier density. Therefore, the carrier density is set to a minimum, leading to highly transparent films due to low free carrier absorption.

After smoothing the ZnO surface with a plasma treatment introduced by.Bailat [Bailat 2006], we achieved light soaked high efficiency μcSi:H (9.9 %) and aSi:H/μcSi:H cells (11.1%).

8.2 Perspectives

Many interesting topics are left to be studied on LPCVD ZnO:B layers. In the author's opinion the most pressing are:

- Understanding the growth and the nucleation process of LPCVD ZnO:B films : so far, we do not understand the exact growth mechanism. However, this could help improving the properties of the first 300 nm of the layers, which are detrimental to the overall film quality.
- Analyzing the doping mechanisms in LPCVD ZnO:B films. A large amount of boron that is incorporated in the layer is not active as a dopant. It may form clusters and impurities that reduce the electron bulk mobility. Thus, understanding the exact incorporation of dopants in LPCVD ZnO:B layers may help to improve the electrical characteristics of the films.
- Studying the ZnO-silicon interface. The LPCVD ZnO:B surface states influence the growth of the solar cell subsequently deposited on it. Analyzing this influence may help to obtain better TCO-cell contacts and a better nucleation of the silicon, leading to progress in solar cell performances.

Appendix : Shunt analysis

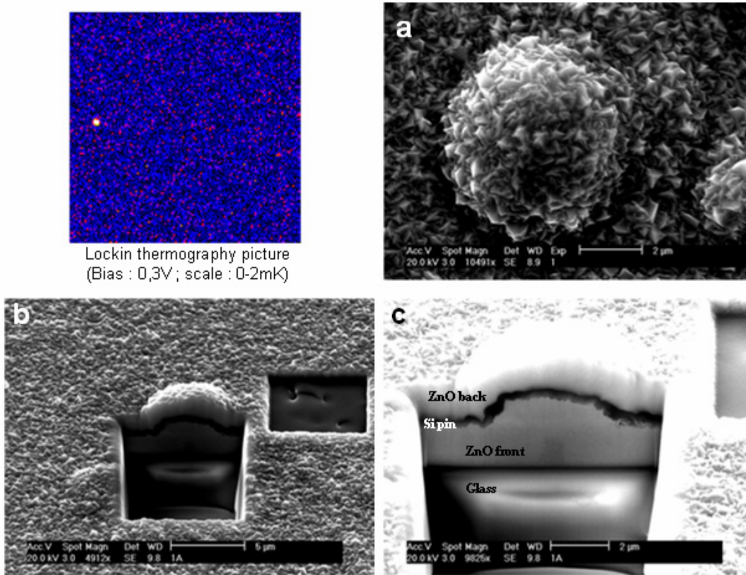

Figure A.1 *The lockin thermography picture, SEM picture of the surface (a), and SEM pictures of the cross section obtained by FIB (b,c) of a surface anomaly located near a thermography hot spot in an amorphous cell.*

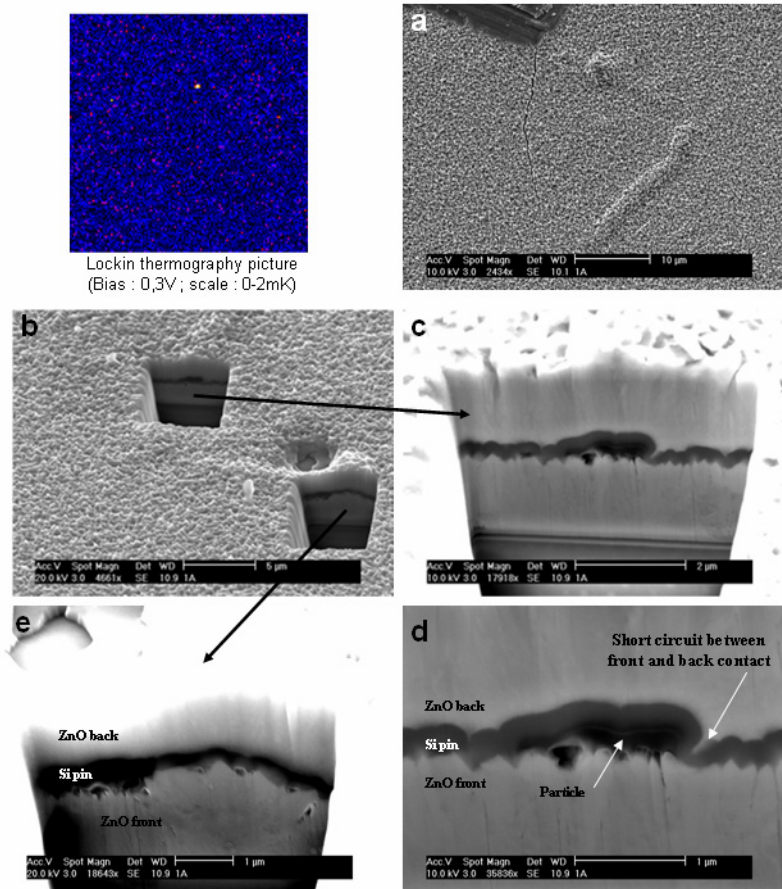

Figure A.2 *The lockin thermography picture, SEM picture of the surface (a), and SEM pictures of the cross section obtained by FIB (b,c,d,e) of a surface anomalies located near a thermography hot spot in an amorphous cell.*

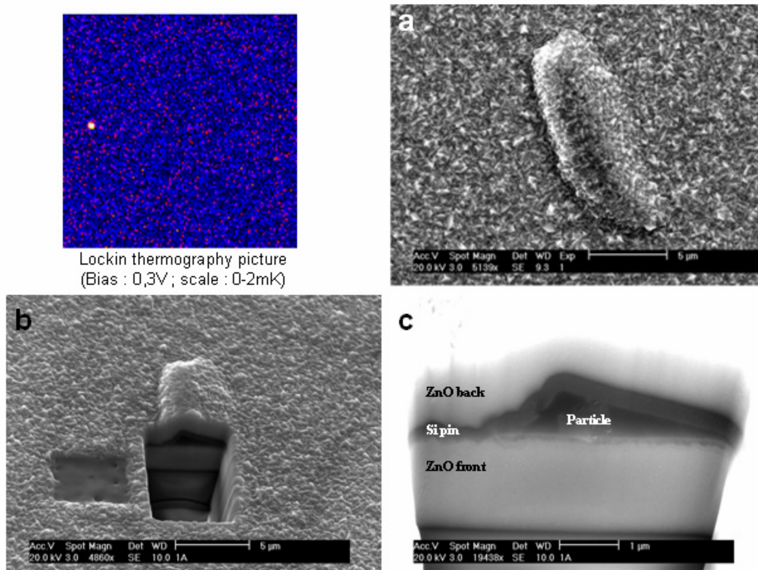

Figure A.3 *The lockin thermography picture, SEM picture of the surface (a), and SEM pictures of the cross section obtained by FIB (b,c) of a surface anomaly located near a thermography hot spot in an amorphous cell.*

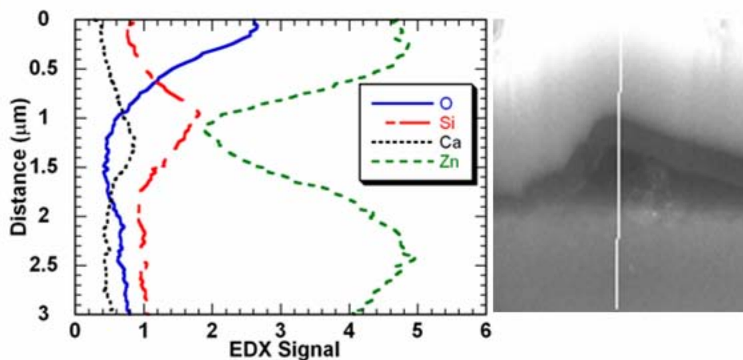

Figure A.4 *The EDX profile (following the white line) of a surface anomaly located near a thermography hot spot in an amorphous cell obtained by FIB cutting .*

Acknowledgments

I would like to thank Pr. Christophe Ballif for giving me the opportunity to accomplish my thesis in the motivating field of photovoltaics in a high level and enthusiastic research group. His scientific inputs and the numerous discussions we had together contributed widely to the achievements of my work.

I thank greatly the referees Dr. Oliver Kluth, Pr. Phillip Aebi, and Pr. Ruud Schropp that they accepted to join the examination board and devoted time to the reading of this thesis.

A special thank goes to my project leader Dr. Sylvie Faÿ, who supervised me during all the duration of this thesis. Her kindness, her availability and her wise advices supported me widely.

I would like to gratefully thank Pr. Arvind Shah and Dr. Diego Fischer to giving me the opportunity to work in the field of thin film silicon solar cells previously from this thesis.

Warm thanks go to all the collaborators of the ZnO group, Romain Schlüchter, Seung Yeop Myong, Nuno Oliveira, Marlène Schwab and Stefan Meier. Their friendship and the numerous scientific discussions we shared together contributed to greatly extend my motivation during this work.

I would like to acknowledge Dr. Evelyne Vallat, Didier Dominé, and Dr. Ricardo Theron for their critical discussions and comments during the writing of this thesis.

I thank Alain Rüfenacht and the team of the Hahn Meitner Institut in Berlin for temperature dependence of the conductivity and Raman measurements. I also thank Pr. Vanacek and the team of Prague University (Institute of Physics, Academy of Sciences of the Czech Republic) for optical characterizations.

I would like to thank all my colleagues and friends at the Institute for their constant help during this work. In particular, Dr. Julien Bailat, Didier Dominé, Peter Bühlmann, Adrian Billet, Dr. Luk Feitknecht, Martin Python, Dr. Andrea Feltrin, and Dr. Fanny Sculati-Meillaud for solar cell depositions and characterizations; Luc Fesquet and Sylvain Dunand for the good atmosphere in our office; Sara Olibet, Thomas Söderström, Grégory Choong, Dr. Nicolas Wyrsch, Xavier Niquille, Franz-Josef Haug, and Dr. Ulrich Kroll for stimulating discussions; Reto Tscharner, Cedric Bucher, Fabrice Jeanneret, Jean-Luc Kumin and Hassan Laaroussi for technical

support; Brigitte Khan, Joelle Benjac, Sandrine Piffaretti and Martial Racine for administration support.

I also would like to thank Laurence Bodenmann for her enthusiasm and her very precious moral support.

Finally, I would like to thank my family for their constant support during all my studies.

References

[Adhikari 2004] S. Adhikaria, S. Kumara, P. Siripuekpongb, Proceedings of the 14th PVSEC, Bangkok, 2004.

[Adachi 1999] S. Adachi, *Optical properties of crystalline and amorphous semiconductor, materials and fundamental principles*, Kluwer academic publishers, 1999.

[Adachi 1999b] S. Adachi, *Optical properties of crystalline and amorphous semiconductor, numerical data and graphical information*, Kluwer academic publishers, 1999.

[Aghamalyan 2003] N. R. Aghamalyan, E. A. Kafadaryan, R. K. Hovsepyan, and S. I. Petrosyan, Semicond. Sci. Technol. **18**, p.525, 2003.

[Aitken 2004] D.W. Aitken, L.L. Billman, S.R. Bull, Renewable energy world, *The climate stabilization challenge*, 2004.

[Aselma 2006] E.A. Alsema, M.J. de Wild-Scholten, V.M. Fthenakis, Proc. of the 21st European Photovoltaic Solar Energy Conference, Dresden, Germany, 2006.

[ASTM 36-1451] American Standard for Testing of Materials (*ASTM*) card N° *36-1451.*

[Bailat 2002] J. Bailat et al. Journal of Non-Crystalline Solids, Vol. 299-302, p. 1219, 2002.

[Bailat 2005] J. Bailat, V. Terrazzoni-Daudrix, J. Guillet, F. Freitas, X. Niquille, A. Shah, C. Ballif, T. Scharf, R. Morf, A. Hansen, D. Fischer, Y. Ziegler, and A. Closset, Proceedings of the 20th European PVSEC, 2005.

[Bailat 2006] J. Bailat, D.Dominé, R. Schlüchter, J. Steinhauser, S. Faÿ, F. Freitas, C. Bucher, L. Feitknecht, X. Niquille, T. Tscharner, A. Shah, C. Ballif, Proc. Of the World PV Conference, 2006.

[Ballif 2006] C. Ballif, J. Bailat, D. Dominé, J. Steinhauser, S. Faÿ, M. Python, L. Feitknecht, Proc. of the 21th European Photovoltaic Solar Energy Conference and Exhibition, Dresden, 2006.

[Bang 2008] J. Bang, K.J. Chang, Applied physics letters **92**, p.132109, 2008.

[Behrendt 2008] M. Behrendt, Proc. of the 23th European Photovoltaic Solar Energy Conference, spain, 2008.

[Benagli 2007] Benagli et al., Proc. of the 22nd EUPVSEC, Italy, 2007.

[Benagli 2008] Benagli et al., Proc. of the 23th EUPVSEC, Spain, 2008.

[Bensmaine 2007] S. Bensmaine et al. Journal of electron devices **5**, p.104, 2007.

[Brendel 2003] R. Brendel, *Thin Film Crystalline Silicon Solar Cells : Physics and Technology*, Wiley, 2003.

[Bubenzer 2003] A. Bubenzer, J. Luther, *Photovoltaics guidebook for decision makers* (Springer) ISBN 3-540-41327-8, 2003.

[Burstein 1954] E. Burnstein, Phys. rev. **93**, p.632, 1954.

[Campa 2007] A. Čampa, J. Krč, J. Malmström, M. Edoff, F. Smole and M. Topič, Thin Solid Films **515**, p.5968 2007.

[Carcia 2003] P.F. Carcia et al., Vac. surf. films **21**, p.745, 2003.

[Carlson 1977] D.E. Carlson, C.R. Wronski, J.I. Pankove, RCA Review 38, p.211, 1977.

[Carlson 2000] D.E. Carlson, G. Lin, G Ganguly, Proc. of 28th IEEE conference, p.707, USA, 2000.

[Catalano 1982] A. Catalano et al., Proc. of 16th IEEE Photovoltaic specialist conference, p.1421, USA, 1982.

[Chae 2007] Y. Chae et al., Proc. of the 22nd European Photovoltaic Solar Energy Conference, Italy, 2007.

[Chatelon 1999] J.P. Chatelon et al., Semicond. Sci. technol. **14**, p. 642, 1999.

[Christoulakis 2005] S. Christoulakis et al.,Rev. adv. Mater. Sci. **10**, p. 331, 2005.

[Chopra 1983] K.L. Chopra, S. Major, and D.K. Pandya, Thin solid Films **102**, p. 1983.

[Dehuff 2005] N.L. Dehuff et al. J. appl. Phys. **97**, p. 64505, 2005.

[Dominé 2008] D. Dominé, P. Buehlmann, J. Bailat, A. Billet, A. Feltrin, and C. Ballif, Proceedings of the EU PVSEC, Valencia, 2008.

[Domingos 2004] H.S. Domingos, J.M. Carlsson, P.D. Bristowe, B. Hellsing, Interface science **12**, p. 227, 2004.

[Dong 2008] Y. Dong et al., Applied physics letters **93**, p. 72111, 2008.

[Drude 1900] P. Drude, Annalen Phys., **1**, p. 566, 1900.

[EAG 2008] Evans analytical group, *RBS application note*, http://www.eaglabs.com/techniques/analytical_techniques/rbs.php, 2008.

[Edwards 2004] P.P. Edwards, A. Porch, M.O. Jones, D.V. Morgan, R.M. Perks, Dalton Trans., p. 2995-3002, 2004.

[Ellmer 2000] K. Ellmer, J. Phys. D : Appl. Phys. **33**, p. R17, 2000.

[Ellmer 2007] K. Ellmer, A. Klein, B. Rech, *Transparent conductive oxide*, Springer, 2007.

[EPIA 2007] European Photovoltaic Industry Association (EPIA), *Solar Generation IV – 2007*, 2007.

[Exarhos 1995] G. Exarhos et al., thin solid films **270**, p.27, 1995.

[Exarhos 2007] G. Exarhos, X. Zhou, Thin solid films **515**, p. 7025-7052, 2007.

[Faÿ 2000] S. Faÿ, S. Dubail, U. Kroll, J. Meier, Y. Ziegler, A. Shah, Proceedings of the 16th EC Photovoltaic Solar Energy Conference, Glasgow, UK, p. 361, 2000.

[Faÿ 2003] S. Faÿ, *L'oxyde de zinc par depot chimique en phase vapeur comme contact électrique transparent et diffuseur de lumière pour les cellules solaires*, EPFL thesis, 2003.

[Faÿ 2005] S. Faÿ, U. Kroll, C. Bucher, E. Vallat-Sauvain, A. Shah, Solar energy material and solar cells **86**, p.385, 2005.

[Faÿ 2005b] S. Faÿ, J. Steinhauser, R. Schlüchter, L. Feitknecht, C. Ballif, A. Shah, Proceedings of the 15th International Photovoltaic Science and Engineering Conference, Shanghai, China, **1**, p. 559, 2005.

[Faÿ 2006] S. Faÿ, L. Feitknecht, R. Schlüchter, U. Kroll, E. Vallat-Sauvain, A. Shah Solar energy material and solar cells, Proc. **90**, p. 2960, 2006.

[Freeman 2000] A.J. Freeman, K.R. Poeppelmeier, T.O. Mason, R.P.H. Chang, and T.J. Marks, MRS Bulletin, p.45-51, 2000.

[Finger 2008] F. Finger, Y. Mai, S. Klein, R. Carius, Thin Solid Films **516**, p. 728, 2008.

[Fionova 1993] L.K. Fionova, A.V. Artemyev, *Grain boundaries in metals and semiconductors*, Les editions de physique, 1993.

[Fthenakis 2007] V. Fthenakis, S. Gualtero, R. van der Meulen and H.C. Kim, Proc. of the Material Research Society, Symposium R, Boston, 2007.

[Fonash 1981] S.J. Fonash, *Solar cell device physics* (Academic Press, Inc.) ISBN 0-12-261980-3, 1981.

[Ginley 2000] D.S. Ginley et al., MRS bull. **25**, p. 15, 2000.

[Green 1982] M.A. Green, *Solar Cells : Operating principles, technology and system application*, Prentice Hall, 1982.

[Green 1987] M.A. Green, *High efficiency silicon solar cells*, Trans tech publications, 1987.

[Green 2002] M.A. Green, Physica E : Low-dimensional Systems and Nanostructures **14** p. 65, 2002.

[Green 2003] M.A. Green, *Third generation photovoltaics*, Springer, 2003.

[Green 2003b] M.A. Green, Proc. of the 3rd World conference on photovoltaic energy conversion, OPL-02, 2003.

[Grundmann 2005] M. Grundmann et al., Supperlattices microstruct. **38**, p.317, 2005.

[Goetzberger 2005]A. Goetzberger, V.U. Hoffmannn, *Photovoltaic solar energy generation*, Springer, 2005.

[Goetzberger 2005b] A. Goetzberger, J. Knobloch, B. Voss, *Silicon Solar Cells : Technology and Systems Applications*, Wiley, 1998.

[Gordon 1996] R.G. Gordon, Proceedings of the materials Research Society Symposium 426, 1996.

[Haase 2007] C. Haase, H. Stiebig, Applied physics letters **91**, p. 061116, 2007.

[Hagemann 2008] Hagemann et al., Proceedings of the EU PVSEC, Valencia, 2008.

[Hamberg 1986] I. Hamberg and C. G. Granqvist, J. Appl. Phys. **60**, R123 1986.

[Hartnagel 1995] H.L. Hartnagel, A.L. Dawar, A.K. Jain, C. Jagadish, *Semiconducting transparent thin films*, IOP publishing Ltd, 1995.

[Harvey 1989] J.E. Harvey, SPIE **1165**, Scatter from optical components, p. 87, 1989.

[Haug 2006] F.-J. Haug, V. Terrazzoni-Daudrix, T. Söderström, X. Niquille, J. Bailat, C. Ballif Proceedings of the 21st EU PVSEC, September 4-8 2006, Dresden, 2006.

[Hecht 1987] E. Hecht, *Optics*, 2nd ed. (Adelphi University) ISBN 0-201-11611-1, 1987.

[Herold 1962] R.J. Herold, S.L. Aggarwal, V. Neff, Canadian journal of chemistry **41**, p.1368, 1962.

[Hong 2002] R.J. Hong et al. J. Vac. Sci. Technol. **A20**, p.900, 20002.

[Hosono 2007] H. Hosono, Thin solid films **515**, p. 6000, 2007.

[Hüpkes 2006] J. Hüpkes et al. Thin solid films **502**, p.286, 2006.

[Ichikawa 1993] Y. Ichikawa, S. Fujikake, T. Takayama, S. Saito, H. Ota, T. Yoshida, T. Ihara, and H. Sakai, Proceedings of the 23rd IEEE Photovoltaic Specialists Conference, p. 27–33, 1993.

[IEA 2007] International Energy Agency, *Key World Energy Statistics*, 2007.

[IEA 2007b] International Energy Agency, *Renewables In Global Energy Supply*, 2007.

[IEA PVPS 2006] International Energy Agency-Photovoltaic Power Systems Programme, *Compared assessment of selected environmental indicators of photovoltaic electricity in OECD cities*, 2006.

[IEC 2005] International standard IEC 60904-3, *Measurement principles for terrestrial photovoltaic (PV) solar devices with reference spectral irradiance data*, 2005.

[Ip 2002] K. Ip, K.H. Baik, M.E. Overberg, E.S. Lambers, Y.W. Heo, D.P. Norton, S.J. Perton, F. Ren, J.M. Zavada, Applied Physics Letters, Vol. 81, p. 3546, 2002.

[IPCC 2007] Intergovernmental Panel on Climate Change (IPCC), *Climate Change 2007 : Synthesis Report, Fourth assessment report*, 2007.

[Jackson 1984] W.B. Jackson, N.M. Amer, Physical review B **25**, p.896, 1984.

[Jagadish 2006] C. Jagadish, S.J. Pearton, *Zinc oxide, bulk, thin films and nanostructures, Elsevier*, 2006.

[Jin 1988] Z. C. Jin, I. Hamberg, and C. G. Granqvist, J. Appl. Phys. **64**, p.5117 1988.

[Katsuma 2007] K. Katsuma, S. Hayakawa, A. Masuda, T. Matsui, and M. Kondo, Proceedings of the 22nd EU PVSEC, 2007.

[Kirchner 2003] C. Kirschner et al., J. Cryst. Growth **248**, p.20, 2003.

[Kluth 2001] O. Kluth, B. Rech, H. Wagner, Proc. of the 17th EUPVSEC, Germany, 2001.

[Kluth 2004] O. Kluth et al. Proc. of the 20th EUPVSEC, France, 2004.

[Krc 2003] J. Krc, F. Smole, M. Topic, Progress in Photovoltaics : Research and Applications **11**, p.429, 2003.

[Koida 2006] T. Koida, M. Kondo, Appl. Phys. Lett. **89**, p. 082104, 2006.

[Koida 2007] T.Koida, H. Fujiwara, M. Kondo, Jpn. J. Appl. Phys. **46** p L685-L687, 2007.

[Sinn 2006] M., Sinn, H.-W., Whalley, J. (eds.), *Privatization Experiences in the European Union,* MIT Press, Cambridge (MA), London, p. 199, 2006.

[Laherrere 2005] Laherrere, *Forecasting production from discovery*, ASPO May 19-20, 2005.

[Lechner 2004] P. Lechner et al., Proceedings of the EU PVSEC, Paris, 2004.

[Lechner 2008] P. Lechner, V.R. Gutlapalli, Proc. of the 23th EUPVSEC, Spain, 2008.

[Li 2001] X. Li et al., NREL/CP-520-31017, 2001.

[Limmer 1998] W. Limmer, W. Ritter, R. Sauer, B. Mensching, C. Liu, B. Rauschenbach, Appl. Phys. Lett. **72** p.2589 1998.

[Liu 2007] Y. Liu, J. K. Rath, and R. E. I. Schropp, Surf. Coat. Technol. 201, 9330, 2007.

[Löffler 2005] J. Löffler, *Transparent conductive oxides fort hin film silicon solar cells*, ISBN 90-393-06702, 2005.

[Logothetidis 2008] S. Logothetidis, A. Laskarakis, S. Kassavetis, S. Lousinian, C. Gravalidis, G. Kiriakidis, Thin solid films, **516**, p.1345, 2008.

[Losurdo 2002] M. Losurdo, M. Giangregorio, P. Capezzuo, G. Bruno, R. De Rosa, F. Roca, C. Summonte, J. Pla, R. Rizzoli, J. Vac, Sci. Technol. **20**(1), p. 37, 2002.

[Manjón 2005] F.J. Manj´on, B. Mari, J. Serrano, A.H. Romero, Appl. Phys. Lett. **97** P.53516, 2005.

[Martí 2004] A. Martí, A. Luque, *Next generation photovoltaics* (A. Martí, A. Luque, Institute of Physics, University of Madrid) ISBN 0-7503-0905-9, 2004.

[Masseti 1983] G. Masseti, M. Severi, S. Solmi, IEEE Trans. Electron Dev. ED**30**, p. 764, 1983.

[Matsubura 2002]K. Matsubura et al., Thin solid films **422**, p. 176, 2002.

[Matsui 2006] T. Matsui, A. Matsuda and M. Kondo, Solar Energy Materials and Solar Cells **90**, p. 3199, 2006.

[Meillaud 2006] F. Meillaud, A. Shah, C. Droz, E. Vallat-Sauvain, C. Miazza,Efficiency Solar Energy Materials and Solar Cells, Vol **90**, Issues 18-19, pp. 2952-2959, 2006.

[Meier 1994] J. Meier, R. Fluckiger, H. Keppner, A Shah, Applied Physics Letters, **65** p. 860, 1994.

[Meier 2003] J. Meier, J. Spitznagel, U. Kroll, C. Bucher, S. Faÿ, T. Moriarty1, A. Shah, Proceedings of the WCPEC-3, Osaka, 2003.

[Meier 2004] J. Meier, U. Kroll, E. Vallat-Sauvain, J. Spitznagel, U. Graf, and A. Shah, Sol. Energy **77**, p. 983, 2004.

[Meier 2008] J. Meier et al. Proc. of the 23th EUPVSEC, Spain, 2008.

[Messing 1993] G.L. Messing et al., J. Am. Ceram. Soc. **76**, p.2707, 1993.

[Metz 2004] A.W. metz et al., Chem. Vap. Depos. **10**, p.297, 2004.

[Minami 2000] T. Minami, MRS Bulletin, p.38-44, 2000.

[Minami 2005] T. Minami, Semicond. Sci. Technol. **20**, p. S35, 2005.

[Mott 1987] N. Mott, *Conduction in non-crystalline materials*, Oxford science publication, 1987.

[Mott 1990] N. Mott, *Metal-insulator transitions*, Taylor & Francis, 1990

[Myong 2007] S.Y. Myong, J. Steinhauser, R. Schlüchter, S.Faÿ, E, Vallat-Sauvain, A. Shah, C. Ballif, A. Rüfnacht, Solar energy materials and solar cells **91**, p.1269, 2007.

[Natsume 2000] Y. Natsume, H. Sakata, Thin solid films, **372**, p.30, 2000.

[Nickel 2004] N. Nickel, E. Terukov, *Zinc oxide – A material for micro and optoelectronic applications, Nato science series*, 2004.

[Niesen 2002] T.P. Niesen et al., Solid state ion. **151**, p.61, 2002.

[Noda 2003] M. Noda et al. Proc. of the 3rd World conference on photovoltaic energy conversion, Japan, 2003.

[Orton 1980] J.W. Orton, M.J. Powel, Rep. prog. phys. **43**, p.81, 1980.

[Orton 1981] J.W. Orton, Thin solid films 86, p.351, 1981.

[Özgür 2005] Ü. Özgür, Y. Alivov, C. Liu, A. Teke, M. A. Reshchikov, S. Dogan, V. Avrutin, S.-J. Cho, H. Morkoç, Journal of applied physics **98**, p. 41301, 2005.

[Pankove 1975] J.I. Pankove, Optical processes in semiconductors, 1975.

[Photon] http://www.photon-magazine.com/

[Pierson 1999] H.O. Pierson, *Handbook of chemical vapor deposition*, Norwich, NY Noyes publications, 1999.

[Poruba 2000] A. Poruba, A. Fejfar, Z. Remes, J. Springer, M. Vanecek, j. Kocka : Journal of Applied Physics **88** ,p.6436, 2000.

[Prince 2002] J.J. Prince et al., J. Cryst. Growth. **240**, p. 142, 2002.

[Python 2008] M. Python, E. Vallat-Sauvain, J. Bailat, D. Dominé, L. Fesquet, A. Shah, C. Ballif Journal of Non-Crystalline Solids, Proceedings of the 22nd ICANS Conference, Breckenridge, Colorado, **354**, p. 2258, 2008.

[Qiao 2006] Z. Qiao, C. Agashe, and D. Mergel, Thin Solid Films **496**, P.520 2006.

[Rath 2007] Rath, J.K., Y. Liu, R.E.I. Schropp, ICANS22, Colorado, U.S.A., 2007.

[Rech 2003] B. Rech, J. Müller, T. Repmann, O. Kluth, T. Roschek, J. Hüpkes, H. Stiebig, and W. Appenzeller, Proc. of the MRS conference, spring 2003.

[Rech 2005] B. Rech et al., Proceedings of the 20th EU PVSEC, Barcelona, pp. 1608-1611, 2005.

[Reeber 1970] R.R. Reeber Journal of applied physics **41**, p.5063, 1970.

[Repmann 2001] T. Repmann et al., Proc. of the 3rd World conference on photovoltaic energy conversion, Japan, 2003.

[Roth 1982] A.P. Roth, J.B. Webb, D.F. Williams, Phys. Rev. B **25**, p.7836, 1982

[Saito 1998] K. Saito, M. Sano, K. Matuda, T. Kondo, T. Nishimoto, K. Ogawa, and I. Kajita, Proceedings of the Second World Conference, p. 351, 1998.

[Schropp 1998] R.E.I. Schropp, M. Zeman, *Amorphous and Microcrystalline Silicon Solar Cells : Modeling, Materials and Device Technology (Electronic Materials: Science & Technology)*, Kluwer academic publisher, 1998.

[Schropp 2007] R.E.I. Schropp, R. Carius, G. Beaucarne, MRS Bulletin **32**, p. 219, 2007.

[Segawa 1997] Y. Segawa et al. Phys. Status solidi B **202**, p.669, 1997.

[Selvan 1998] A.J.A. Selvan, *ZnO for thin film solar cells*, thesis, Neuchâtel University, 1998.

[Sernelius 1988] B.E. Sernelius, K.F. Berggren, Z.C. Jin, I. Hamberg, C.G. Granqvist, Phys. Rev. B **37**, p.10244, 1988.

[Seto 1975] J.Y. Seto, Journal of Applied Physics **46**, p. 5247, 1975.

[Shah 1999] A. Shah, P. Torres, R. Tscharner, N. Wyrsch, H. Keppner, Science Vol **285**, p. 692, 1999.

[Shah 2004] A.V. Shah, H. Schade, M. Vanecek, J. Meier, E. Vallat-Sauvain, N. Wyrsch, U. Kroll, C. Droz, J. Bailat, Prog. Photovolt: Res. Appl., **12** p. 113-142, 2004.

[Shah 2006] A. Shah, J. Meier, A. Buechel, U. Kroll, J. Steinhauser, F. Meillaud, H. Schade and D. Dominé, Thin Solid Films, Volume **502**, Issues 1-2, p. 292-299, 2006.

[Simmons 1963] J.G. Simmons, Journal of applied physics **34**, p. 1793, 1963.

[Smith 1978] R.A. Smith, Semiconductors, 2nd ed. (Cambridge University Press) ISBN 0-521-21824-1, 1978.

[Smith 2003] S.M. Smith, H.B. Schlegel, Chem. Mater. **15**, p.162-166, 2003.

[Smits 1958] F.M. Smits, The Bell System Technical Journal **37**, p.711-718, 1958.

[Solarbuzz] http://www.solarbuzz.com/

[Springer 2002] J. Springer, A. Poruba, M. Vanecek, S. Fay, L. Feitknecht, N. Wyrsch, J. Meier, A. Shah, T. Repmann, O. Kluth, H. Stiebig, B. Rech: Proc. 17th European Photovoltaic Solar Energy Conf., Munich 2001, eds. B. McNelis, W. Palz, H.A. Ossenbrink, P. Helm, WIP, Munich, vol III, p. 2830-5, 2002.

[Springer 2004] J. Springer, B. Rech, W. Reetz, J. Müller and M. Vanecek, Solar Energy Materials and Solar Cells **85**,p.1 2005.

[Steinhauser 2005] J. Steinhauser, L. Feitknecht, S. Faÿ, R. Schlüchter, A. Shah, C. Ballif, J. Springer, L. Mullerova-Hodakova, A. Purkrt, A. Poruba, M. Vanecek, Proceedings of the 20th EU PVSEC, Barcelona, pp. 1608-1611, 2005.

[Steinhauser 2006] J. Steinhauser, S. Faÿ, R. Schlüchter, E. Vallat, S. Y. Myong, and C. Ballif, Mater. Res. Soc. Symp. Proc. p.928, 2006.

[Steinhauser 2007] J. Steinhauser, S. Faÿ, N. Oliveira, E. Vallat-Sauvain, and C. Ballif, Applied Physics Letters, **90**, p. 142107, 2007.

[Steinhauser 2007b] J. Steinhauser, S. Faÿ, N. Oliveira, E. Vallat-Sauvain, D. Zimin, U. Kroll, and C. Ballif, Physica status solidi a, Proc. of the E-MRS, 2007.

[Steinhauser 2008] J. Steinhauser, S. Faÿ, S. Meyer, M. Schwab, and C. Ballif, Proc. of 2nd International Symposium on Transparent Conductive Oxides, 2008.

[Sun 1994] C.J. Sun et al. J. Applied physics **76**, p.236, 1994.

[Sun 2005] S.S. Sun, N.S. Sacriciftci, *Organic photovoltaics* (CRC Press) ISBN 0-8247-5963-X, 2005.

[Sundaram 1997] K.B. Sundaram, J.vac. sci. technol. A **15**, p. 428, 1997.

[Sze 1981] S.M. Sze, *Physics of semiconductors*, 2nd ed. (John Wiley & Sons) ISBN 0-85226-846-7, 1981.

[Tao 1994] G. Tao, *Optical modeling and characterization of hydrogenated amorphous silicon solar cells*, Delft University Press, ISBN 90-407-1063-5.

[Tohsophon 2006] T. Tohsophon, J. Hüpkes, Proceedings of the E-MRS conference syposium F, 2006.

[UNDP 2000] United Nations Development Programme (UNDP), *World Energy Assessment, 2000.*

[Uni St Louis 2008] University of Saint Louis, Washington, *SIMS a brief introduction*, http://presolar.wustl.edu/work/what_is_sims.html, 2008.

[Urbach 1953] F. Urbach, Phys. Rev. **92**, p.1324, 1953.

[Van d Pauw 1958] L.J. Van der Pauw, Philips Research Reports **13**, 1958.

[Van de Walle 2000] C. Van de Walle, Physical review letters **85**, p.1012, 2000.

[Volintiru 2008] I. Volintiru, M. Creatore, M.C.M. Van de Sanden, Journal of applied physics **103**, p. 033704, 2008.

[Wenas 1991] W.Wenas, A. Yamada, K. Takahashi, M. Yoshino, and M. Konagai, Journal of applied physics **70**, p.7119-7123, 1991.

[Wenas 1994] W.Wenas, A. Yamada, M. Konagai, K. Takahashi, Proceedings of the 12th Photovoltiac solar energy conference, 1994.

[Wieser 1999] N. Wieser, O. Ambacher, H. Angerer, R. Dimitrov, M. Stutzmann, R. Stritzker, J.K.N. Lindner, Phys. Status Solidi B **216** p.806, 1999.

[Wild-Scholten 2005] M.J. de Wild-Scholten, E.A. Alsema, Proc. of the Materials Research Society Fall Meeting, Boston, USA, November 2005.

[Woodcock 1997] J.M. Woodcock, H. Schade, H. Maurus, B. Dimmler, J. Springer, A. Ricaud, Proceedings of 14th European Photovoltaic Solar Energy Conference, 857, 1997.

[Wu 2004] X. Wu, Solar Energy **77**, p. 803, 2004.

[Yamamoto 2002] K. Yamamoto et al. Solar energy materials and solar cells **74**, p. 449, 2002.

[Yan 2006] B. Yan, G. Yue, J. M. Owens, J. Yang, and S. Guha, Proceedings of the Fourth World Conference on Photovoltaic Energy Conversion, p. 4, 2006.

[Yim 2006] K. Yim et al., Cryst. Res. Technol. **41**, p. 1198, 2006.

[Zeman 2000] M. Zeman, R. A. C. M. M. van Swaaij, J. W. Metselaar, R. E. I. Schropp, Journal of applied physics **88**, p.6437, 2000.

[Zhou 2001] X.D. Zhou et al., J. Mater. Sci. **36**, p. 3759, 2001.

[Zweibel 2004] K. Zweibel, B. van Roedern, H. Ullal, Photon International October p.48, 2004.

University of Neuchâtel
Institute of Microtechnology

Low pressure chemical vapor deposited zinc oxide for thin film solar cells

Jérôme Steinhauser

Transparent conductive oxides, such as low pressure chemical vapor deposited zinc oxide doped with boron (LPCVD ZnO:B), play a major role as contacts in thin film silicon photovoltaic solar cells. This document study "LPCVD ZnO:B layers, from the deposition process to the final application" and focus especially on their electrical and optical properties.

This work intended on understanding the physics of the LPCVD ZnO:B film properties in order to efficiently optimize its characteristics to obtain transparent conductive oxide films well suited for thin film solar cell applications. In particular, theoretical models that describe the optical and electrical properties of LPCVD ZnO:B films are determined and verified experimentally.

ISBN 978-1-4092-8451-2
90000
9 781409 284512